PARTICLE TRANSPORT AND ION CURRENT RECTIFICATION IN CONICAL-SHAPED NANOPORES

by

Wenjie Lan

A dissertation submitted to the faculty of
The University of Utah
in partial fulfillment of the requirements for the degree of

Doctor of Philosophy

Department of Chemistry

The University of Utah

December 2011

The University of Utah Graduate School

STATEMENT OF DISSERTATION APPROVAL

The dissertation of **Wenjie Lan**

has been approved by the following supervisory committee members:

Henry S. White	, Chair	**9/15/2011** Date Approved
Joel M. Harris	, Member	**9/15/2011** Date Approved
Marc D. Porter	, Member	**9/15/2011** Date Approved
Ilya Zharov	, Member	**9/15/2011** Date Approved
Clayton C. Williams	, Member	**9/15/2011** Date Approved

and by **Henry S. White** , Chair of the Department of **Chemistry**

and by Charles A. Wight, Dean of The Graduate School.

ABSTRACT

This dissertation presents experimental and computational investigations of nanoparticle transport and ion current rectification in conical-shaped glass nanopore membranes (GNMs). Chapter 1 provides an overview of the Coulter counter or "resistive pulse" method, ion current rectification, and finite-element simulations used in solving mass transfer problems in conical-shaped nanopores.

Chapter 2 describes a fundamental study of the electrophoretic translocation of charged polystyrene nanoparticles in conical-shaped pores contained within glass membranes using the Coulter counter principle, in which the time-dependent current is recorded as the nanoparticle is driven across the membrane. Particle translocation through the conical-shaped nanopore results in a direction-dependent and asymmetric triangular-shaped resistive pulse. The simulation and experimental results indicate that nanoparticle size can be differentiated based on pulse height.

Chapter 3 presents experimental, theoretical, and finite-element simulation investigations of the pressure-driven translocation of nanoparticles across a conical-shaped GNM. Analytical theory and finite-element simulation for pressure-driven flow through a conical-shaped pore were developed to compute the volumetric flow rate, the position-dependent particle velocity, and the particle translocation frequency. The translocation frequencies computed from theory and simulation were found to be in agreement with experimental observations.

Chapter 4 reports the pressure-dependent ion current rectification that occurs in conical-shaped glass nanopores in low ionic strength solutions. Because the pressure-induced flow rate is proportional to the third power of the nanopore orifice radius, the pressure-driven flow can eliminate rectification in nanopores with radii of ~200 nm but has a negligible influence on rectification in a nanopore with a radius of ~30 nm. The dependence of the *i*-*V* response on pressure is due to the dependence of cation and anion distributions on convective flow within the nanopore.

Chapter 5 describes pressure-reversal methods to capture and release individual nanoparticles. One (or more) particle is driven through the orifice of a conical-shaped nanopore by pressure-induced flow. A reverse of flow, following the initial translocation, drives the particle back through the nanopore orifice in the opposite direction. The sequence of particle translocations in the capture step is preserved and can be read out in the release step. The observed instantaneous transfer rate and return probability are in good agreement with finite-element simulations of particle convection and diffusion in the confined geometry of the nanopore.

TABLE OF CONTENTS

LIST OF ABBREVIATIONS

1D – one-dimensional

2D – two-dimensional

3D – three-dimensional

Å– angstrom

-COOH – carboxylic acid

DLS – dynamic light scattering

ECR – electrophoretic capture and release

EOF – electroosmotic flow

Eq – equation

ESZ – electrical sensing zone

FEM – finite-element method

GNM – glass nanopore membrane

g – gram

ICR – ion current rectification

i – current

KCl – potassium chloride

mC – millicoulomb

mL – milliliter

mV – millivolt

n – normal

nA – nanoampere

nm – nanometer

pA – picoampere

PDEs – partial differential equations

PS – polystyrene

Pt – platinum

QNM – fused quartz nanopore membrane

SEM – scanning electron microscopy

TEM – transmission electron microscopy

V – volt

V – voltage

W rod – tungsten rod

μm – micrometer

LIST OF FIGURES

ACKNOWLEDGEMENTS

I would like to sincerely thank my PhD advisor, Professor Henry S. White. It's been a great honor and a real pleasure for me to work with him over the last four years. His integrity, enthusiasm in science, extensive knowledge, hard-working attitude, exceptional communication skills, and thoughtful guidance have been an inspiration to me. I attribute my success in future pursuits to the education I received from him.

I am grateful to my dissertation committee, Prof. Joel M. Harris, Prof. Marc D. Porter, Prof. Ilya Zharov, and Prof. Clayton C. Williams, for their insightful suggestions.

I also wish to thank all of the members of the White Group with whom I shared a laboratory, especially Prof. Jin Liu, Dr. Anna E. P. Schibel, Mr. Deric A. Holden, Ms. Qian Jin, Ms. Katrina Fairfax, Prof. Jiming Hu, Mr. Chris C. Cauley, Mr. Jiewen Xiong, Mr. Clemens Kubeil, Mr. Qianjin Chen, Ms. Jessica Bastian, Mr. Long Luo, and Prof. Gangli Wang. Thanks also to Prof. Ilya Zharov and Ms. Zhe Gao for their help in the DLS and zeta-potential measurements, to Prof. Bo Zhang for helpful discussions, and to Dr. Ming Wang and Dr. Yaorong Zheng in Prof. Peter Stang's group for our pleasant collaborations.

On a personal note, this dissertation is dedicated with affection to my parents, and all my family, for their continuing love, encouragement, and support.

Wenjie Lan

August 8, 2011

CHAPTER 1

INTRODUCTION

1.1 Coulter counter analysis

This dissertation describes the properties and applications of glass nanopore membranes (GNMs) as Coulter counters for the analysis of nanoparticles. The Coulter counter, invented by Dr. Wallace Coulter in 1953, is also called a resistive-pulse counter or electrical sensing zone (ESZ) counter.[1] It is an instrument used to detect and size objects, including particles, biological cells, abrasives, bacteria, clays, cosmetics, crystals, lubricants, microspheres, pharmaceuticals, vaccines, and water contaminants.[2]

Small apertures in the traditional Coulter counter (with diameters from ~20 μm to as large as 2 mm) are bounded by two electrolyte solutions, Figure 1.1. Particles in the solution are drawn through an aperture by a voltage bias or a pressure gradient applied across the channel. Two Ag/AgCl electrodes are placed on opposite sides of the aperture to generate an ionic current through the aperture. The current between the two electrodes is continuously monitored, enabling particle translocations through the pore that are sensed by a momentary change in electrical impedance.[3] The baseline current, determined by the electrolyte concentration, the applied potential, and the geometry of the pore,[4] is constant when particles are not present in the bulk solution. When a particle or a cell enters the pore, it displaces an amount of electrolyte solution that is equivalent to the particle volume. As a result, the pore resistance increases momentarily during the particle

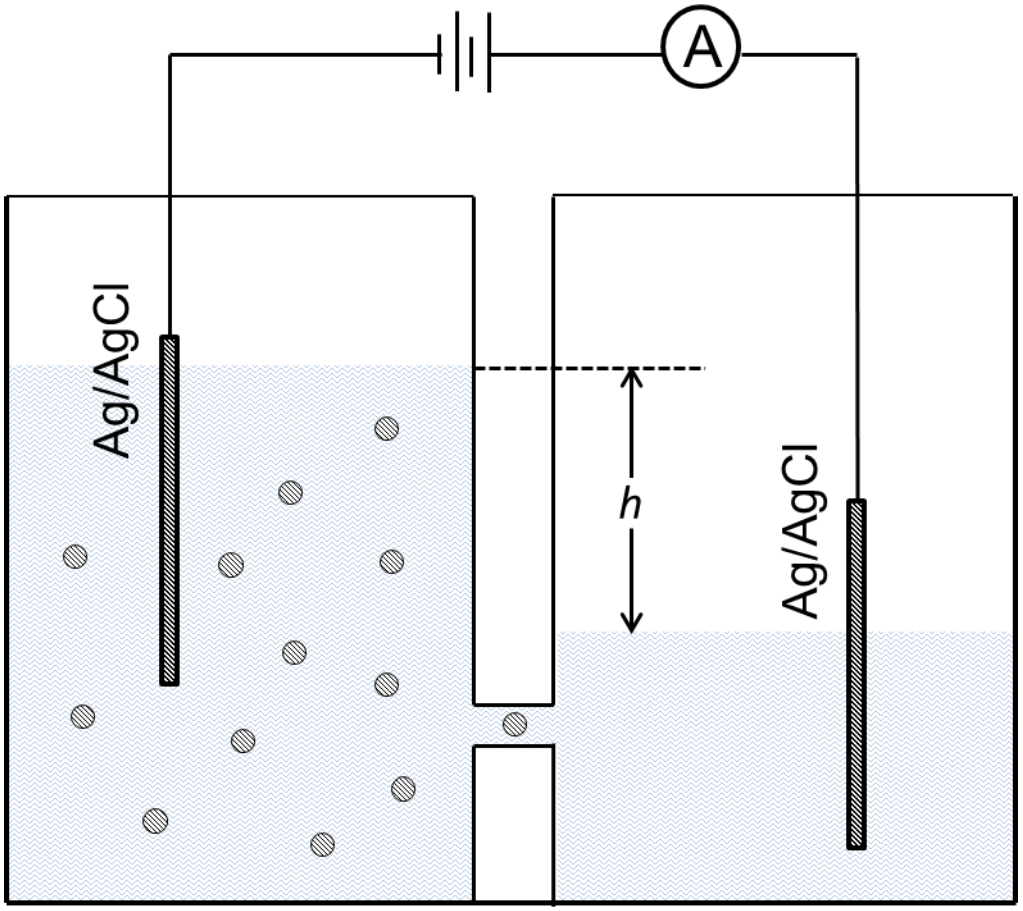

Figure 1.1. Schematic of a Coulter counter using hydrostatic pressure to drive particles through a membrane orifice. Adapted from the original Coulter counter patent (reference 1).

residence time. This transient attenuation generates a resistive pulse that can be measured in the current-time recordings. The resistive pulses generated by the particle translocations are recorded to determine the translocation frequency, pulse width, and peak height. The event frequency is generally proportional to the particle concentration in the sample. The amplitude of the pulse is directly proportional to the volume of the particle that produces it, thus providing the particle size. The peak width (or translocation time) offers insight into the effective charges carried by particles.[5] A membrane containing more than one pore can be utilized to size a mixture of particles in a short period of time.[6] In general, the pore can sense particles with radii that are between 20-80% of the pore radius. If the particle is too small, the change in resistance during particle translocation will be too small to be detected. On the other hand, if the particle is larger than the pore, it cannot translocate through the pore. These basic principles governing the Coulter counter strategy suggest that smaller nanopores may be able to detect smaller objects.

With the development of nanotechnology, scientists have pushed pore sizes to the nanometer scale, thus causing a resurgence of Coulter counting for the analysis of nanoscale objects. In the 1970s, DeBlois, Bean, and Wesley reported the extension of the Coulter technique to polystyrene particles (90 nm in diameter) and viruses (above 60 nm in diameter) through the use of submicron pores in a plastic sheet.[7,8] In the past 10 years, the development of synthetic[9] and biological nanopores[10] has attracted significant attention due to the application of nano-Coulter counters in the detection and analysis of nanoparticles and macromolecules.[11,12] Recently, the Crooks group reported applications of Si_3N_4 and PDMS membranes containing an individual multi-walled carbon nanotube

(~65 nm radius) as a nano-Coulter counter, as illustrated in Figure 1.2. Nanoparticles with different sizes and surface charges were simultaneously analyzed, and the results agreed with other techniques (transmission electron microscopy, TEM and dynamic light scattering, DLS).[13] Martin and coworkers used synthetic nanopore membranes as resistive-pulse sensors for molecular and macromolecule analytes.[14] The Zhang group reported the analytical application of cylindrical-shaped silica nanochannels for sensing single 40 nm radius polystyrene particles and molecular transport of double-stranded DNA.[15] Sohn and coworkers utilized micro-fabricated nanopores/channels in quartz substrate/PDMS membranes for counting particles as small as 43 nm in radius (~10^8 particles/mL) and for detecting the binding of unlabeled antibodies to the surface of a latex colloid by a resistive-pulse method.[16] In a previous report, our group introduced a technique of particle detection based on the "electrophoretic capture and release" (ECR), in which the nanopore was too small to allow translocation of nanoparticles.[17] Cylindrical solid-state nanopores (as small as 20 nm) fabricated by electron-beam lithography were able to detect polystyrene particles with the Coulter counting technique.[18] There are also commercial instruments based on the Coulter counting method. Multisizer 4 COULTER COUNTER (Beckman Coulter, Inc.),[19] for instance, is used to analyze particles from 0.4 to 1600 μm in diameter. Other techniques, such as TEM,[20 a,20b] scanning electron microscopy (SEM),[20c] and DLS[20d] are rountinely used to characterize nanoparticles.

In Coulter counters, the analyte is driven through the pore using a pressure gradient or an electric field.[21] Most recent publications have focused on the electric-field force to electrophoretically drive the particles or molecules through synthetic or biological pores. The references mentioned later in this paragraph represent pressure-

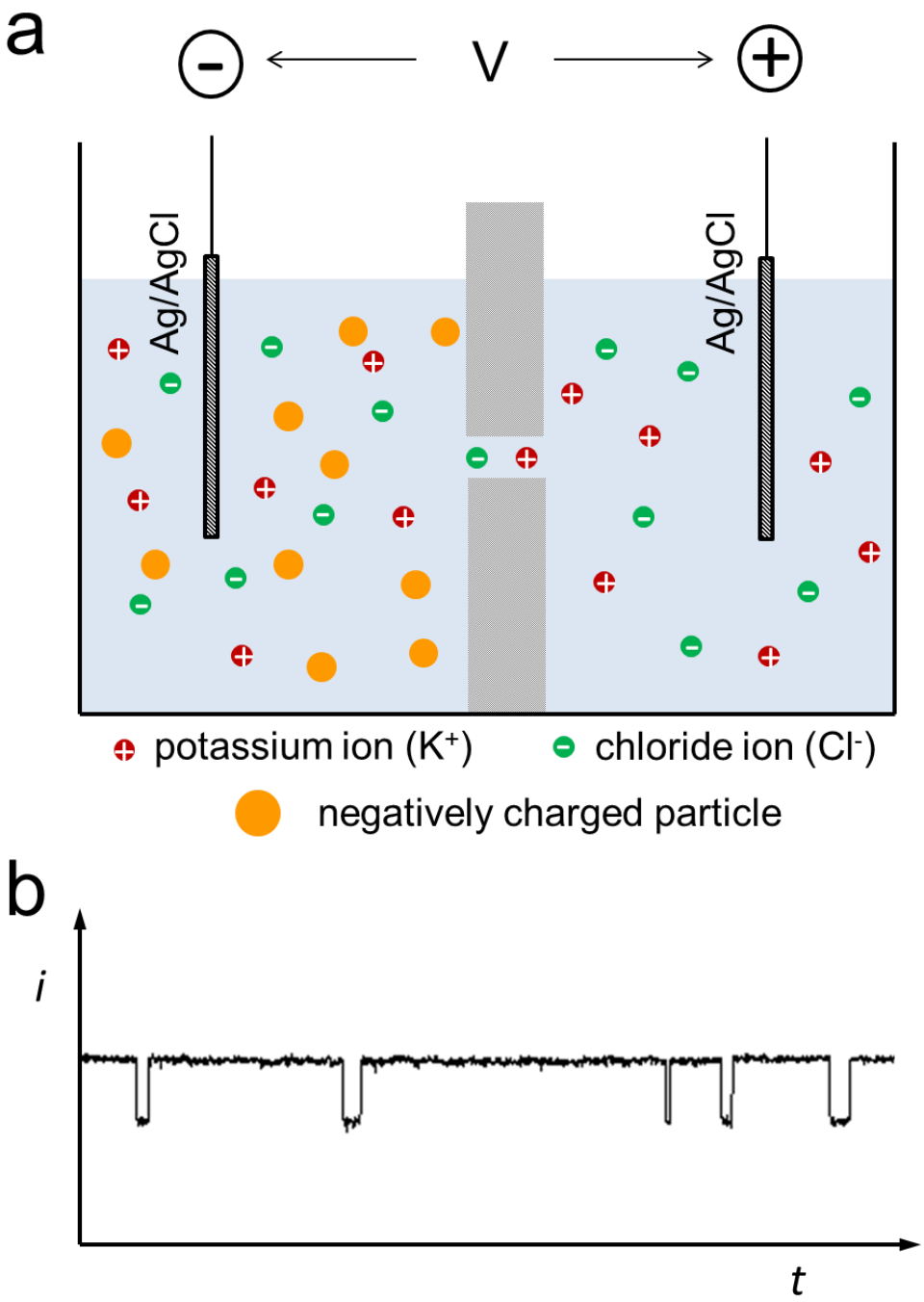

Figure 1.2. (a) Electric field-driven Coulter counting using a cylindrical pore, e.g., a carbon nanotube or a pore in Si_3N_4. (b) A typical current-time recording for particles translocating through a cylindrical pore.

driven analyte analyses using the Coulter counter. The original Coulter counter used hydrostatic pressure to drive particles through the small orifice.[1] Sun and Crooks also reported the hydrodynamic transport of polystyrene particles through single cylindrical carbon nanotubes and demonstrated that the experimental particle translocation rate constant was in approximate agreement with the calculated value.[13] Willmott, Roberts, Trau, Vogel, and coworkers reported the fabrication of tunable nanopores in elastomeric membranes and their applications in particle detection, discrimination, and sizing, using a pressure-driven flow or electrophoresis.[22] Keyser and coworkers demonstrated that a few tens of DNA strands bound to colloids can be detected by the pressure-driven translocation through a microcapillary-based Coulter counter.[23] Through simple comparison of current amplitudes for blank and DNA-coated colloids at low salt concentrations (2-40 mmol NaCl), the surface charges on colloids can be detected, and the results were in good agreement with a dynamical computer model. Zhe et al. described a micromachined Coulter counter with multiple sensing microchannels for quantitative measurement of particles and pollen. The particle solution was forced through the microchannels by creating a pressure difference with a syringe.[24,25] Harnett et al. presented a design for a micro-Coulter counter with a stepped outlet channel, and demonstrated a 2.5' fold increase in signal strength over a nonstepped device, which resulted from hydrodynamic focusing in both horizontal and vertical directions.[26] Daoudil and Brochard presented a theoretical study of the passage of flexible polymers in solution through pores driven by hydrodynamic flows, thus showing that a critical driving force is needed for translocation.[27] A molecular dynamics simulation has also been utilized to study the transport behavior of water molecules in a single-walled carbon nanotube.[28]

The dissertation herein is focused on electrophoresis[29] and pressure-driven[30] Coulter analyses, which can be applied to charged and neutral particles in aqueous or non-aqueous solutions. Quantitative analyses of pressure-dependent transfer rate, duration time, and resistive-pulse height have been conducted. Analytical theories, as well as the finite-element simulations, were also developed to better understand the mechanism of particle translocation.

In the Coulter analysis, if the same analyte (particles or molecules) can be driven repetitively back and forth through the pore, the analysis accuracy may be enhanced by multiple measurements. This method potentially provides a way to detect in-situ size and conformational structure changes of the analyte during the translocation process since the Coulter technique is very sensitive to variance of the analyte volume.[31] Gershow and Golovchenko have investigated multiple translocations of a single DNA molecule through a nanopore by reversing the transmembrane potential direction after molecule translocation. These researchers studied the mechanism and dynamics of trapping and recapturing single DNA molecules experimentally in a solid-state silicon nitride nanopore, and by numerical solution of a physical drift-diffusion model.[32] Repeated translocation of the same molecules demonstrates the ability to capture and manipulate single macromolecules in a solution. The similar fast voltage switching method has also been applied by Meller to probe the escape of single-stranded DNA from a protein pore.[33] Our group has used alternating current to measure the diffusion coefficient of DNA oligomers in the protein ion channel, using a d.c. voltage to capture and release the molecules within the protein lumen.[34]

The pressure-reversal technique in the cylindrical-micropores-based Coulter counter was first reported by Berge and Jossang in 1990 to broaden the application of the resistive pulse technique.[35] A trigger signal from the particle translocation was used to activate two miniature solenoid valves (pressure switches). The capture and release translocation shapes have been shown for particles, bacteria, and air bubbles. The same group also probed the phenomenon of particle radial migration in Poiseuille flow using the pressure-reversal method. The authors indicated that this technique potentially enables the study of single-particle flow dynamics.[35]

In this dissertation, a pressure-reversal method in the GNM-based Coulter conter was developed to capture and release between one and several hundred nanoparticles in conical-shaped GNMs.[36] A convection-diffusion model was developed and solved by finite-element simulations to quantitatively predict the experimental results.

The Coulter counters used in our investigations are based on the bench-top made GNMs. The GNM comprises a glass capillary containing an individual conical-shaped nanopore in a membrane with 20-75 μm thickness. A sharpened Pt tip is used as a template in the construction of the conical-shaped pore.[37-40] The orifice radii of the GNMs can be varied from tens of nanometers to several micrometers. GNMs are excellent platforms for a nano-Coulter counter. Recently, GNMs have been designed as support structures for planar bilayers for ion-channel recordings, which are essentially molecular Coulter counters.[41] Compared to traditional Coulter counters with cylindrical openings, the conical-shaped GNM has potential advantages in sensing analytes.[42] The mass transfer resistance of the GNM and the potential drop across the membrane are highly localized at the small opening of the pore, as shown in Figure 1.3. A consequence of this

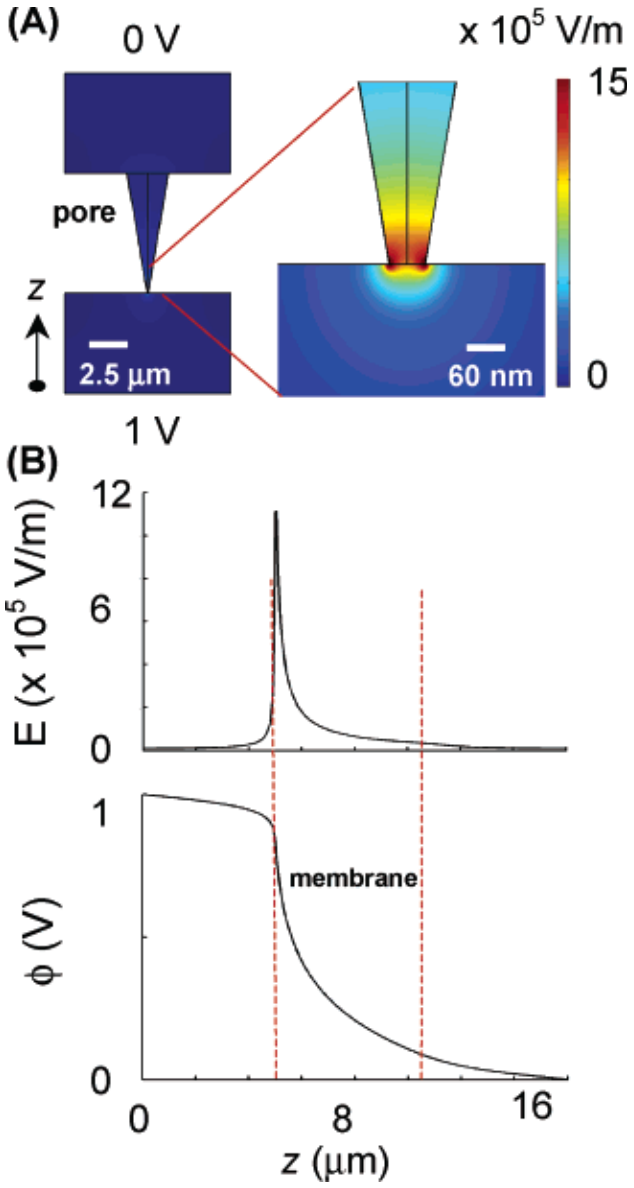

Figure 1.3. (a) Distribution of the electric field across a conical-shaped pore with a large-opening diameter of 2.5 μm, small-opening diameter of 60 nm, and thickness of 6 μm. (b) Line profiles of the electric field and potential across the membrane corresponding to the centerline axis of the pore (from reference 42).

localization and decreased volume of the sensing zone is potentially higher sensitivity to the particle's geometrical and chemical properties than is possible using a cylindrical pore. Additional advantages of glass nanopores include their excellent chemical stability in electrolyte solutions, mechanical robustness in pressure-driven particle transport, favorable electrical properties for high-bandwidth measurements, and a continuous range of orifice sizes (between several nanometers to tens of micrometers).

1.2 Ion current rectification in nanopores

An interesting mass transfer characteristic in conical-shaped nanopores is ion current rectification (ICR).[43] ICR is defined as the experimental departure of current-voltage responses of nanopores or nanotubes from the linear ohmic behavior,[44] i.e., the magnitude of the current flowing through the nanopore between two Ag/AgCl electrodes at negative potentials is larger or smaller than the current at the same positive potentials, as shown in Figure 1.4 (right part). Wei, Bard, and Feldberg first reported ICR in 1997 based on experiments using quartz nanopipets.[45] They noted that the ICR behavior in the conical-shaped nanopipets is strongly dependent on the ionic strength and nanopipet orifice size. Since then, numerous reports have been published concerning the manipulation of ICR phenomena and the sensing applications of ICR in pores with various materials, surface modifications, radii, and electrolyte concentrations. [46] Generally, ICR can occur in conical-shaped nanopores[47] or cylindrical nanopores with asymmetric surface charge distribution.[48,49]

Recently, Wang and Jiang have successfully attached a pH-sensitive DNA molecular motor to the synthetic poly (ethylene terephthalate) (PET) nanopore, giving different conductive states at various pHs.[50] Jiang and Zhu demonstrated a biomimetic

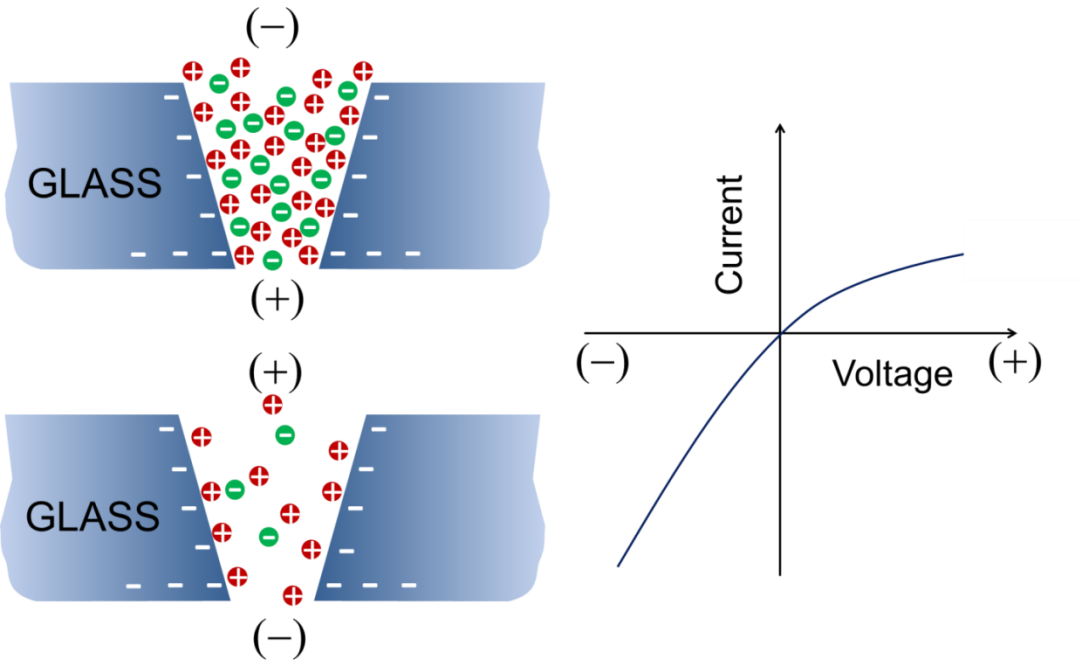

Figure 1.4. Schematic representation of ion current rectification in conical-shaped glass nanopores.

asymmetric responsive single nanochannel system, which is pH and temperature tunable.[51] Siwy et al. described a new method of biosensing with nanofluidic diodes, using the rectification factor as the detection signal for presence of an analyte.[52] They also showed the manipulation of transport properties of nanofluidic devices by changing the ionic species and the concentrations on each side of the nanopore membrane.[53] Azzaroni reported the integration of polymer brushes into single conical nanochannels to effectively control the ICR by pH value.[54] The same group also used a layer-by-layer assembly technique to construct multilayered films of poly (allylamine hydrochloride) (PAH) and poly (styrenesulfonate) (PSS) on the pore surface, in order to change the mass transport.[55] Zhang and coworkers have shown that current rectification of a cone-shaped silica nanopore strongly depends on the rate of the voltage scan.[56]

The asymmetric distribution of surface charges on the pore walls gives rise to ICR,[57] as illustrated in Figure 1.4. For glass nanopores, the surface is negatively charged at neutral pH due to the dissociation of the surface silanol groups. The number of surface charges depends on the number of active surface sites and the pK_a of the dissociation reaction. The electrical double layer associated with charged surface has a thickness of $\sim 5\kappa^{-1}$,

$$\kappa^{-1} = \sqrt{\frac{\varepsilon_r \varepsilon_0 RT}{2z^2 F^2 c}} \tag{1.1}$$

where κ^{-1} is the Debye screening length, ε_r is the relative permittivity, ε_0 is the permittivity in a vacuum, R is the gas constant, T is the absolute temperature, z is the electrolyte valence, F is Faraday's constant, and c is the electrolyte concentration. The

Debye length is ~3 nm for a 0.01 M KCl solution and ~0.3 nm for a 1 M KCl solution. These were the most commonly used solutions in the experiments described in the following chapters.

When the conical-shaped pore orifice size (a) approaches the nanoscale and is of the order of magnitude of $5\kappa^{-1}$, the volume of solution in the pore orifice becomes cation selective because of the negative charges on the surface. Later, when a negative potential (pore interior vs. external solution) is applied across the membrane, the potassium ion (K^+) flux is directed from external solution to the pore interior, while the chloride ions (Cl^-) move in the opposite direction. As the pore is small and negatively charged, Cl^- ions are rejected by the glass surface due to the electric field resulting from this surface charge. Thus, there is an increase in Cl^- concentration within the pore interior, resulting in a greater conductivity inside the pore than that of the bulk KCl solution. Conversely, when a positive potential is applied inside the pore relative to the external solution, the transport of Cl^- from external solution to pore interior is rejected by the surface charges and Cl^- is depleted within the pore. This decreases the nanopore conductivity and the experimentally measured ion current.[58]

It is imperative to note that the small pore size and conical pore shape are prerequisites of this explanation. Under this circumstance, the electric field is confined in the small area of the pore orifice and most of the mass transfer resistance is also located in that area. Even a small change of the electrolyte concentration or electric conductivity in this area causes a significant change in the ionic current flowing through the nanopore. At positive or negative potentials, the electrolyte concentration outside the pore orifice is slightly greater or smaller than that in the bulk KCl solution based on the above

explanation. However, the conductivity change is insignificant compared to the change inside the pore, and the ion current is more dependent on the conductivity just inside the pore orifice. Thus, the variation of the conductivity profile inside the pore determines the ionic current at positive or negative potentials. A larger conical-shaped nanopore displays a weaker rectification than a smaller pore due to a smaller extension of the ion electrical double layer into the pore. The above qualitative explanation is quantitatively supported by previously published finite-element simulations.[59-61] It has been generally assumed that the rectification behaviors are strongly dependent on the pore size, surface charges, and the ionic strength. In Chapter 4, a fundamental but previously unobserved pressure-dependent ion current rectification is reported in conical-shaped glass nanopores.[62] Also, the nanoparticle translocations through ion current rectifying nanopores were found to generate double-peak current pulses in the corresponding *i-t* recordings.[63]

There are three basic partial differential equations (PDEs) governing ion transport phenomena in nanopores, which describe the ion fluxes within the nanopore. The first of three is the Nernst-Planck equation:

$$\mathbf{J}_i = -D_i \nabla c_i - \frac{z_i F}{RT} D_i c_i \nabla \Phi + c_i \mathbf{u} . \qquad (1.2)$$

In eq 1.2, $\mathbf{J}_i$, D_i, c_i, and z_i are, respectively, the ion flux vector, diffusion coefficient, concentration, and charge of species i in solution. Φ and $\mathbf{u}$ are the local electric potential and fluid velocity, while F, R, and T are Faraday's constant, the gas constant, and the absolute temperature, respectively. The three terms in the right-hand side represent the contributions of ion transport from diffusion, migration, and convection, respectively.

The fluid velocity is induced by the applied pressure across the GNM or electroosmotic flow due to the negatively charged pore surface.

Another PDE describes the relationship between the electric charge and the electric potential in the nanopore. The relationship between local electric potential Φ and ion concentrations c_i is given by the Poisson equation, eq 1.3,

$$\nabla^2\Phi = -\frac{F}{\varepsilon}\sum_i z_i c_i \tag{1.3}$$

where ε is the dielectric constant of the solution.

Finally, the pressure-driven or electroosmosis-driven flow through the nanopore is described by the Navier-Stokes equation, eq 1.4, and it relates pressure and local charge density to fluid velocity.

$$\mathbf{u}\nabla\mathbf{u} = \frac{1}{\rho}(-\nabla P + \eta\nabla^2\mathbf{u} - F\left(\sum_i z_i c_i\right)\nabla\Phi) \tag{1.4}$$

In eq 1.4, ρ and η are the density and viscosity of the fluid, while P is the pressure. A description of mass transfer in the nanopore involves the simultaneous solution of the above system of PDEs. However, the simultaneous solution of coupled PDEs is not simple, especially in complicated or irregular geometries, such as those of conical-shaped nanopores. Due to the truncated conical geometry of the GNM, analytical solutions to the three equations mentioned above are not easy to prove. Numerical methods have to be used to solve these equations.

1.3 Finite-element simulations of mass transfer in nanopores

Numerical methods have been widely utilized to simulate various scientific phenomena. As a method of solving partial differential equations (PDEs), the finite-element method (FEM) has advantages in handling complicated or irregular geometries. The FEM is based on the idea of constructing a complicated irregular object from small and simple pieces, or more technically, it is mesh discretization of a continuous domain into a set of discrete sub-domains. The continuum PDEs are thus discretized in a large quantity of small pieces or meshes by using Δx instead of ∂x. This is a proven numerical technique to approximate the solutions of PDEs. The approach eliminates the differential equation (linear), or converts the PDEs into a set of ordinary differential equations.

FEM uses a complex system of points (nodes) and a grid (mesh). For a two dimensional geometry, the domains are generally divided into triangular or quadrilateral mesh elements, while in 3D, FEM partitions the domains into tetrahedral, hexahedral, or prism mesh elements. The mesh size can be adjusted in different areas of the geometry in order to more accurately solve the PDEs in the areas of interest. The discrete elements are then connected and integrated to approximate the solutions for PDEs.

Richard L. Courant developed FEM in 1942, expanding the variational methods described by Rayleigh, Ritz, and Galerkin to solve several two dimensional examples of equilibrium and vibration.[64] The original paper published by Courant used piecewise-linear approximants on a set of triangular subdomains, which are also called "elements". The method of solving plane problems using FEM was then broadened between the 1950s and 1970s. With the declining cost and increasing efficiency of personal computers, FEM was no longer limited to mainframe computers. Because an average

desktop computer can now perform such finite-element analyses with high precision on complex geometries, FEM is widely used in areas of science and engineering.

Numerical methods have been extensively applied to nanopore transport. Cervera et al. solved the Nernst-Planck and Poisson equations, while neglecting the convection term in a conical-shaped nanopore.[65] The surface charge on the pore walls was used as the only adjustable parameter to simulate the mass transport properties of the conical pores in PET, and the simulation results are in qualitative agreement with the experimental data. Daiguji and coworkers numerically modeled the ionic transport in nanofluidic channels based on the same equations.[66] Our group also solved the Nernst-Planck equation in the simulation to model the voltammetric behavior of a truncated cone-shaped nanopore electrode.[39]

White and Bund have used the FEM to solve Nernst-Planck, Poisson, and Navier-Stokes equations to simulate the ion transport phenomena in conical-shaped nanopores.[59] They also solved several simple electrochemistry problems with finite-element analysis involving the electrical double layer and electroosmosis, where known analytical solutions exist. The accuracy of FEM for simulating electrochemical double layer problems was verified in their paper by comparison to known analytical solutions. They simulated the current rectification behavior of a conical-shaped GNM and demonstrated that the rectification is mainly due to a change in the ionic conductivity in the vicinity of the pore orifice at varying bias voltages, as shown in Figure 1.5.[59] This change in the ionic conductivity results from redistribution of the ionic species under the influences of the external electric field and pore surface charge.

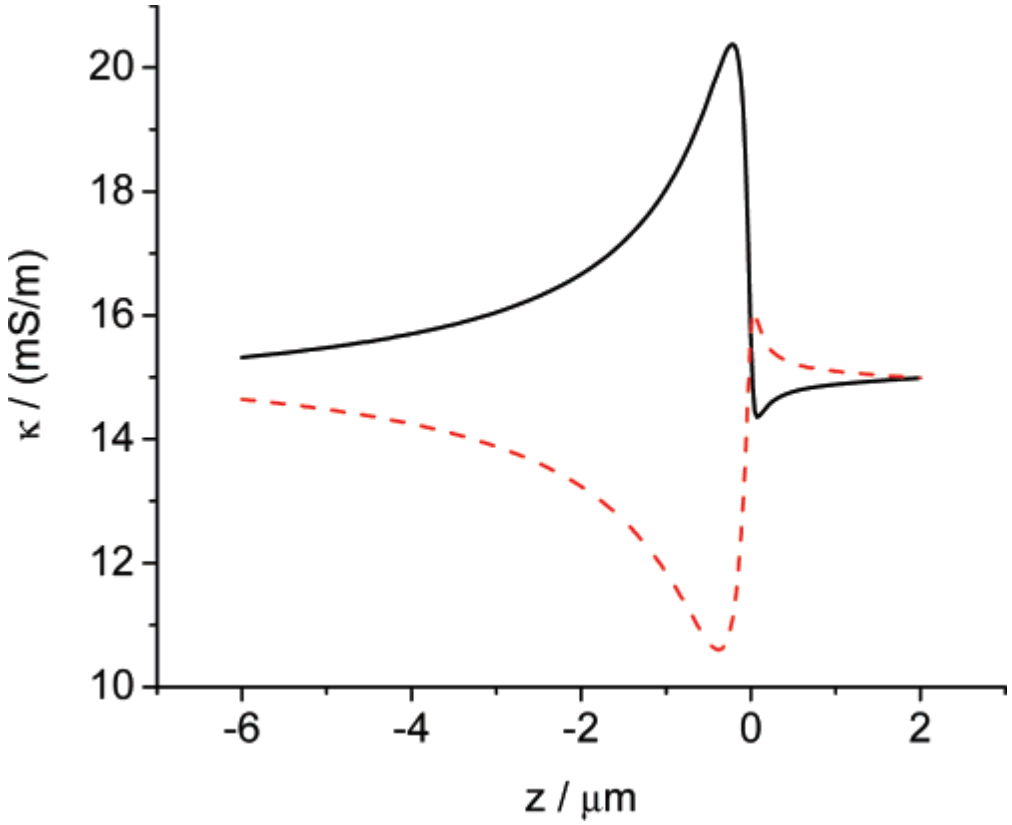

Figure 1.5. Electric conductivity along the center-line *z* axis (*r* = 0) of a 50 nm orifice radius nanopore (base radius 2.2 μm, length 10 μm, half cone angle 12 °, surface charge -1 mC/m^2) in 1 mM KCl as a function of applied bias (*E*) across the nanopore: (-) -0.5 V and (--) +0.5 V. The bulk value of the conductivity is 15 mS/m, corresponding to a 1 mM KCl solution. The orifice of the pore is located at *z* = 0 (from reference 59).

In the following chapters, finite-element simulations were performed to solve the Nernst-Planck, Poisson, or Navier-Stokes equations in order to qualitatively or quantitatively predict the particle transport frequency, translocation shape, current pulses height and duration time, and ionic current in conical-shaped nanopores. COMSOL Multiphysics commercial finite-element software was used throughout this dissertation. The simulations were performed by building physical models, constructing model geometries, choosing suitable subdomain and boundary settings, creating a mesh for the finite elements, compiling the PDEs in the given geometry with computational mesh, and postprocessing the solution. The modules were established by defining the relevant physical quantities, such as material properties, voltages, electrolyte concentrations, and pressures through a graphical user interface.

We report the numerical solution of the Nernst-Planck equation for particle transport behavior of a conical-shaped GNM (Chapter 2). Also, the Navier-Stokes equation was solved numerically to simulate the behavior of pressure-driven flow through a GNM (Chapter 3). The coupled Nernst-Planck, Poisson, and Navier-Stokes equations were solved simultaneously to predict the pressure-dependent ion current rectification (Chapter 4). Additionally, a coupled model of time-dependent Nernst-Planck and Navier-Stokes equations was established to allow the simulation of particle capture and release within a GNM (Chapter 5). The solutions of the Poisson and Nernst-Planck equations were also combined with a dynamic particle trajectory to predict the double-peak resistive pulse for particle translocation through ion current rectifying nanopores.

1.4 References

(1) Coulter, W. H. Means for Counting Particles Suspended in a Fluid. U.S. Patent 2,656,508, 1953.

(2) Williams, W. J.; Beutler, E.; Erslev, A. J.; Lichtman, M. A. *Hematology*, 3rd ed.; McGraw-Hill Book Company: New York, 1983.

(3) Bayley, H.; Martin, C. R. *Chem. Rev.* **2000**, *100*, 2575-2594.

(4) (a) Ho, C.; Qiao, R.; Heng, J. B.; Chatterjee, A.; Timp, R. J.; Aluru, N. R.; Timp, G. *Proc. Natl. Acad. Sci. U.S.A.* **2005**, *105*, 10445. (b) Li, N.; Yu, S.; Harrell, C.; Martin, C. R. *Anal. Chem.* **2004**, *76*, 2025.

(5) Murray, R. W. *Chem. Rev.* **2008**, *108*, 2688-2720.

(6) (a) Kobayashi, Y.; Martin, C. R. *Anal. Chem.* **1999**, *71*, 3665. (b) Yu, S.; Lee, S. B.; Martin, C. R. *Anal. Chem.* **2003**, *75*, 1239. (c) Martin, C. R. *Science* **1994**, *266*, 1961.

(7) DeBlois, R. W.; Bean, C. P. *Rev. Sci. Instrum.* **1970**, *41*, 909-916.

(8) DeBlois, R. W.; Wesley, R. K. A. *J. Virol.* **1977**, *23*, 227-233.

(9) (a) Li, J.; Stein, D.; McMullan, C.; Branton, D.; Aziz, M. J.; Golovchenko, J. A. *Nature* **2001**, *412*, 166-169. (b) Storm, A. J.; Chen, J. H.; Ling, X. S.; Zandbergen, H. W.; Dekker, C. *J. Appl. Phys.* **2005**, *98*, 014307. (c) Wu, M. Y.; Krapf, D.; Zandbergen, M.; Zandbergen, H.; Batson, P. E. *Appl. Phys. Lett.* **2005**, *87*, 113106. (d) Chen, P.; Mitsui, T.; Farmer, D. B.; Golovchenko, J.; Gordon, R. G.; Branton, D. *Nano Lett.* **2004**, *4*, 1333-1337. (e) Lo, C. J.; Aref, T.; Bezryadin, A. *Nanotechnology* **2006**, *17*, 3264-3267. (f) Dekker, C. *Nature Nanotech.* **2007**, *2*, 209-215. (g) Martin, C. R.; Siwy, Z. S. *Science* **2007**, *317*, 331-332.

(10) (a) Bezrukov, S. M.; Vodyanoy, I.; Parsegian, V. A. *Nature* **1994**, *370*, 279-281. (b) Kasianowicz, J. J.; Brandin, E.; Branton, D.; Deamer, D. W. *Proc. Natl. Acad. Sci. U.S.A.* **1996**, *93*, 13770-13773. (c) Bayley, H.; Cremer, P. S. *Nature* **2001**, *413*, 226-230. (d) Meller, A.; Nivon, L.; Branton, D. *Phys. Rev. Lett.* **2001**, *86*, 3435-3438. (e) Ambjornsson, T.; Apell, S. P.; Konkoli, Z.; Di Marzio, E. A.; Kasianowicz, J. J. *J. Chem. Phys.* **2002**, *117*, 4063-4073. (f) Henrickson, S. E.; Misakian, M.; Robertson, B.; Kasianowicz, J. J. *Phys. Rev. Lett.* **2000**, *85*, 3057-3060.

(11) (a) Li, J. L.; Gershow, M.; Stein, D.; Brandin, E.; Golovchenko, J. A. *Nature Mater.* **2003**, *2*, 611-615. (b) Han, A.; Schürmann, G.; Mondin, G.; Bitterli, R. A.; Hegelbach, N. G.; De Rooij, N. F.; Staufer, U. *Appl. Phys. Lett.* **2006**, *88*, 093901. (c) Fologea, D.; Ledden, B.; McNabb, D. S.; Li, J. *Appl. Phys. Lett.* **2007**, *91*, 053901. (d) Fologea, D.; Gershow, M.; Ledden, B.; McNabb, D. S.;

Golovchenko, J. A.; Li, J. *Nano Lett.* **2005**, *5*, 1905-1909. (e) Fologea, D.; Uplinger, J.; Thomas, B.; McNabb, D. S.; Li, J. L. *Nano Lett.* **2005**, *5*, 1734-1737. (f) Storm, A. J.; Storm, C.; Chen, J.; Zandbergen, H.; Joanny, J.-F.; Dekker, C. *Nano Lett.* **2005**, *5*, 1193-1197.

(12) (a) Kasianowicz, J. J.; Brandin, E.; Branton, D.; Deamer, D. W. *Proc. Natl. Acad. Sci. U.S.A.* **1996**, *93*, 13770-13773. (b) Gu, L. Q.; Braha, O.; Conlan, S.; Cheley, S.; Bayley, H. *Nature* **1999**, *398*, 686-690.

(13) (a) Sun, L.; Crooks, R. M. *J. Am. Chem. Soc.* **2000**, *122*, 12340-12345. (b) Ito, T.; Sun, L.; Crooks, R. M. *Anal. Chem.* **2003**, *75*, 2399-2406. (c) Ito, T.; Sun, L.; Bevan, M. A.; Crooks, R. M. *Langmuir* **2004**, *20*, 6940-6945. (d) Ito, T.; Sun, L.; Crooks, R. M. *Chem. Comm.* **2003**, 1482-1483. (e) Henriquez, R. R.; Ito, T.; Sun, L.; Crooks, R. M. *Analyst* **2004**, *129*, 478-482. (f) Ito, T.; Sun, L.; Henriquez, R. R.; Crooks, R. M. *Acc. Chem. Res.* **2004**, 937-945.

(14) (a) Choi, Y.; Baker, L. A.; Hillebrenner, H.; Martin, C. R. *Phys. Chem. Chem. Phys.* **2006**, *8*, 4976-4988. (b) Siwy, Z. S.; Trofin, L.; Kohli, P.; Baker, L. A.; Trautmann, C.; Martin, C. R. *J. Am. Chem. Soc.* **2005**, *127*, 5000-5001. (c) Park, S. R.; Peng, H.; Ling, X. S. *Small* **2007**, *3*, 116-119. (d) Harrell, C. C.; Choi, Y.; Horne, L. P.; Baker, L. A.; Siwy, Z. S.; Martin, C. R. *Langmuir* **2006**, *22*, 10837-10843. (e) Heins, E. A.; Siwy, Z. S.; Baker, L. A.; Martin, C. R. *Nano Lett.* **2005**, *5*, 1824-1829. (f) Sexton, L. T.; Horne, L. P.; Sherrill, S. A.; Bishop, G. W.; Baker, L. A.; Martin, C. R. *J. Am. Chem. Soc.* **2007**, *129*, 13144-13152.

(15) Zhang, B.; Wood, M.; Lee, H. *Anal. Chem.* **2009**, *81*, 5541-5548.

(16) (a) Saleh, O. A.; Sohn, L. L. *Rev. Sci. Instrum.* **2001**, *72*, 4449-4451. (b)Saleh, O. A.; Sohn, L. L. *Proc. Natl. Acad. Sci. U.S.A.* **2003**, *100*, 820-824.

(17) White, R. J.; White, H. S. *Anal. Chem.* **2007**, *79*, 6334-6340.

(18) Petrossian, L; Wilk, S. J.; Joshi, P.; Goodnick, S. M.; Thornton, T. J. *J. Phys.: Conf. Ser.* **2008**, *109*, 012028.

(19) http://www.beckman.com/coultercounter/product_multisizer4.jsp

(20) (a) Wang, X.; Zhuang, J.; Peng Q.; Li, Y. *Nature* **2005**, *437*, 121-124. (b) Lan, W. J.; Yu, S. H.; Qian, H. S.; Wan, Y. *Langmuir* **2007**, *23*, 3409-3417. (c) Wan, Y.; Wu, C.; Min, Y.; Yu, S. H. *Langmuir* **2007**, *23*, 8526-8530. (d) Colver, P. J.; Colard, C. A. L.; Bon, S. A. F. *J. Am. Chem. Soc.* **2008**, *130*, 16850-16851.

(21) *International Standard*, ISO 13319:2007(E), ISO, Geneva, 2007.

(22) (a) Willmott, G. R.; Vogel, R.; Yu, S. S. C.; Groenewegen, L. G.; Roberts, G. S.; Kozak, D.; Anderson, W.; Trau, M. *J. Phys.: Condens. Matter* **2010**, *22*, 454116.

(b) Roberts, G. S.; Kozak, D.; Anderson, W.; Broom, M. F.; Vogel, R.; Trau, M. *Small* **2010**, *6*, 2653-2658. (c) Vogel, R.; Willmott, G.; Kozak, D.; Roberts, G. S.; Anderson, W.; Groenewegen, L.; Glossop, B.; Barnett, A.; Turner, A.; Trau, M. *Anal. Chem.* **2011**, *83*, 3499-3506. (d) Willmott, G. R.; Parry, B. E. T. *J. Appl. Phys.* **2011**, *109*, 094307.

(23) Steinbock, L. J.; Stober, G.; Keyser, U. F. *Biosens. Bioelectron.* **2009**, *24*, 2423-2427.

(24) Zhe, J.; Jagtiani, A.; Dutta, P.; Hu, J.; Carletta, J. *J. Micromech. Microeng.* **2007**, *17*, 304-313.

(25) Jagtiani, A. V.; Zhe, J.; Hu, J.; Carletta, J. *Meas. Sci. Technol.* **2006**, *17*, 1706-1714.

(26) Scott, R.; Sethu, P.; Harnett, C. K. *Rev. Sci. Instrum.* **2008**, *79*, 046104.

(27) Daoudil, S.; Brochard, F. *Macromolecules* **1978**, *11*, 751-758.

(28) Yu, H. Q.; Li, H.; Zhang, J. X.; Liu, X. F.; Liew, K. M. *Carbon* **2010**, *48*, 417-423.

(29) Lan, W. J.; Holden, D. A.; Zhang, B.; White, H. S. *Anal. Chem.* **2011**, *83*, 3840-3847.

(30) Lan, W. J.; Holden, D. A.; Liu, J.; White, H. S. *J. Phys. Chem. C* **2011**, *115*, 18445-18452.

(31) Smeets, R. M. M.; Kowalczyk, S. W.; Hall, A. R.; Dekker, N. H.; Dekker, C. *Nano Lett.* **2009**, *9*, 3089-3095.

(32) Gershow, M.; Golovchenko, J. A. *Nature Nanotech.* **2007**, *2*, 775-779.

(33) Bates, M.; Burns, M.; Meller, A. *Biophys. J.* **2003**, *84*, 2366-2372.

(34) (a) Lathrop, D. K.; Ervin, E. N.; Barrall, G. A.; Keehan, M. G.; Kawano, R.; Krupka, M. A.; White, H. S.; Hibbs, A. H. *J. Am. Chem. Soc.* **2010**, *132*, 1878-1885. (b) Ervin, E. N.; Kawano, R.; White, R. J.; White, H. S. *Anal. Chem.* **2008**, *80*, 2069-2076.

(35) (a) Berge, L. I.; Feder, J.; Jossang, T. *Rev. Sci. Instrum.* **1989**, *60*, 2756-2763. (b) Berge, L. I.; Jossang, T.; Feder, J. *Meas. Sci. Technol.* **1990**, *1*, 471-474.

(36) Lan, W. J.; White, H. S. *PITTCON*, Atlanta, March, **2011**.

(37) Zhang, B.; Galusha, J.; Shiozama, P. G.; Wang, G.; Bergren, A. J.; Jones, R. M.; White, R. J.; Ervin, E. N.; Cauley, C. C.; White, H. S. *Anal. Chem.* **2007**, *79*, 4778-4787.

(38) White, R. J.; Zhang, B.; Daniel, S.; Tang, J. M.; Ervin, E. N.; Cremer, P. S.; White, H. S. *Langmuir* **2006**, *22*, 10777-10783.

(39) (a) Zhang, B.; Zhang, Y.; White, H. S. *Anal. Chem.* **2004**, *76*, 6229-6238. (b) Zhang, B.; Zhang, Y.; White, H. S. *Anal. Chem.* **2006**, *78*, 477-483.

(40) Zhang, Y.; Zhang, B.; White, H. S. *J. Phys. Chem. B* **2006**, *110*, 1768-1774.

(41) (a) White, R. J.; Ervin, E. N.; Yang, T.; Chen, X.; Daniel, S.; Cremer, P. S.; White, H. S. *J. Am. Chem. Soc.* **2007**, *129*, 11766-11775. (b) Kawano, R.; Schibel, A. E. P.; Cauley, C.; White, H. S. *Langmuir* **2009**, *25*, 1233-1237. (c) Ervin, E. N.; White, R. J.; White, H. S. *Anal. Chem.* **2009**, *81*, 533-537.

(42) Lee, S.; Zhang, Y.; Harrell, C. C.; Martin, C. R.; White, H. S. *Anal. Chem.* **2004**, *76*, 6108-6115.

(43) Siwy, Z.; Heins, E.; Harrell, C. C.; Kohli, P.; Martin, C. R. *J. Am. Chem. Soc.* **2004**, *126*, 10850-10851.

(44) (a) Kosinska, I. D. *J. Chem. Phys.* **2006**, *124*, 244707-7. (b) Fulinski, A.; Kosinska, I. D.; Siwy, Z. S. *Europhys. Lett.* **2004**, *67*, 683-689. (c) Feng, J.; Liu, J.; Wu, B.; Wang, G. *Anal. Chem.* **2010**, *82*, 4520-4528.

(45) Wei, C.; Bard, A. J.; Feldberg, S. W. *Anal. Chem.* **1997**, *69*, 4627-4633.

(46) Siwy, Z. S. *Adv. Funct. Mater.* **2006**, *16*, 735-746.

(47) Jin, P.; Mukaibo, H.; Horne, L. P.; Bishop, G. W.; Martin, C. R. *J. Am. Chem. Soc.* **2010**, *132*, 2118-2119.

(48) Karnik, R.; Duan, C.; Castelino, K.; Daiguji, H.; Majumdar, A. *Nano Lett.* **2007**, *7*, 547-551.

(49) Miller, S. A.; Kelly, K. C.; Timperman, A. T. *Lab Chip* **2008**, *8*, 1729-1732.

(50) Xia, F.; Guo, W.; Mao, Y.; Hou, X.; Xue, J.; Xia, H.; Wang, L.; Song, Y.; Ji, H.; Ouyang, Q.; Wang, Y.; Jiang, L. *J. Am. Chem. Soc.* **2008**, *130*, 8345-8350.

(51) Hou, X.; Yang, F.; Li, L.; Song, Y.; Jiang, L.; Zhu, D. *J. Am. Chem. Soc.* **2010**, *132*, 11736-11742.

(52) Vlassiouk, I.; Kozel, T. R.; Siwy, Z. S. *J. Am. Chem. Soc.* **2009**, *131*, 8211-8220.

(53) He, Y.; Gillespie, D.; Boda, D.; Vlassiouk, I.; Eisenberg, R. S.; Siwy, Z. S. *J. Am. Chem. Soc.* **2009**, *131*, 5194-5202.

(54) Yameen, B.; Ali, M.; Neumann, R.; Ensinger, W.; Knoll, W.; Azzaroni, O. *J. Am. Chem. Soc.* **2009**, *131*, 2070-2071.

(55) Ali, M.; Yameen, B.; Cervera, J.; Ramirez, P.; Neumann, R.; Ensinger, W.; Knoll, W.; Azzaroni, O. *J. Am. Chem. Soc.* **2010**, *132*, 8338-8348.

(56) Guerrette, J. P.; Zhang, B. *J. Am. Chem. Soc.* **2010**, *132*, 17088-17091.

(57) (a) Siwy, Z. S.; Gu, Y.; Spohr, H. A.; Baur, D.; Wolf-Reber, A.; Spohr, R.; Apel, P.; Korchev, Y. E. *Europhys. Lett.* **2002**, *60*, 349-355. (b) Cervera, J.; Schiedt, B.; Ramirez, P. *Europhys. Lett.* **2005**, *71*, 35-41.

(58) (a) Woermann, D. *Phys. Chem. Chem. Phys.* **2003**, *5*, 1853-1858. (b) Woermann, D. *Nucl. Instrum. Methods B* **2002**, *194*, 458-462. (c) Woermann, D. *Phys. Chem. Chem. Phys.* **2004**, *6*, 3130-3132.

(59) White, H. S.; Bund, A. *Langmuir* **2008**, *24*, 2212-2218.

(60) Kubeil, C.; Bund, A. *J. Phys. Chem. C* **2011**, *115*, 7866-7873.

(61) Ai, Y.; Zhang, M.; Joo, S. W.; Cheney, M. A.; Qian, S. *J. Phys. Chem. C* **2010**, *114*, 3883-3890.

(62) Lan, W. J.; Holden, D. A.; White, H. S. *J. Am. Chem. Soc.* **2011**, *133*, 13300-13303.

(63) Lan, W. J.; Kubeil, C.; White, H. S., in preparation.

(64) Giuseppe Pelosi (2007). "The finite-element method, Part I: R. L. Courant: Historical Corner". doi:10.1109/MAP.2007.376627.

(65) (a) Cervera, J.; Schiedt, B.; Ramirez, P. *Europhys. Lett.* **2005**, *71*, 35-41. (b) Cervera, J.; Schiedt, B.; Neumann, R.; Mafe, S.; Ramirez, P. *J. Chem. Phys.* **2006**, *124*, 104706.

(66) (a) Daiguji, H.; Yang, P.; Majumdar, A. *Nano Lett.* **2004**, *4*, 137-142. (b) Daiguji, H.; Oka, Y.; Shirono, K. *Nano Lett.* **2005**, *5*, 2274-2280.

CHAPTER 2

NANOPARTICLE TRANSPORT IN CONICAL-SHAPED NANOPORES

2.1 Introduction

This chapter presents a fundamental study of nanoparticle transport phenomena in conical-shaped nanopores contained within glass membranes.[1] The electrophoretic translocation of charged polystyrene (PS) nanoparticles (80 and 160 nm radius) was investigated using the Coulter counter principle (or "resistive-pulse" method), in which the time-dependent nanopore current is recorded as the nanoparticle is driven across the membrane. Particle translocation through the conical-shaped nanopore results in a direction-dependent and asymmetric triangular-shaped resistive pulse. Because the sensing zone of conical-shaped nanopores is localized at the orifice, the translocation of nanoparticles through this zone is very rapid, resulting in pulse widths of ~200 μs for the nanopores used in this study. A linear dependence between translocation rate and nanoparticle concentration was observed from 10^7 to 10^{11} particles/mL for both 80 and 160 nm radius particles, and the magnitude of the resistive pulse scaled approximately in proportion to the particle volume. A continuum theory-based finite-element simulation for computing ion fluxes was combined with a dynamic electric force-based nanoparticle trajectory calculation to compute the position- and time-dependent nanoparticle velocity as the nanoparticle translocates through the conical-shaped nanopore. The computational results were used to compute the resistive pulse current-time response for conical-shaped

pores, allowing comparison between experimental and simulated pulse heights and translocation times. The simulation and experimental results indicate that nanoparticle size can be differentiated based on pulse height, and to a lesser extent based on translocation time.

The Coulter counter, also called the resistive-pulse counter or electrical sensing zone counter, is a traditional device used to detect and size particles (including biological particles and cells), and is broadly employed in manufacturing, health sciences, and environmental analyses.[2] In the Coulter counter, a glass membrane containing an aperture of diameter ranging from micrometers to millimeters is bounded by two electrolyte solutions. A constant electrochemical excitation (such as dc or ac potential) is applied across the aperture to create a "sensing zone," while the resulting ion current is continuously monitored. [3] The baseline current is determined by the electrolyte concentration, the applied potential, and the geometry of the pore.[4] When a particle or a cell enters the pore, it displaces an amount of electrolyte solution equivalent to the particle volume. As a result, the pore resistance momentarily increases during the residence time and the current is attenuated. This transient attenuation generates a pulse that can be measured in the current-time recordings. If the particle is electrically insulating, the amplitude of the pulse is directly proportional to the volume of the particle that produces it. The event frequency is proportional to the particle concentration in the solution, and the translocation time is related to the particle charge and mobility.[5] A variant of Coulter counting is based on membranes containing more than one pore.[6]

The basic principles governing the Coulter counter strategy indicate that smaller nanopores or nanochannels may be able to detect smaller particles[7] and, indeed, the

recent widespread use of protein ion channels and solid-state nanopores for sensing molecules, polymers, and in the structural analysis of biopolymers is a molecule-scale version of the resistive-pulse sensing method.[3,4,6,8] In 1977, DeBlois reported that 60 nm diameter viruses may be rapidly sized in their natural hydrated state as they pass through a single pore.[9] More recently, the Crooks group reported Si_3N_4/PDMS membranes containing individual multi-walled carbon nanotubes (~65 nm in radius). Nanoparticles with different sizes and surface charges were simultaneously analyzed, and the results were shown to be in agreement with other techniques, such as transmission electron microscopy (TEM) and dynamic light scattering (DLS).[10] Sohn and coworkers utilized micro-fabricated nanopores/channels in quartz or PDMS for counting particles as small as 43 nm in radius (~10^8 particles/mL) and for the detection of antibodies binding to latex colloids.[11] Thornton has used electron beam lithography to fabricate cylindrical solid-state nanopores with diameters as small as 20 nm, capable of detecting polystyrene particles by the Coulter counting technique.[12] Zhang et al. also reported the analytical application of cylindrical-shaped silica nanochannels for sensing single 40 nm polystyrene particles and double-stranded DNA.[13]

We have previously described the fabrication and application of glass and fused quartz nanopore membranes (GNM and QNM, respectively) as a lipid bilayer support for ion channel recordings.[14-19] The GNM/QNM contains a single, conical-shaped nanopore embedded within a 25 to 50 μm thick glass/fused quartz membrane at the end of a capillary. The conical shape of the nanopore has potential advantages in resistive-pulse sensing of particles due to strong confinement of the electric field at the small opening. A consequence of the field confinement at the orifice is that the volume of the sensing zone

is of the same scale as the particle, providing potentially higher sensitivity to the particle shape and properties than is possible using a long rectangular channel or cylindrical pore. Additional feasible advantages of glass and quartz nanopores for particle analyses include their favorable electrical properties for high-bandwidth measurements, excellent chemical stability in aqueous and nonaqueous solutions, and a continuous range of orifice sizes (between several nanometers to tens of micrometers).

A recent report described the pressure-driven deformation and translocation of 570 nm radius soft microgel particles through GNMs with radii as small as 375 nm.[20] Herein, we describe a fundamental study of electrophoretically-driven translocation of hard particles through conical-shaped glass nanopores, with a focus on understanding the translocation current-time characteristics using computational simulations. Ion transport in conical-shaped nanopores has been explored extensively in recent years, both experimentally and computationally, due to the phenomenon of ion current rectification, which refers to non-ohmic electrical behavior observed in nanopores of asymmetric geometry.[21,22] The simulation of the particle translocation reported herein is performed by the coupling of the electrolyte ion fluxes with the motion of a much larger nanoparticle. The asymmetry of a conical-shaped pore results in a position-dependent electric field within the pore, and thus, the velocity of the nanoparticle varies by an order of magnitude as it translocates through the sensing zone (*vide infra*). In order to compute the particle velocity and resistive pulse shape, we combined continuum-based simulations of ion fluxes with a discrete electric force-based nanoparticle trajectory calculation. The computational results were used to compute the resistive pulse current-time response for conical-shaped pores, allowing for quantitative comparison to experimental results.

2.2 Experimental section

2.2.1 Chemicals and materials

KCl, K_2HPO_4, KH_2PO_4 (Mallinckrodt), Triton X-100 (Sigma-Aldrich), 3-cyanopropyldimethylchlorosilane ($Cl(Me)_2Si(CH_2)_3CN$), and *n*-butyldimethylchloro-silane ($Cl(Me)_2Si(CH_2)_3CH_3$) (Gelest Inc.) were used as received. All aqueous solutions were prepared using water (18 MΩ·cm) from a Barnstead E-pure water purification system. Acetonitrile (HPLC grade, J. T. Baker) was stored over 3-Å molecular sieves. Polystyrene (PS) nanoparticles (160 nm radius: PC02N Lots 5418 (type A) and 9172 (type B) and 80 nm radius: PC02N Lots 3 (type A) and 2254 (type B), Bangs Laboratories, Fishers, IN) with surface carboxylic acid (-COOH) functional groups were dispersed in KCl solution as received. Particle surface group density and mobility are listed in the Appendix.

2.2.2 Glass nanopore membrane (GNM) fabrication and surface modification

GNMs were fabricated according to a previous report. Briefly, the preparation involves the following five steps: (1) a 2 cm length piece of 25 μm diameter Pt wire (Alfa-Aesar, 99.95%) is attached to a W rod (0.254 mm diameter, FHC, Inc.) using Ag conductive paste. The Pt tip is electrochemically etched to produce a sharp tip; (2) the sharpened Pt tip is sealed in a glass capillary (Dagan Corp., Prism glass capillaries, SB16, 1.65 mm outer diameter, 0.75 mm inner diameter, softening point 700 °C) using a H_2/air flame; (3) the capillary is polished until a Pt nanodisk is exposed. This process is monitored by an electrical continuity circuit; (4) the exposed Pt nanodisk is then etched in a 20% $CaCl_2$ solution by applying a 5.9 V ac voltage between the Pt nanoelectrode and a

Pt wire counter, after which the entire Pt wire is gently pulled from the glass to yield a conical-shaped nanopore. The small opening radius of the GNM (r_i) is computed from the dc electrical ohmic resistance (R) of the GNM measured in a 1.0 M KCl solution at room temperature;[23] (5) the GNM is thoroughly rinsed with H_2O, soaked in 1.0 M HNO_3 for 10 min, followed by rinsing in H_2O, C_2H_5OH, and CH_3CN; afterwards the GNM is immersed overnight in CH_3CN solution containing 2% v/v $Cl(Me)_2Si(CH_2)_3CH_3$ or $Cl(Me)_2Si(CH_2)_3CN$, resulting in covalent attachment of a monolayer of either n-butyl silane or cyanopropyl silane to both exterior and interior glass surfaces. Finally, the modified GNMs are rinsed thoroughly in CH_3CN and C_2H_5OH to remove excess silane.

2.2.3 Nanoparticle characterization

ζ-potential measurements were performed using a NICOMP 380ZLS Zeta Potential Analyzer (Agilent Technologies, Inc.).

2.2.4 Cell configuration, data acquisition, and computational simulations

A Dagan Cornerstone Chem-Clamp potentiostat was interfaced to a computer through a PCI 6251 data acquisition board (National Instruments). Current-time (*i*-*t*) recordings were recorded using in-house virtual instrumentation written in LabVIEW (National Instruments) at a sampling frequency of 100 kHz. A 3-pole Bessel low-pass filter was applied at a cut-off frequency of 10 kHz. The GNM was immersed in a 0.01 M KCl solution (pH 6.9) and PS nanoparticles were uniformly dispersed into the solution. A potential difference was applied across the GNM using Ag/AgCl electrodes. A schematic illustration of the experimental setup is presented in Figure 2.1. The finite-element simulations were carried out with COMSOL Multiphysics 3.5a (Comsol, Inc.) using a high-performance desktop computer.

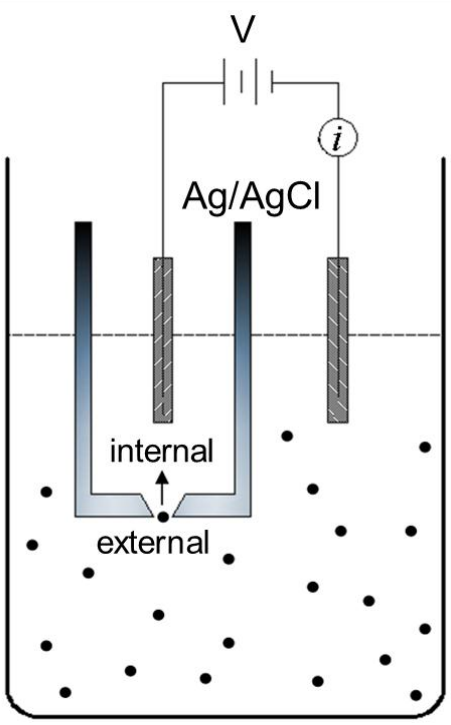

Figure 2.1. Schematic illustration of the GNM and particle detection system.

2.3 Results and discussion

2.3.1 Silanization and characterization of the GNM

The GNM surface displays siloxane bonds, silanol (Si-OH) groups, and silicic acid ($Si\text{-}O^-$) groups.[24] The terminal silanol groups dissociate to generate a negatively charged surface.[25] The negative charges on the glass surface repel the negatively charged PS nanoparticles, possibly hindering their entry into the pores. Thus, in order to reduce the negative surface charges, the GNM was silanized with *n*-butyldimethylchlorosilane or 3-cyanopropyldimethylchlorosilane. Because the silanes contain a single reactive Si-Cl bond, the surface chemical modification yields a monolayer that exposes a terminal-CH_3 or terminal-CN group to the solution. However, the silanization yields a surface coverage of only ~60%,[26] leaving some negative charges on the glass surface. Ion current rectification in GNMs, which results from the charge on the interior pore surface, is significantly reduced in a 0.01 M KCl solution after silanization.

The radii of small orifices of the GNMs were determined from the ionic resistance of the nanopore in a 1.0 M KCl solution. The ionic current was measured as a function of the voltage between internal and external Ag/AgCl electrodes. From the slope of *i*-*V* curve, the radius (r_i) was calculated using the expression $r_i = 18.5/R$.[17] The radii of the pores used in the studies below were 230, 240, and 250 nm with an estimated relative uncertainty of ~10%.

2.3.2 Detection of 160 and 80 nm radius PS particles

Figure 2.2 shows *i-t* recordings for a 250 nm radius GNM in a 0.01 M KCl solution containing negatively charged 160 nm radius (type A) PS particles at concentrations ranging from 10^7 to 10^{11} particles/mL. Individual pulses are observed in the *i-t* trace, corresponding to the translocation of nanoparticles through the GNM. While the pulse heights are relatively uniform, a few larger pulses are also seen, as shown in Figure 2.2d. This is due to the translocation of larger or aggregated particles, or to the finite probability of simultaneous translocation of multiple particles, resulting in a relatively high pulse with a longer duration time.[20, 27] More coincident events are observed at higher particle concentrations.

The translocation of PS nanoparticles is driven by the electrophoretic force imposed by the applied voltage between the Ag/AgCl electrodes. The transference numbers of potassium ion (K^+) and chloride ion (Cl^-) are nearly equal (0.4902 for K^+ and 0.5098 for Cl^-) in 0.01 M KCl solution[28]. With the increase of KCl concentration from 0.01 to 0.1 M, the ζ-potentials of both 160 and 80 nm radius PS particles decreased from ~-35 mV to less than -0.5 mV (Appendix). Correspondingly, the average electrophoretic mobility of PS particles in the solution and the translocation event frequency decreased significantly. Thus, the 0.01 M KCl solution (pH 6.9) was used as the electrolyte solution.

The average normalized pulse height corresponding to 160 nm radius particle translocation is ~3.7% for a 250 nm radius GNM at V_{app} = 200 mV. The current pulse associated with each particle translocation has an asymmetrical triangular shape (shown in Figure 2.2f), which reflects the geometries of the conical pore and spherical particle. Previous finite-element simulations demonstrate that the mass-transfer resistance inside a

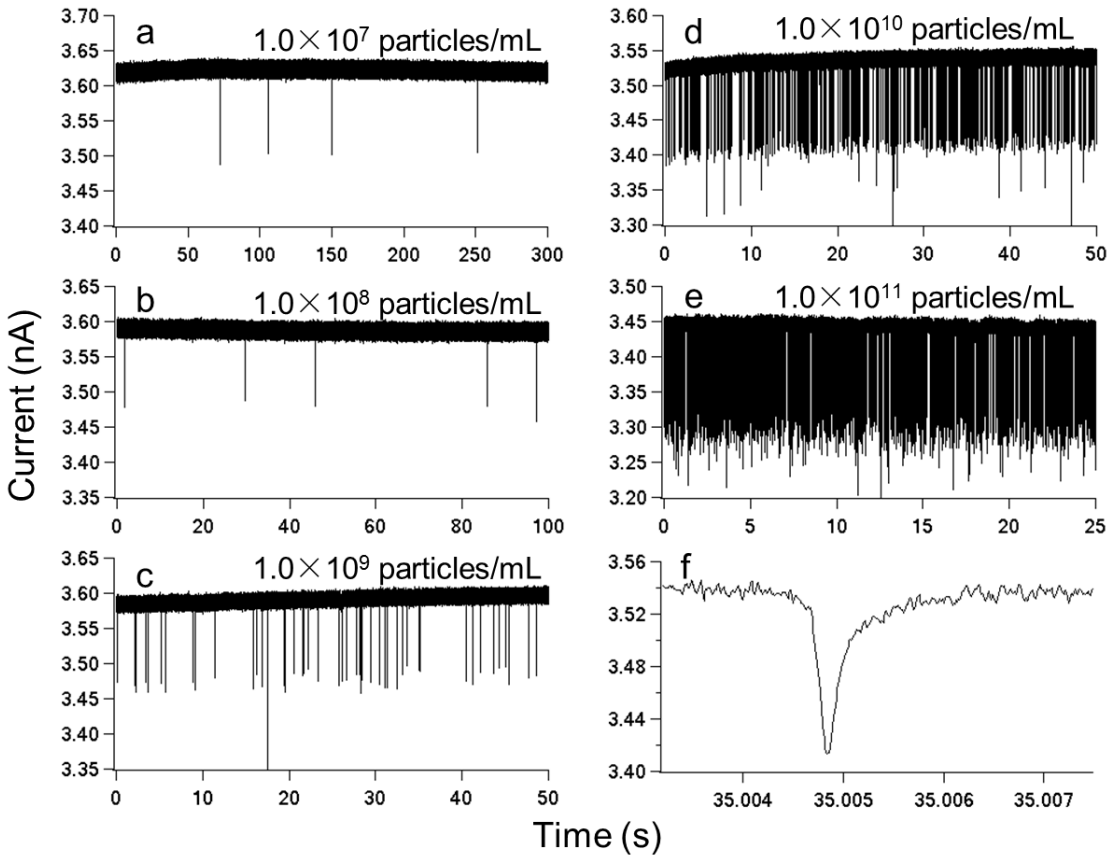

Figure 2.2. Current-time recordings for a 250 nm radius GNM in a 0.01 M KCl solution containing 0.1% Triton X-100 in the presence of 160 nm radius PS particles at different concentrations: (a) 1.0×10^7; (b) 1.0×10^8; (c) 1.0×10^9; (d) 1.0×10^{10}; (e) 1.0×10^{11} particles/mL; and (f) a typical individual translocation pulse. Applied voltage: 200 mV internal vs. external.

conical-shaped nanopore is localized at the small pore orifice,[29] and thus the increase in resistance during translocation is largest when a nanoparticle is in proximity of the pore orifice. Correspondingly, a resistive pulse in the *i-t* recordings occurs as the particle passes through the orifice. In the case of cylindrical pore, however, the resistance of the pore is approximately constant and the current is constant as a particle travels through the pore, resulting in a square-wave pulse in the current-time recording.[11] The average duration time (half-height pulse width) of 160 nm radius particle translocation events through the conical-shaped pore is ~230 ± 40 μs at 200 mV, based on an average of 1455 events (Appendix).

At constant applied voltage and for any combination of nanopore and nanoparticle, a linear dependence is observed between the particle translocation event rate and the particle concentration. Figure 2.3 shows log plots of the event rate for 160 and 80 nm radius particles translocating through 250 and 240 nm radius nanopores, respectively. The slopes of the plots of log (events/s) vs. log (particles/mL) are 0.96 ± 0.02 and 1.01 ± 0.01, respectively, over a range of four orders of magnitude range (10^7 to 10^{11} particles/mL). The low event rate at the lowest particle concentrations (~10^{-2} events/s) potentially limits analytical applications; optimization of event rate has not been a focus of this investigation. The offset between the two calibration lines, corresponding to a factor of ~2.5 higher count rate for 160 nm radius particles through the 250 nm radius GNM, relative to 80 nm radius particles through the 240 nm radius GNM, is not well understood at this time. We observe differences of similar magnitude in event rate using other combinations of nanoparticles and GNMs. We speculate that these differences may reflect the S/N ratio change, or entrance effects due to the similar sizes of the

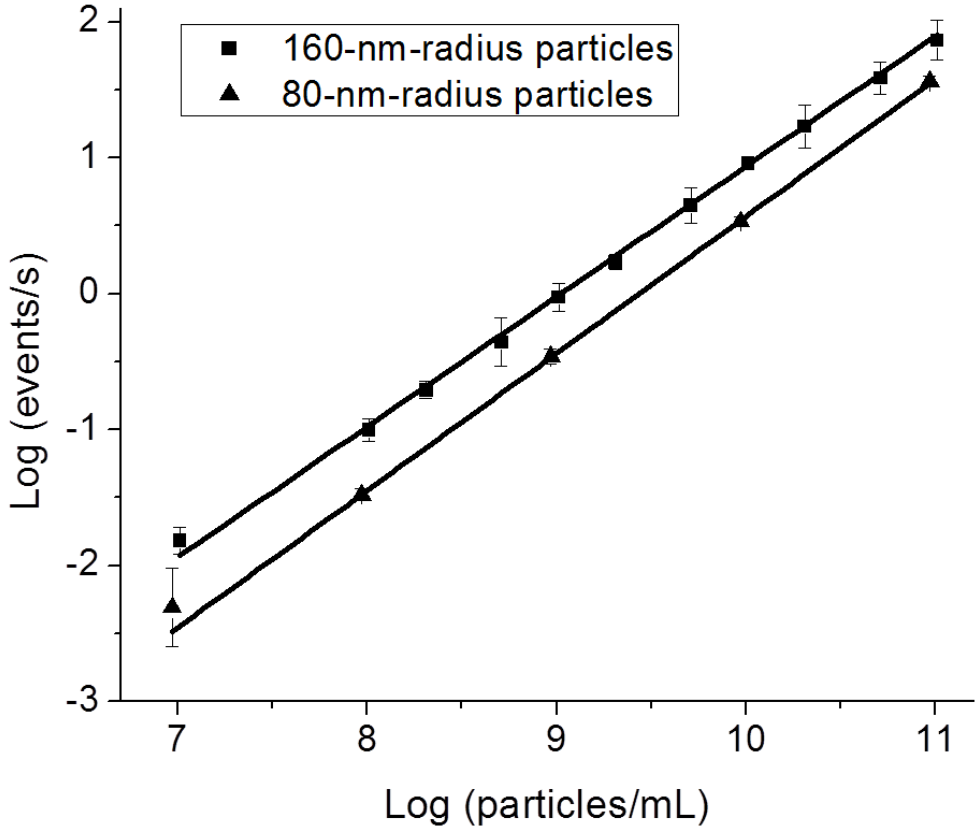

Figure 2.3. Particle translocation rate as a function of particle concentration. The data were obtained in a 0.01 M KCl solution containing 0.1% Triton X-100 in the presence of 160 and 80 nm radius negatively-charged PS particles. The slopes of the best-fit straight lines were 0.96 ± 0.02 for 160 nm radius particles and 1.01 ± 0.01 for 80 nm radius particles. Applied voltage: 200 mV internal vs. external.

particles and pore orifices, or to differences in the effectiveness of neutralizing the GNM surface charge via silanization. Regardless, a semiquantitative theoretical or computational prediction of event rate is beyond our current capabilities. However, empirical calibration, such as that presented in Figure 2.3, would be useful in quantitative analysis of particle concentration.

2.3.3 Simulation of particle translocation through a conical-shaped pore

Quantitative prediction of the pulse height and duration is complicated by the coupling of the calculation of the fluxes of electrolyte ions with the motion of a much larger nanoparticle. In addition, the asymmetry of conical-shaped pore results in a position-dependent electric field, and thus, the nanoparticle velocity varies continuously as it translocates through the pore.

In order to determine the resistive pulse shape, we combined a finite-element simulation based on continuum theory to calculate ion fluxes, with an electric force-based nanoparticle trajectory calculation to compute the position-dependent nanoparticle velocity and ion current as the nanoparticle translocates through the conical-shaped nanopore. The computational results were then used to compute the resistive pulse *i*-*t* response for conical-shaped pores, allowing comparison between experimental and simulated pulse heights and translocation times.

The calculation procedure is outlined as follows. Continuum finite-element simulations were used to compute the ion fluxes, potential distribution, and electric field within the nanopore and in the contacting solutions, using input parameters corresponding to the experiment (ion mobilities, bulk concentrations, the GNM geometry, and the applied voltage). We ignored the charge on the GNM surface in the calculation, in

order to assume electroneutrality throughout the system and simplify the simulation. Measurements of the *i*-*V* behavior for the 250 nm radius GNM in KCl solutions indicate a weak degree of ion rectification after surface silanization; thus, we assume that this assumption introduces a modest error in the calculated results.

The ion fluxes and potential distribution are modeled by the Nernst-Planck equation assuming electroneutrality and no convection:

$$\mathbf{J}_i = -D_i \nabla c_i - \frac{z_i F}{RT} D_i c_i \nabla \Phi \tag{2.1}$$

In eq 2.1, $\mathbf{J}_i$, D_i, c_i, and z_i are, respectively, the ion flux vector, diffusion coefficient, concentration, and charge of species *i* in solution. Φ is the local electric potential and *F*, *R*, and *T* are the Faraday's constant, the gas constant, and temperature, respectively. Finite-element simulations are performed to obtain solutions for the ionic current as the nanoparticle translocates through the pore. The geometry of the model, shown in Figure 2.4, is based on a 2D axial symmetric system (cylindrical coordinate) with the pore orifice centered at $z = 0$, $r = 0$ (Figure 2.5a). The orifice radius and length of the GNM were set to be 250 nm and 20 μm, respectively. To approximate the semi-infinite boundary of the experiment, the exterior boundary of the bulk solution in the model was extended to a distance $r = 100$ μm and $z = 60$ μm away from the pore. The glass surface of the nanopore was defined as an uncharged insulating boundary. The electrolyte solution parameters for the ionic species were chosen to reflect a 0.01 M KCl solution ($D_{K+} = 1.957 \times 10^{-9}$ m^2/s, $c_{K+} = 0.01$ M, $z_{K+} = +1$, $D_{Cl-} = 2.032 \times 10^{-9}$ m^2/s, $c_{Cl-} = 0.01$ M, $z_{Cl-} = -1$, T = 298 K).

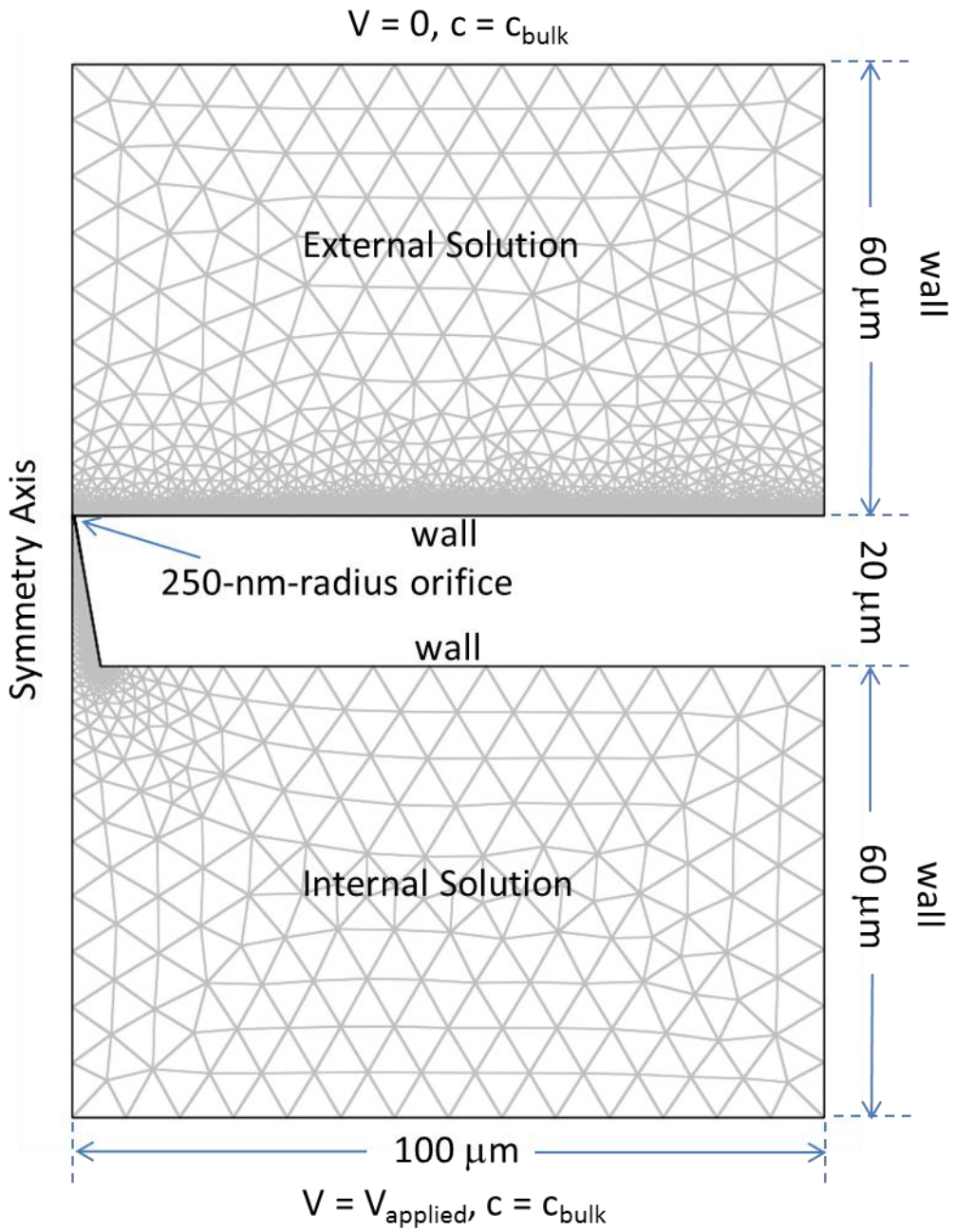

Figure 2.4. The 2D axial symmetric geometry of the GNM used for the finite-element simulations. The mesh size at the nanopore is refined to obtain a more accurate electric field and ion flux. "Wall" indicates an insulating surface. The dimensions of the simulation geometry and boundary conditions of the bulk solutions far from the nanopore are indicated in the figure.

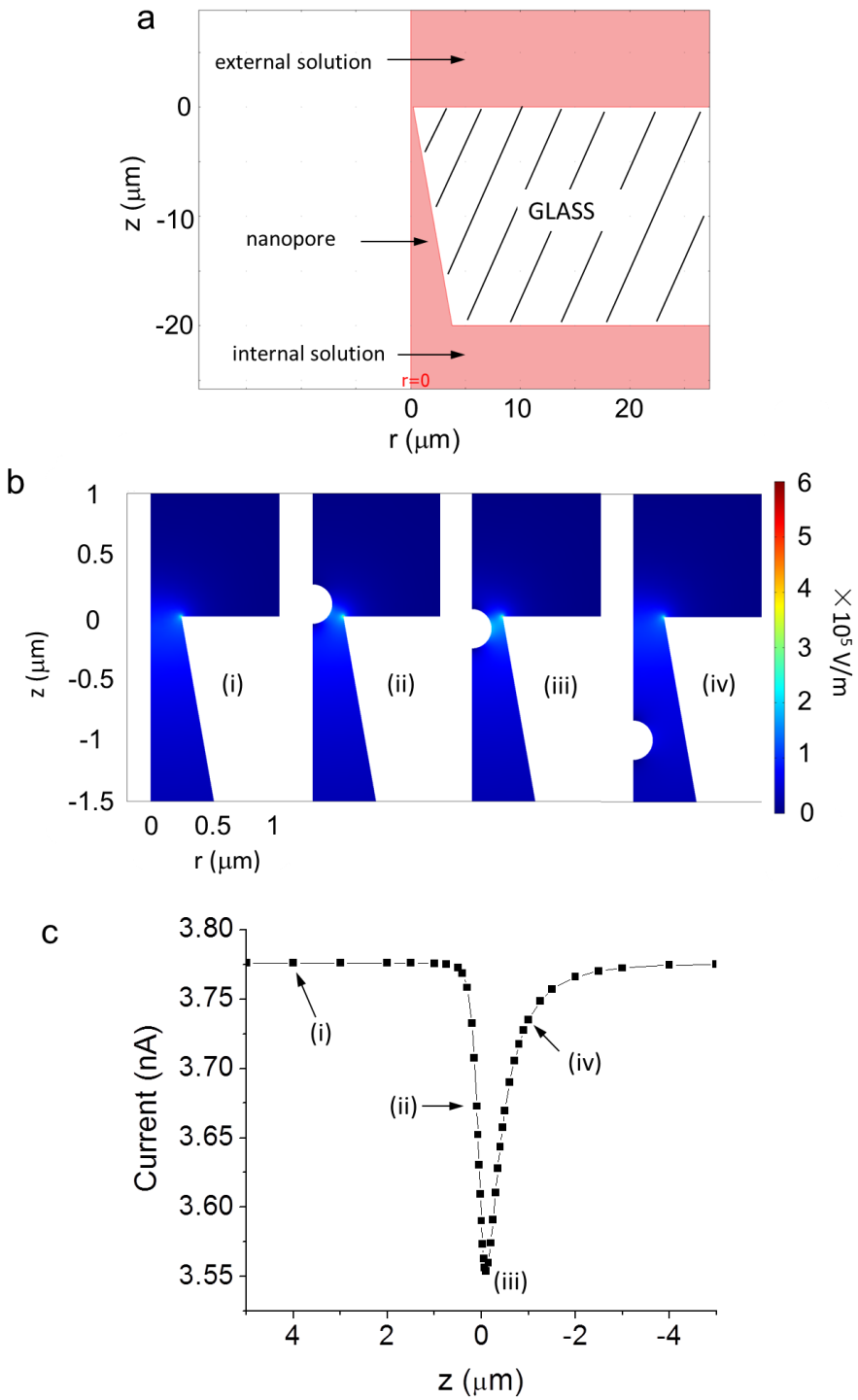

Figure 2.5. Simulated electric-field distribution and current as a function of the position of a 160 nm radius nanoparticle during translocation through a 250 nm radius nanopore (0.01 M KCl solution; applied voltage: 200 mV internal vs. external). (a) The 2D axial symmetric geometry of the GNM used in the finite-element simulation. (b) Electric-field distribution as the particle translocates through the nanopore. (c) Simulated current-position pulse corresponding to a single translocation; z = 0 corresponds to the location of the pore orifice.

To quantitatively predict the shape of the resistive pulse, the above finite-element simulation of the electric field and ion fluxes was performed simultaneously with a simple dynamics calculation of the nanoparticle's motion. We first computed the electric field and ion fluxes within the 250 nm orifice nanopore in the absence of a nanoparticle (Appendix). A 160 nm radius nanoparticle was then introduced into the simulation as a nonconducting sphere, consistent with the properties of PS nanoparticles used in the experiments. The nanoparticle was moved incrementally in Δz-length steps along the centerline axis of the pore (depending on the distance of the particle away from the pore orifice), as shown in Figure 2.5b, and the corresponding ion fluxes in the presence of the nanoparticle were computed. This manual stepping of the particle through the nanopore generates a current-position (*i*-*z*) pulse, as shown in Figure 2.5c.

Knowledge of the electric force acting on the nanoparticle, as it moves from position to position in the simulation, is required in order to convert the static *i*-*z* pulse into a dynamic *i*-*t* pulse. Because of the conical shape of the nanopore, the electric field is highly nonuniform, resulting in a force and particle velocity that change as a function of position. For forced migration of a charged particle in an electric field, the electrophoretic mobility (μ) is defined as

$$\mu = \frac{v}{E} \tag{2.2}$$

where v is the position-dependent particle velocity and E is the position-dependent electric field. Values of μ for the PS nanoparticles are determined from the experimental ζ-potential measurements, while E is obtained from the finite-element

simulations. Thus, the particle velocity v can be computed from eq 2.2 at any position within the nanopore. For a 160 nm radius PS particle passing through a 250 nm radius GNM, a maximum velocity of 0.28 cm/s is obtained at the pore orifice.

Values of v as a function of position were then used to compute the time, Δt, between the particle moving a distance increment Δz during the simulation, eq 2.3.

$$\Delta z = v\Delta t \tag{2.3}$$

Values of Δz between 25 and 1000 nm were employed, using finer spatial increments when the particle was within the sensing zone, in order to obtain greater computational precision.

Figure 2.6 shows experimental and simulated *i-t* traces for a 160 nm radius nanoparticle translocating through a 250 nm radius GNM at 200 mV applied voltage in the 0.01 M KCl solution. Without any adjustable parameters, the simulation is in semi-quantitative agreement with all aspects of the experiment trace, including baseline current (3.54 (*expt.*) vs. 3.77 nA (*sim.*)), translocation time (τ, defined as the width at half pulse height (230 ± 40 (*expt.*) vs. 235 μs (*sim.*)), and % pulse height (3.7% (*expt.*) vs. 5.9% (*sim.*)). The differences in simulated and experimental values are likely due to the approximation of assuming uncharged GNM and particle surfaces. (Note that while the particle charge is implicitly contained within the measured value of μ, the charge distribution on the particle surface and its influence on the instantaneous pore conductivity are ignored).

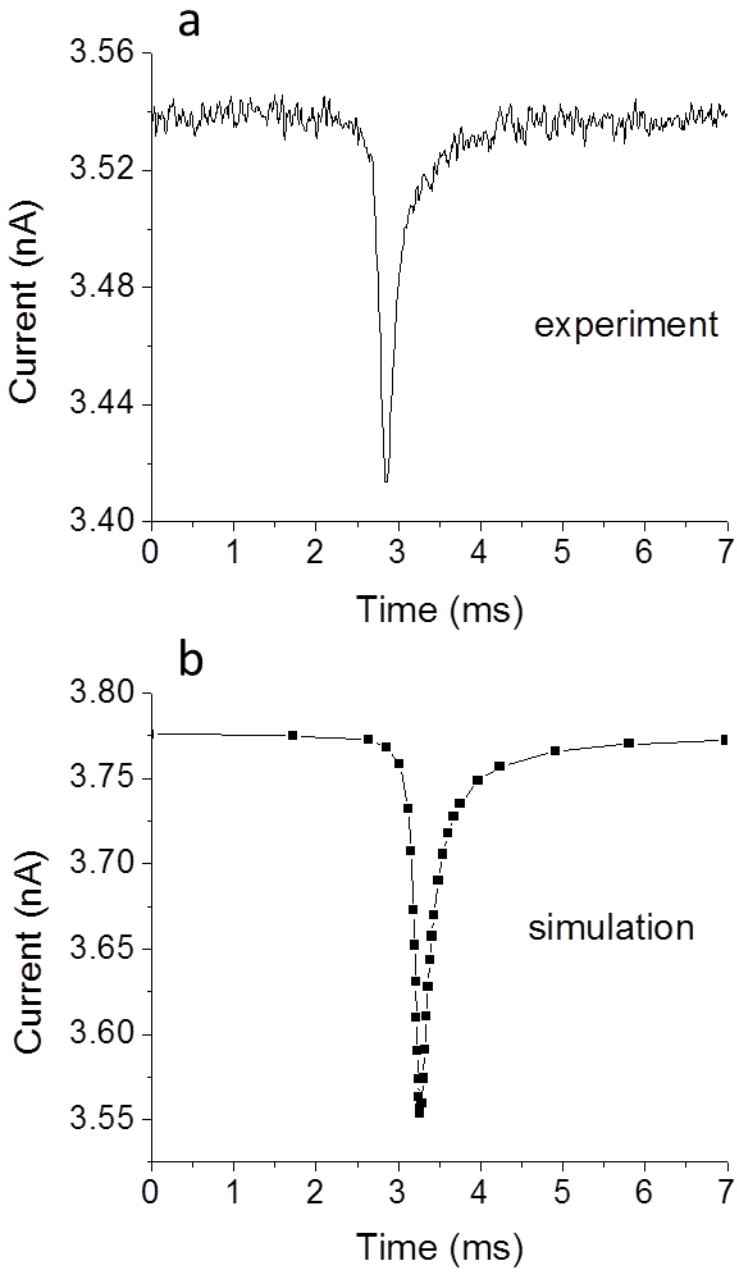

Figure 2.6. Experimental (a) and simulated (b) current-time pulses corresponding to the translocation of a single 160 nm radius PS nanoparticle through a 250 nm radius nanopore in a 0.01 M KCl solution. Applied voltage: 200 mV internal vs. external.

During particle passage, the simulated and experimental current first drops steeply to the peak value when a particle moves from the exterior solution to the disk-shaped pore orifice, and then slowly increases back to the baseline as it moves through the conical-shaped pore interior (Figure 2.6). The asymmetrical triangular shape of current pulse largely reflects the electric-field distribution within the truncated conical pore geometry. The electric-field distribution inside a 250 nm radius GNM in the absence of nanoparticles indicates that the similarity in the shapes of the *i-t* resistive pulse and the electric-field distribution is clear (Appendix).

Results from additional translocation simulations demonstrate τ to be related to the ratio of pore to particle radii ($r_{pore}/r_{particle}$), as shown in Figure 2.7a. As $r_{pore}/r_{particle}$ increases, at constant voltage (200 mV), the sensing zone inside the pore increases relative to the particle size. In addition, the electric field inside the sensing zone decreases as r_{pore} increases, resulting in the larger values of τ. Our simulations indicate that τ increases in approximate proportion to $(r_{pore}/r_{particle})^2$. Normalized resistive pulse heights ($\%\Delta i$) decrease in inverse proportion to $(r_{pore}/r_{particle})^{3.2}$, Figure 2.7b, in approximate agreement with the expectation that the resistive pulse height is proportional to the volume of electrolyte excluded by the translocating particle.

2.3.4 Translocation analysis in mixed nanoparticle solutions

Figure 2.8 shows an *i-t* recording for a 0.01 M KCl solution containing both 80 and 160 nm radius particles (Type B) at a concentration ratio of ~10:1. A 230 nm radius GNM and an applied voltage of 600 mV were employed in this experiment. The normalized pulse heights, measured from the center of the baseline signal, are 2.7% and 0.5% for the 160 and 80 nm radius particles, respectively. The ratio of pulse heights, is

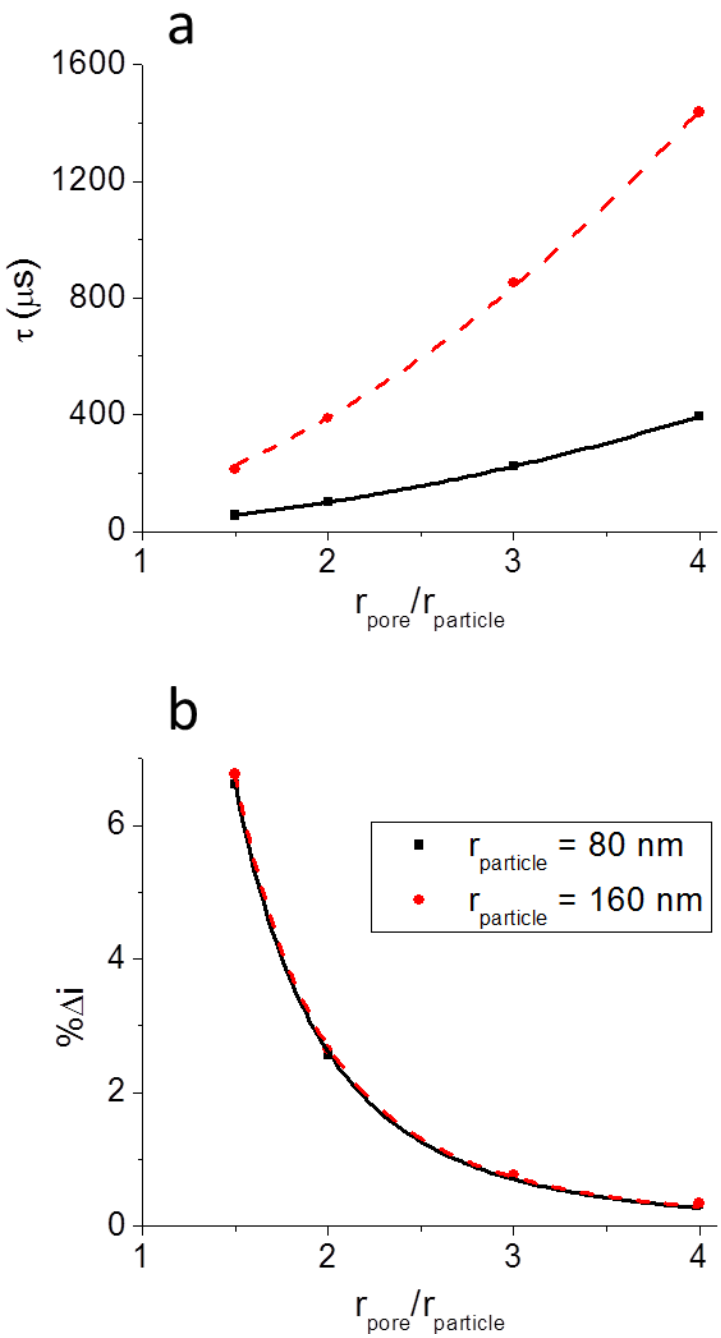

Figure 2.7. (a) Computed values of τ as a function of $r_{pore}/r_{particle}$. The best fit curves are $y = 25.5 \cdot x^{1.98}$ for 80 nm radius particles, and $y = 106 \cdot x^{1.88}$ for the 160 nm radius particles. (b) Computed values of %Δi as a function of $r_{pore}/r_{particle}$. The best fit curves to the values are $y = 24.5 \cdot x^{-3.23}$ for 80 nm radius particles and $y = 24.7 \cdot x^{-3.2}$ for 160 nm radius particles.

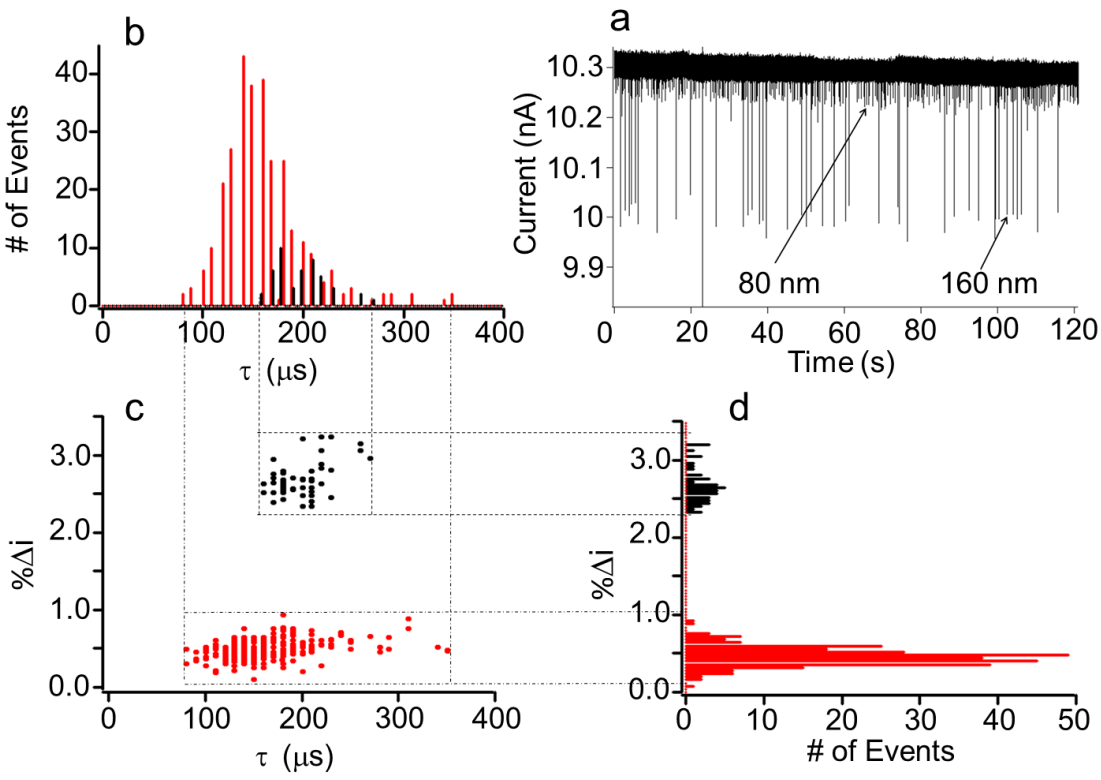

Figure 2.8. (a) Current-time recordings for a 230 nm radius GNM in 0.01 M KCl solution containing 80 (1.0×10^9 particles/mL) and 160 nm radius (1.0×10^8 particles/mL) particles at 600 mV (internal vs. external). (b) Histogram of translocation time (τ). (c) 2D histogram of %Δi vs. τ. (d) Histogram of percentage pulse height (%Δi).

~5.4, slightly lower than the predicted ratio of pulse heights (~8.8), a consequence of electronic filtering of the signal. In comparison with the pulse heights generated by the 160 nm radius particles translocation through the previously-mentioned 250 nm radius pore (3.7%), the smaller pulse height for a particle of the same size using the 230 nm radius pore (2.7%) is probably due to the differences of effectiveness in neutralizing the pore surface charge via silanization. The translocation times are 160 ± 40 μs for 80 nm radius particles (298 events) and 200 ± 30 μs for 160 nm radius particles (46 events). The translocation times of 80 nm radius particle are more dispersed than that of 160 nm radius particle, due to the poorer S/N ratio for the smaller resistive pulse, making it difficult to measure τ values for the smaller, faster moving particle. Nevertheless, the cluster histogram of $\%\Delta i$ vs. τ, as shown in Figure 2.8, demonstrates that individual particle events are cleanly separated, allowing for the characterization of particle sizes and concentrations in mixed particle solutions.

2.4 Conclusions

Conical-shaped GNMs have been applied to the detection and analysis of 80 and 160 nm radius PS nanoparticles based on the resistive-pulse technique. A linear dependence has been found between the count rate and the particle concentration over the range 10^7 to 10^{11} particles/mL. The asymmetrical triangular current pulse for the translocation through the GNM arises from the non-uniform electric field within the pore. Computer simulations combining continuum theory and an electric field based nanoparticle trajectory calculation, without any adjustable parameters, yield predictions of the observed resistive pulses that are in semiquantitative agreement with the experimental observations. Particles with different sizes result in variable current

decreases when passing through the pore, which provide an efficient means for simultaneous differentiation of particles.

Our ability to reliably detect nanoparticles is currently limited to particles of radius greater than ~40 nm, a consequence of electronic filtering of the resistive pulse signal. A 10 nm radius particle is predicted (from simulations) to generate a 5 μs pulse as it translocates through a 30 nm radius GNM, well beyond accurate recording using electronics with 10 kHz filtering. This limitation is not inherent to conical-shaped pores, and efforts are underway to improve the temporal resolution. The origin of this limitation lies in the nanoscale dimensions of the sensing zone; however, in the absence of electronic limitations, the small volume of the conical-shaped sensing zone allows for higher temporal resolution in sensing the physical and chemical properties of both hard and soft nanoparticles. An example of this feature of resistive pulse analysis using conical-shaped pores is the ability to electrically monitor the deformation of microgel particles during translocation.[20] Current research is thus focused on improving the electronics to allow analysis of particles of significantly smaller dimensions.

2.5 Appendix

In this Appendix, example GNM *i*-*V* curves, ζ-potential and other particle properties, an example particle translocation histogram, a schematic of the 2D axial symmetric geometry used in the finite-element simulations, and the simulated electric-field distribution in the nanopore are shown in Figure 2.9-2.12 and Table 2.1, respectively.

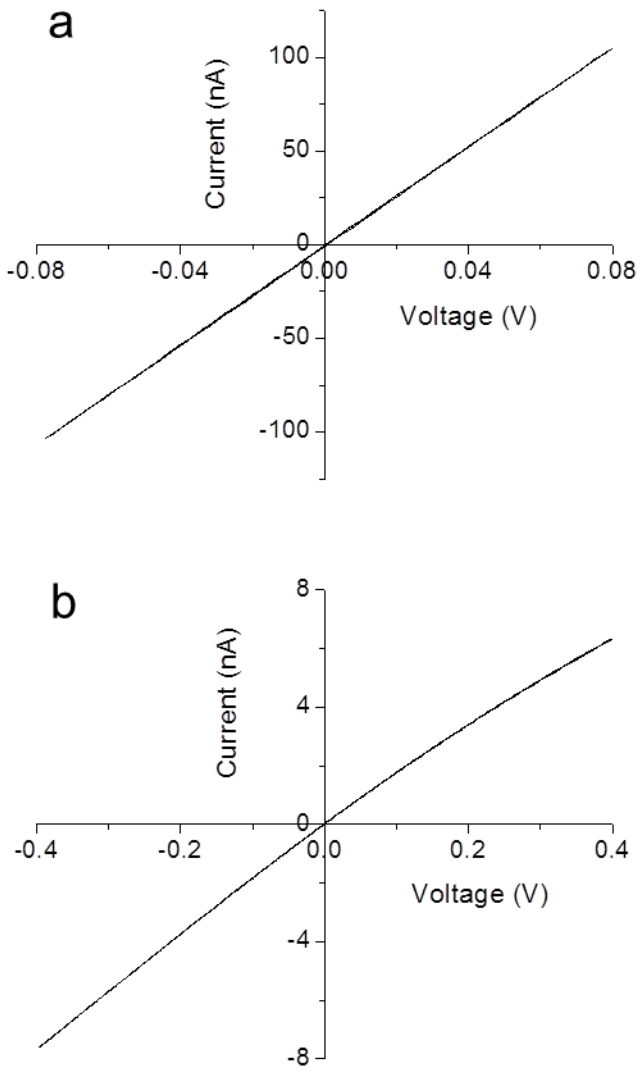

Figure 2.9. The *i*-*V* responses of a silanized 250 nm radius GNM in (a) 1.0 M and (b) 0.01 M KCl solutions.

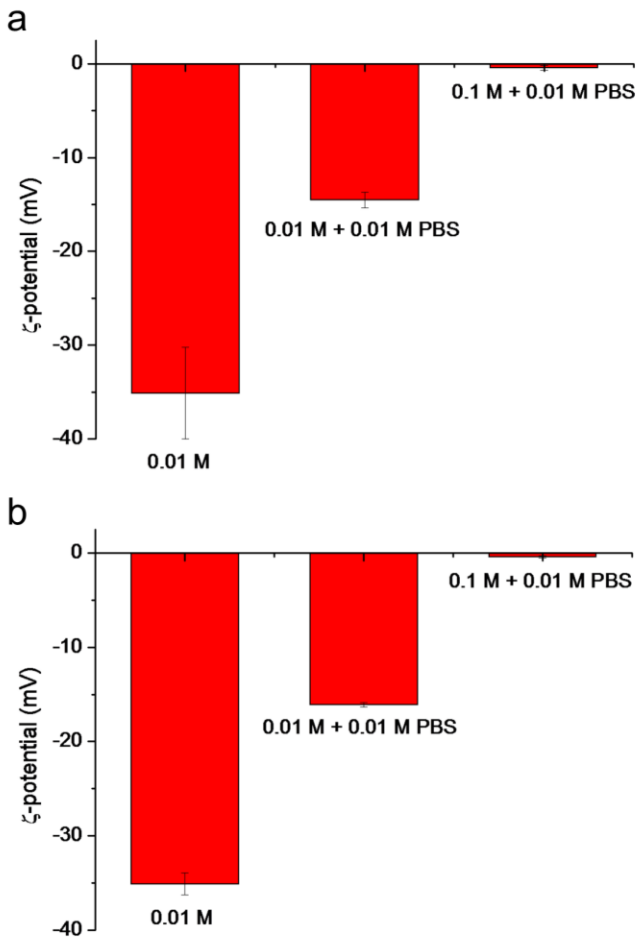

Figure 2.10. ζ-potentials of (a) 160 and (b) 80 nm radius -COOH PS particles in different KCl solutions. The nanoparticle concentrations were 1.0×10^9 particles/mL and 8.6×10^9 particles/mL, respectively.

Table 2.1. The average mobility of the particles in 0.01 M KCl solution. The 80 nm (type A) and 160 nm (type A) were used for the concentration dependence experiments and the 80 nm (type B) and 160 nm (type B) were used for the mixed experiments (see main text). The average mobility (μ) was measured from the ζ-potential experiments. Γ_{man} is the surface group density on particles provided by the manufacturer. The particle concentration in the mobility measurement is indicated in the table.

Particle Type	μ ($\times 10^{-8}$ $m^2 \cdot s^{-1} \cdot V^{-1}$)	Γ_{man} (groups/particle)	Particle concentration (particles/mL)
80 nm A	2.79	3.38×10^5	8.6×10^9
160 nm A	2.78	1.45×10^6	1.0×10^9
80 nm B	5.17	7.94×10^4	1.0×10^9
160 nm B	5.42	1.45×10^6	1.0×10^8

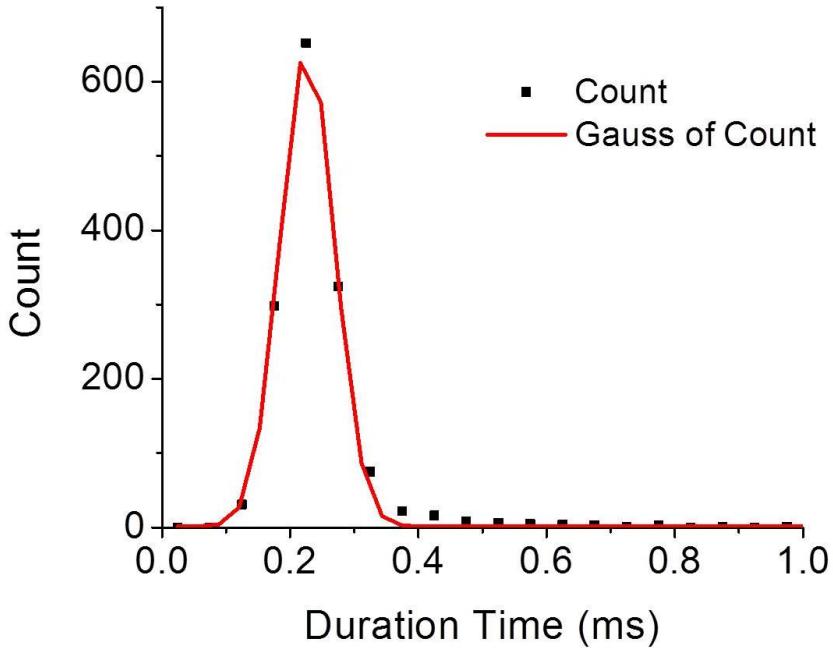

Figure 2.11. Distribution of duration times for 160 nm radius particle translocation in a 250 nm radius GNM at V_{app} = 200 mV. The average duration time (half-height pulse width) of translocation events is ~230 ± 40 μs at 200 mV, based on 1455 events. The red line is drawn to fit the data, assuming a Gaussian distribution.

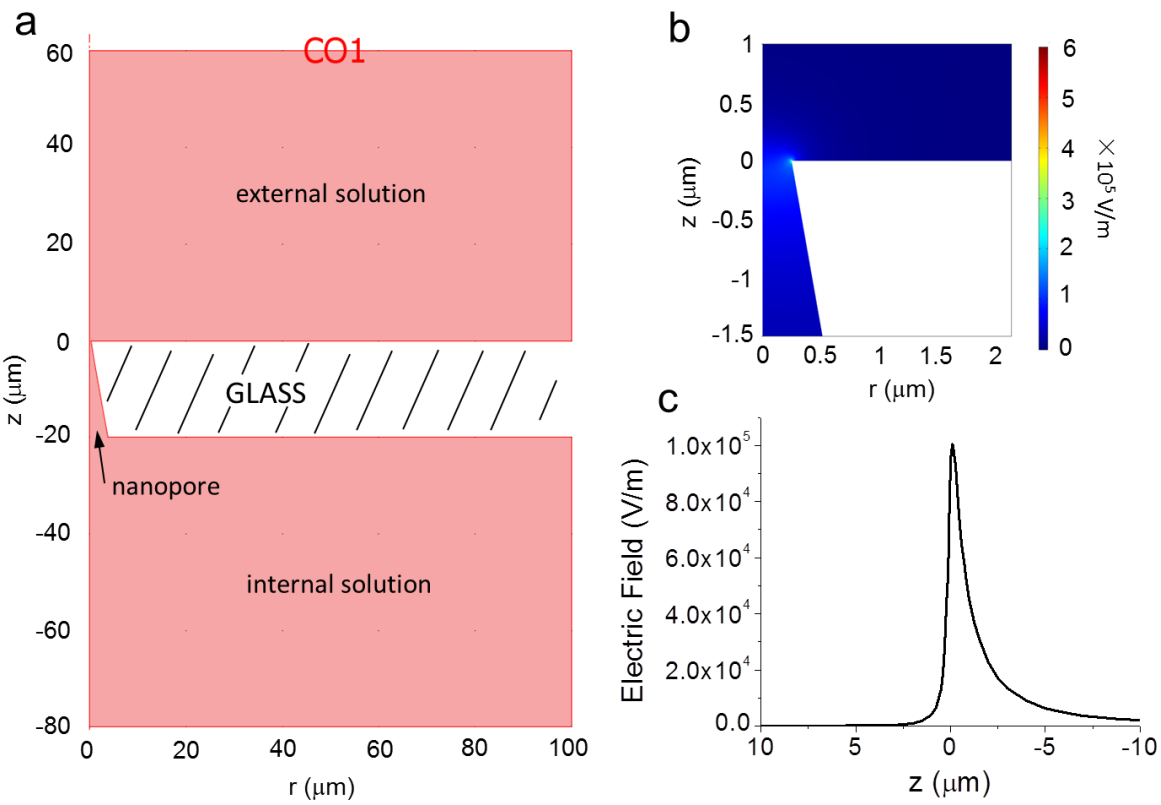

Figure 2.12. (a) The 2D axial symmetric geometry of the 250 nm radius GNM and solution used in the finite-element simulation. (b) Electric-field distribution in the nanopore, internal solutions, and external solutions. (c) The electric field distribution as a function of distance along the central pore axis. The opening of the pore is located at $z = 0$ μm in each figure. Values of $z < 0$ μm correspond to the nanopore interior, while values of $z > 0$ μm correspond to the external solution. Applied voltage: 200 mV internal vs. external.

2.6 References

(1) Lan, W. J.; Holden, D. A.; Zhang, B.; White, H. S. *Anal. Chem.* **2011**, *83*, 3840-3847.

(2) (a) Coulter, W. H. Means for Counting Particles Suspended in a Fluid. U.S. Patent 2,656,508, 1953. (b) Williams, W. J.; Beutler, E.; Erslev, A. J.; Lichtman, M. A. *Hematology*, 3rd ed.; McGraw-Hill Book Company: New York, 1983.

(3) (a) Bayley, H.; Martin, C. R. *Chem. Rev.* **2000**, *100*, 2575-2594. (b) Lines, R. W. In *Particle Size Analysis*; Stanley-Wood, N. G., Lines, R. W., Eds; Royal Society of Chemistry: Cambridge, U.K., 1992.

(4) (a) Ho, C.; Qiao, R.; Heng, J. B.; Chatterjee, A.; Timp, R. J.; Aluru, N. R.; Timp, G. *Proc. Natl. Acad. Sci. U.S.A.* **2005**, *102*, 10445. (b) Li, N.; Yu, S.; Harrell, C. C.; Martin, C. R. *Anal. Chem.* **2004**, *76*, 2025.

(5) Murray, R. W. *Chem. Rev.* **2008**, *108*, 2688-2720.

(6) (a) Kobayashi, Y.; Martin, C. R. *Anal. Chem.* **1999**, *71*, 3665. (b) Yu, S.; Lee, S. B.; Martin, C. R. *Anal. Chem.* **2003**, *75*, 1239. (c) Martin, C. R. *Science* **1994**, *266*, 1961.

(7) DeBlois, R. W.; Bean, C. P. *Rev. Sci. Instrum.* **1970**, *41*, 909-916.

(8) (a) Kasianowicz, J. J.; Brandin, E.; Branton, D.; Deamer, D. W. *Proc. Natl. Acad. Sci. U.S.A.* **1996**, *93*, 13770-13773. (b) Gu, L. Q.; Braha, O.; Conlan, S.; Cheley, S.; Bayley, H. *Nature* **1999**, *398*, 686-690. (c) Robertson, J. W. F.; Rodrigues, C. G.; Stanford, V. M.; Rubinson, K. A.; Krasilnikov, O. V.; Kasianowicz, J. J. *Proc. Natl. Acad. Sci. U.S.A.* **2007**, *104*, 8207-8211. (d) Reiner, J. E.; Kasianowicz, J. J.; Nablo, B. J.; Robertson, J. W. F. *Proc. Natl. Acad. Sci. U.S.A.* **2010**, *107*, 12080-12085. (e) Robertson, J. W. F.; Kasianowicz, J. J.; Reiner, J. E. *J. Phys.: Condens. Matter* **2010**, *22*, 454108.

(9) DeBlois, R. W.; Wesley, R. K. A. *J. Virol.* **1977**, *23*, 227-233.

(10) (a) Sun, L.; Crooks, R. M. *J. Am. Chem. Soc.* **2000**, *122*, 12340-12345. (b) Ito, T.; Sun, L.; Crooks, R. M. *Anal. Chem.* **2003**, *75*, 2399-2406. (c) Ito, T.; Sun, L.; Bevan, M. A.; Crooks, R. M. *Langmuir* **2004**, *20*, 6940-6945. (d) Ito, T.; Sun, L.; Crooks, R. M. *Chem. Comm.* **2003**, 1482-1483. (e) Henriquez, R. R.; Ito, T.; Sun, L.; Crooks, R. M. *Analyst* **2004**, *129*, 478-482. (f) Ito, T. Sun, L.; Henriquez, R. R.; Crooks, R. M. *Acc. Chem. Res.* **2004**, *37*, 937-945.

(11) (a) Saleh, O. A.; Sohn, L. L. *Rev. Sci. Instrum.* **2001**, *72*, 4449-4451. (b)Saleh, O. A.; Sohn, L. L. *Proc. Natl. Acad. Sci. U.S.A.* **2003**, *100*, 820-824.

(12) Petrossian, L; Wilk, S. J.; Joshi, P.; Goodnick, S. M.; Thornton, T. J. *J. Phys.: Conf. Ser*. **2008**, *109*, 012028.

(13) Zhang, B.; Wood, M.; Lee, H. *Anal. Chem.* **2009**, *81*, 5541-5548.

(14) Zhang, B.; Zhang, Y.; White, H. S. *Anal. Chem.* **2004**, *76*, 6229-6238.

(15) Zhang, B.; Zhang, Y.; White, H. S. *Anal. Chem.* **2006**, *78*, 477-483.

(16) Zhang, B.; Galusha, J.; Shiozawa, P. G.; Wang, G.; Bergren, A. J.; Jones, R. M.; White, R. J.; Ervin, E. N.; Cauley, C. C.; White, H. S. *Anal. Chem.* **2007**, *79*, 4778-4787.

(17) White, R. J.; Zhang, B.; Daniel, S.; Tang, J. M.; Ervin, E. N.; Cremer, P. S.; White, H. S. *Langmuir* **2006**, *22*, 10777-10783.

(18) White, R. J.; Ervin, E. N.; Yang, T.; Chen, X.; Daniel, S.; Cremer, P. S.; White, H. S. *J. Am. Chem. Soc.* **2007**, *129*, 11766-11775.

(19) Schibel, A. E. P.; Edwards, T.; Kawano, R.; Lan, W. J.; White, H. S. *Anal. Chem.* **2010**, *82*, 7259-7266.

(20) Holden, D. A.; Hendrickson, G.; Lyon, L. A.; White, H. S. *J. Phys. Chem. C* **2011**, *115*, 2999-3004.

(21) (a) Wei, C.; Bard, A. J.; Feldberg, S. W. *Anal. Chem.* **1997**, *69*, 4627-4633. (b) White, H. S.; Bund, A. *Langmuir* **2008**, *24*, 12062-12067. (c) Siwy, Z.; Heins, E.; Harrell, C. C.; Kohli, P.; Martin, C. R. *J. Am. Chem. Soc.* **2004**, *126*, 10580-10581. (d) Siwy, Z. S. *Adv. Funct. Mater.* **2006**, *16*, 735-746. (e) Guerrette, J. P.; Zhang, B. *J. Am. Chem. Soc.* **2010**, *132*, 17088-17091.

(22) (a) Cervera J.; Schiedt, B.; Neumann R.; Mafe, S.; Ramirez, P. *J. Chem. Phys.* **2006**, *124*, 104706. (b) Cervera, J.; Schiedt, B.; Ramirez, P. *Europhys. Lett*. **2005**, *71*, 35-41.

(23) Bard, A. J.; Faulkner, L. R. *Electrochemical Methods: Fundamentals and Applications*; 2nd ed.; John Wiley & Sons: New York, 2001.

(24) Claesson, P. M.; Dedinaite, A.; Poptoshev, E. In *Physical Chemistry of Polyelectrolytes*; Radeva, T., Ed.; Marcel Dekker, Inc.: New York, 2001; Surfactant Science Series Vol. 99, p 462.

(25) Behrens, S. H.; Grier, D. G. *J. Chem. Phys.* **2001**, *115*, 6716-6721.

(26) Fadeev, A. Y.; McCarthy, T. J. *Langmuir* **1999**, *15*, 3759-3766.

(27) Figueiredo, M. M. In *Encyclopedia of Analytical Chemistry*; Meyers, R. A., Ed.; John Wiley & Sons: New York: 2000: pp 5358-5371.

(28) MacInnes, D. A. *The Principles of Electrochemistry*; Dover: New York, 1961; p 85.

(29) White, H. S.; Bund, A. *Langmuir* **2008**, *24*, 2212-2218.

CHAPTER 3

PRESSURE-DRIVEN NANOPARTICLE TRANSPORT ACROSS GLASS MEMBRANES CONTAINING A CONICAL-SHAPED NANOPORE

3.1 Introduction

In this chapter, experimental, theoretical, and finite-element simulation investigations of the pressure-driven translocation of nanoparticles across a conical-shaped glass nanopore membrane (GNM) are presented. The translocation of the particles is experimentally analyzed by measuring the shape of transient pulses when current flowing between two Ag/AgCl electrodes, located on opposite sides of the GNM, is momentarily interrupted as a particle passes through the nanopore. Asymmetric triangular-shaped resistive pulses are observed for the translocation of 120 nm radius particles through a 210 nm radius GNM at a transmembrane pressure between -2 and -160 mmHg. A linear dependence is observed between the particle translocation frequency and the applied pressure. Analytical theory and finite-element simulation for pressure-driven flow through a conical-shaped pore were developed to compute the volumetric flow rate, the position-dependent particle velocity, and the particle translocation frequency. The translocation frequencies computed from theory and simulation as a function of pressure were found to be in agreement with experimental observations. The particle translocation pulse shape was also computed by a combination of finite-element simulation with a dynamic nanoparticle trajectory calculation. Surprisingly, the

simulations demonstrate that pulse widths are nearly independent of the nanopore radius. The independence of pulse width on nanopore size is a consequence of both the solution velocity and the width of the electrical sensing zone increasing in proportion to the orifice radius for conical-shaped pores.[1]

The application of the resistive-pulse principle method (i.e., Coulter counter[2,3]) has increased in recent years due to greatly improved detection sensitivity as the size of synthetic pores and channels are reduced to dimensions that are comparable to those of nanoparticles and macromolecules. In resistive-pulse analysis, nanoparticles or macromolecules present in a weak electrolyte solution are driven through an aperture or a channel in a membrane, either by an electric field (in a stationary solution), or by convective solution flow engendered by a pressure gradient,[2,4] electroosmosis,[5] and salt gradients.[6] Electrodes placed on opposite sides of the membrane are used to record the flux of electrolyte ions, which is momentarily interrupted as the particle or macromolecule passes through the aperture or channel.[7] Resistive pulses are counted to determine analyte concentration, while the pulse duration and height potentially provide information regarding the size and structure of the particle or macromolecule.[8]

We wish to report an investigation of the pressure-driven convective translocation of nanoparticles across a glass membrane containing a single conical-shaped nanopore. Herein, theoretical and finite-element analyses of the pressure and velocity distributions across a nanopore (> 100 nm) of conical geometry are developed, and used to predict the translocation frequency and pulse shape as spherical nanoparticles are driven through the nanopore by an externally applied pressure. Conical nanopores are of special interest in resistive pulse analysis because the sensing zone is localized at the orifice; i.e., the

majority of the resistance of the nanopore is localized to a solution volume of width that is comparable to the radius of the nanopore orifice.[9] Conical pores can be readily fabricated with pore sizes as small as a few nanometers,[10-13] and thus have potential to sense particles and molecules of comparable dimensions, as demonstrated by Martin[14] and Jacobson.[15] While numerous recent reports describe resistive pulse analyses using synthetic cylindrical or conical pores,[16-20] a quantitative analysis of pressure-driven flow and the accompanying transport of particles through a conical pore has not been presented to the best of our knowledge. Willmott, Roberts, Trau, Vogel, and coworkers have recently reported the fabrication of tunable conical nanopores in elastomeric membranes, and their applications in particle detection, discrimination, and sizing, using pressure-driven flow or electrophoresis.[21] Additionally, our laboratory has recently reported electrophoresis-driven transport of charged nanoparticles through conical-shaped nanopores, focusing on how the electric field distribution across the orifice influences the observed pulse shape.[8] Here, we demonstrate, through experiments, theory, and finite-element simulations, a linear dependence of pressure-driven translocation frequency that can be readily predicted, a priori, from the applied transmembrane pressure, radius of the small opening of the nanopore, and solution viscosity. We also show that, unlike flow in a cylindrical nanopore where the volumetric flow rate increases with the fourth power of the pore radius (r^4), the flow rate through a conical nanopore is proportional to the cube of the pore orifice radius (r^3). A consequence of this flow rate dependence is that resistive pulse widths are essentially independent of the nanopore radius.

3.2 Experimental section

3.2.1 Chemicals and materials

KCl, K_2HPO_4, KH_2PO_4 (Mallinckrodt), Triton X-100 (Sigma-Aldrich), 3-cyanopropyldimethylchlorosilane ($Cl(Me)_2Si(CH_2)_3CN$), and *n*-butyldimethylchlorosilane ($Cl(Me)_2Si(CH_2)_3CH_3$) (Gelest Inc.) were used as received. All aqueous solutions were prepared using water (18 MΩ·cm) from a Barnstead E-pure water purification system. Acetonitrile (HPLC grade, J. T. Baker) was stored over 3-Å molecular sieves. Non-functionalized polystyrene (PS) nanoparticles (120 nm radius) from Bangs Laboratories, Fishers, IN (PS02N Lot 5708) were dispersed in buffered 0.1 M KCl solutions as received. ζ-potential was measured by electrophoretic light scattering using a NICOMP 380ZLS Zeta Potential Analyzer (Agilent Technologies, Inc.).

3.2.2 GNM fabrication and surface modification

The GNM was fabricated as described in previous reports from our lab.[10] A conical-shaped nanopore is fabricated in a ~50 μm thick glass membrane at the end of a glass capillary. The half-cone angle of the nanopore was estimated to be 10 ± 1 °.[11] This angle was roughly estimated with an optical microscope. The radius of the small orifice of the GNM was determined to be 210 nm from the ionic resistance of the pore in 1.0 M KCl solution, using the expression $r_i = 18.5/R$ (assuming a half-cone angle of 10 °),[11] with a relative uncertainty of ~10%. The interior and exterior surfaces of the GNM were silanized in acetonitrile with *n*-butyldimethylchlorosilane or 3-cyanopropyldimethylchlorosilane to reduce the negative charge on the glass surface.

Fabrication of GNMs requires significant skill and training, but an experienced student can produce GNMs with high yields (>50%). The GNMs are mechanically robust;

indeed, the GNM used in this chapter has been continuously used for over one year in particle counting experiments. Clogging of the nanopore during particle analyses occurs occasionally due to particle aggregates, especially at high pressures that correspond to very large volumetric flow rates. Particle aggregates are removed by rinsing the external and internal surfaces with H_2O. Gentle sonication on the GNM in H_2O is also useful in removing particle aggregates, but care must be taken not to damage the pores.

3.2.3 Cell configuration and data acquisition

A Pine RDE3 potentiostat and a Dagan Chem-Clamp potentiostat was interfaced to a computer through a PCI 6251 data acquisition card (National Instruments). Current-time (*i*-*t*) curves were recorded at a sampling frequency (data acquisition rate) of 100 kHz using in-house virtual instrumentation written in LabVIEW (National Instruments). A 3-pole Bessel low-pass filter was applied at a cut-off frequency of 10 kHz. Electrical filtering of the resistive pulse due to the low-pass filter is described in the Results and Discussion section. A schematic illustration of the experimental setup is presented in Figure 3.1. The GNM capillary was filled with a 0.1 M KCl solution containing 10 mM K_2HPO_4 / KH_2PO_4 buffer and 0.1% Triton X-100 (pH 7.5) and immersed in a 5 mL glass vial containing the same electrolyte. PS nanoparticles were uniformly dispersed into the external solution. A potential difference was applied across the GNM using Ag/AgCl electrodes placed inside the GNM capillary and in the exterior bulk solution. The Ag/AgCl electrodes were prepared by oxidation of clean Ag wires in Clorox solution for 15 min. Pressure was applied across the nanopore using a gastight syringe and measured by a pressure gauge. The pressure across the membrane is defined as the pressure inside the glass capillary relative to the external solution, which is at atmospheric pressure.

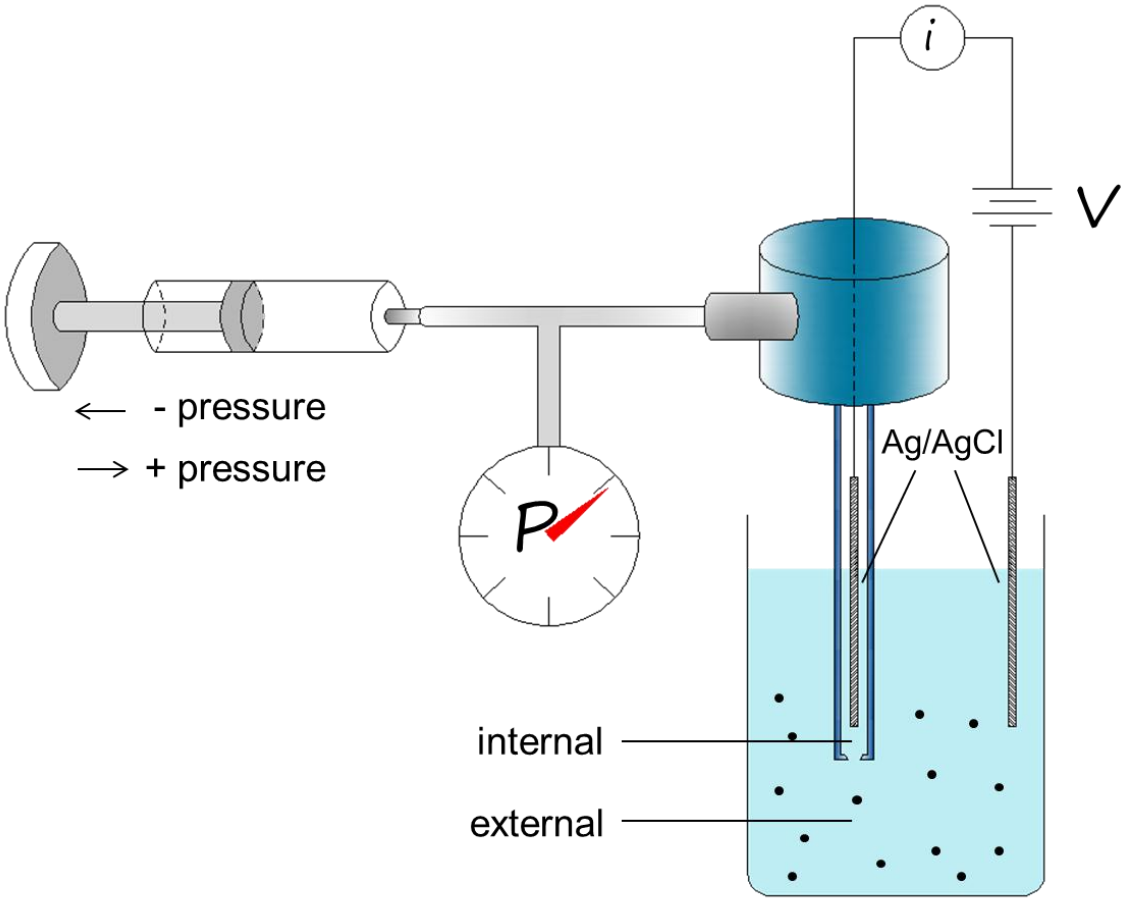

Figure 3.1. Schematic illustration of the pressure-driven particle analysis system. Particles are placed in the external bulk solution and driven through the conical nanopore into the capillary by applying a negative internal pressure. Particle translocation through the nanopore is recorded by a transient decrease in the current between the Ag/AgCl electrodes. All pressures and voltages reported in this chapter are defined as the values inside the capillary (internal) vs. the values in the bulk solution (external).

Particles were driven from the bulk solution into the pore by applying a negative pressure, creating a flow through the nanopore.

3.2.4 Computational analysis and simulations

i-t recordings were plotted with Igor Pro software 6.0.2.4 (WaveMetrics, Lake Oswego, U.S.A.). Current pulses were analyzed by QuB software package 1.5.0.20 (State University of New York at Buffalo, available at www.qub.buffalo.edu/). Finite-element simulations of the pressure distribution, flow velocity, and ionic current within the conical nanopore were performed with COMSOL Multiphysics 3.5a (Comsol, Inc.) on a high-performance desktop computer (Intel Core i7 CPU with 8 GB RAM).

3.3 Results and discussion

3.3.1 Analysis of 120 nm radius PS nanoparticles in KCl solution

Figure 3.2 shows an example *i-t* trace of a 210 nm radius pore in 0.1 M KCl solution containing 10 mM K_2HPO_4 / KH_2PO_4 buffer and 0.1% Triton X-100 in the presence of 120 nm radius PS particles (1.3×10^9 particles/mL). A voltage of 200 mV (internal vs. external) was applied, generating a baseline current of ~28 nA. In the absence of an applied pressure (0-15 s in the *i-t* trace), electrophoresis and diffusion of the PS particles through the nanopore results in a small number of resistive pulses (0.2 events/s), indicating a small negative surface charge density on the particles. Although the surface of the PS particles is not intentionally functionalized, it is still slightly negatively charged at neutral pH because the sulfate groups from the initiator in the emulsion polymerization process terminate the polymer chains at the particle surface.[22] The ζ-potential of the 120 nm radius particles in a 0.1 M KCl solution (pH = 7.5) was measured to be less than -2 mV, indicating a very small negative surface charge density.

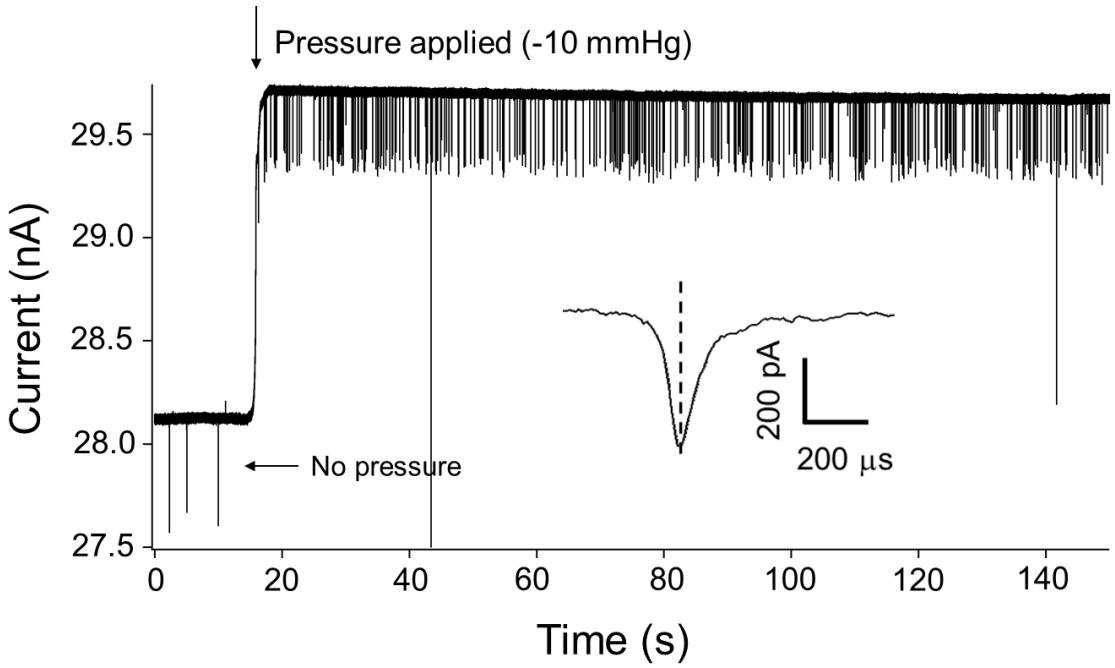

Figure 3.2. *i-t* recording for a 210 nm radius GNM in a 0.1 M KCl solution (pH 7.5) in the presence of 120 nm radius PS particles (1.3×10^9 particles/mL) at constant voltage (200 mV), without (0 - ~15 s) and with -10 mmHg applied pressure (> ~15 s). Inset: a typical individual pulse selected from the recording corresponding to translocation of one particle. Applied voltage and pressure are defined as internal vs. external solution.

The possibility of electroosmosis (EO)-driven particle translocation due to residual negative surface charge of the nanopore after silanization is ruled out in these experiments because any EO flow would be directed from the internal capillary solution to the external solution when a positive voltage (internal vs. external) is applied.

When a negative pressure (-10 mmHg) was applied across the GNM (at ~15 s in the *i-t* trace of Figure 3.2), the frequency of resistive pulses increased to ~3.3 events/s, corresponding to convection translocation of the PS nanoparticles through the nanopore. An expanded *i-t* trace of an individual pulse is shown in the inset of Figure 3.2. The asymmetric triangular-shaped pulse reflects a convolution of the geometries of the conical-shaped pore and spherical particle, *vide infra*. We previously reported that a similar triangular-shaped pulse is also observed in the electrophoresis-driven translocation of nanoparticles through conical-shaped nanopores.[8] It is also interesting to note that the baseline current increases upon application of pressure, a consequence of the disruption of the ion distributions inside the nanopore by the flowing solution. This phenomenon will be detailed in Chapter 4 of this dissertation.

Figure 3.3 shows the *i-t* recordings of the 210 nm radius GNM in 0.1 M KCl solution in the presence of PS particles at applied pressures ranging from 0 to -90 mmHg. As the applied pressure is increased, the number of particles passing through the nanopore per unit time increases, while the resistive pulse height decreases. The increase in translocation frequency at higher pressure is due to the increase in convective flow, which carries the particles through the nanopore. The decrease in pulse height is a consequence of instrumental electrical low-pass filtering and is described later in detail.

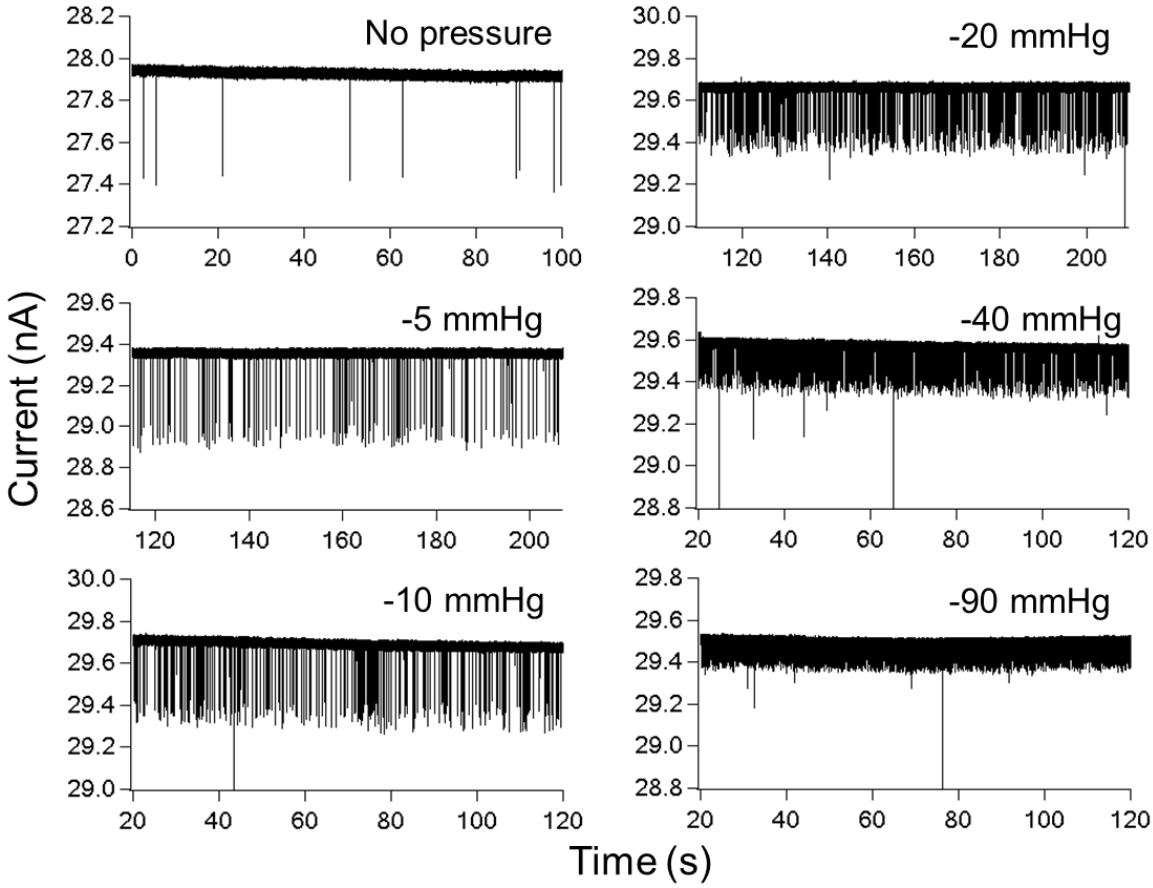

Figure 3.3. *i-t* recordings corresponding to the translocation of 120 nm radius PS particles (1.3×10^9 particles/mL, 200 mV) at different pressures (internal vs. external) using a 210 nm radius GNM in a 0.1 M KCl solution (pH 7.5).

Each current pulse in the *i-t* trace of Figure 3.3 corresponds to a single nanoparticle translocation. The few large pulses are due to coincident translocation of multiple particles, or translocation of particle agglomerates, resulting in a pulse of greater amplitude and longer duration time.[23,24] Figure 3.4 shows that a linear dependence between the translocation frequency and applied pressure is observed over an approximately two orders of magnitude range in pressure. A similar linear relationship has also been observed by Willmott et al.[21a] As shown in the following sections, the translocation frequency is dominated by convective flow through the conical-shaped nanopore.

3.3.2 Analytical expression for flow through a GNM

The translocation frequency was computed based on the pressure-driven volumetric flow rate through the pore by multiplying the computed flow rate (mL/s) by the particle concentration (particles/mL). We assumed that the particles move uniformly with the solution flow and that there are no entrance effects due to the comparable sizes of the nanoparticles (120 nm) and nanopore orifice (210 nm). Calculations of the volumetric flow rate through the GNM were based on the geometry schematically drawn in Figure 3.5 (not to scale). The GNM consists of a cylindrical capillary and a conical nanopore in series. The flow rate Q (m^3/s) is readily derived in terms of the solution viscosity, η, (see ref. 25 and the Appendix):

$$Q = \Delta P(\frac{3\pi}{8\eta})[3LR_3^{-4} + \cot\theta(R_1^{-3} - R_2^{-3})]^{-1} \qquad (3.1)$$

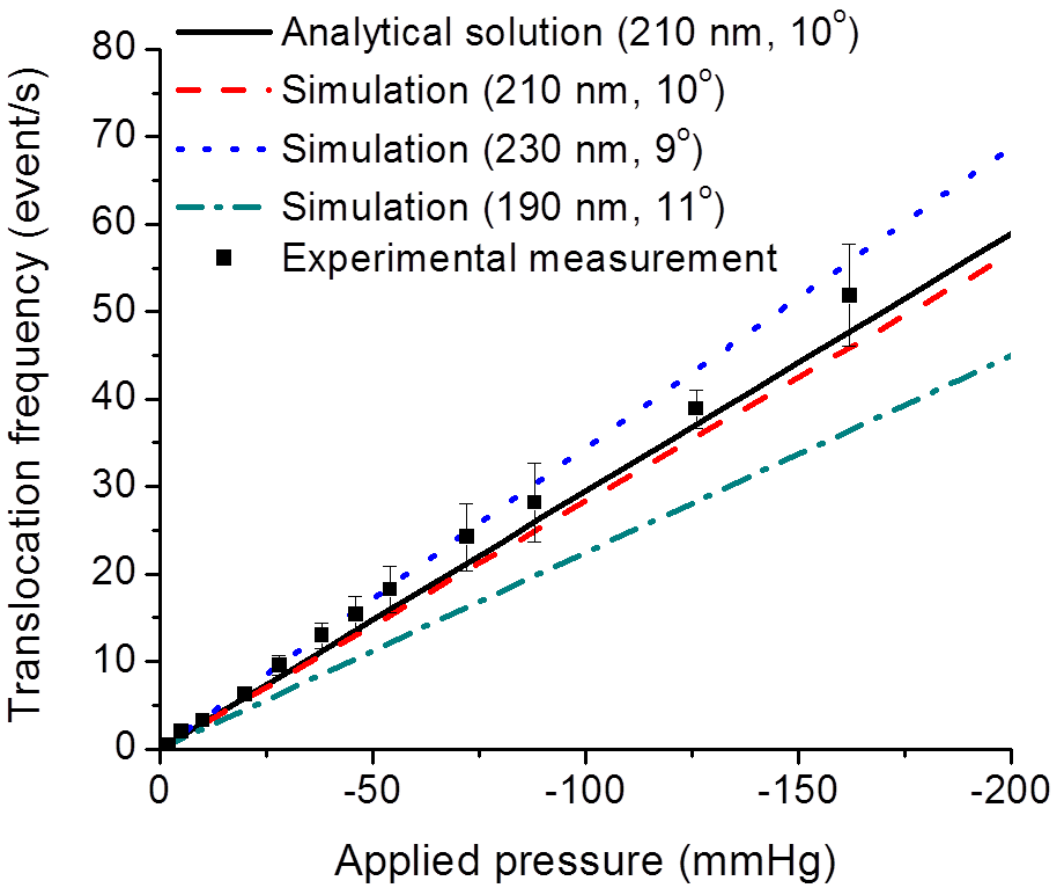

Figure 3.4. Comparison of the particle translocation frequencies as a function of pressure obtained from analytical theory, finite-element simulation, and experimental measurement. The curves correspond to 120 nm radius PS particles (1.3×10^9 particles/mL) translocating through a 210 nm radius pore in a 0.1 M KCl solution (pH 7.5) at constant voltage (200 mV). The simulated values are shown for the conical nanopore half-cone angles (θ) of 9, 10 and 11°, corresponding to the estimated experimental value of $\theta = 10 \pm 1$ °.

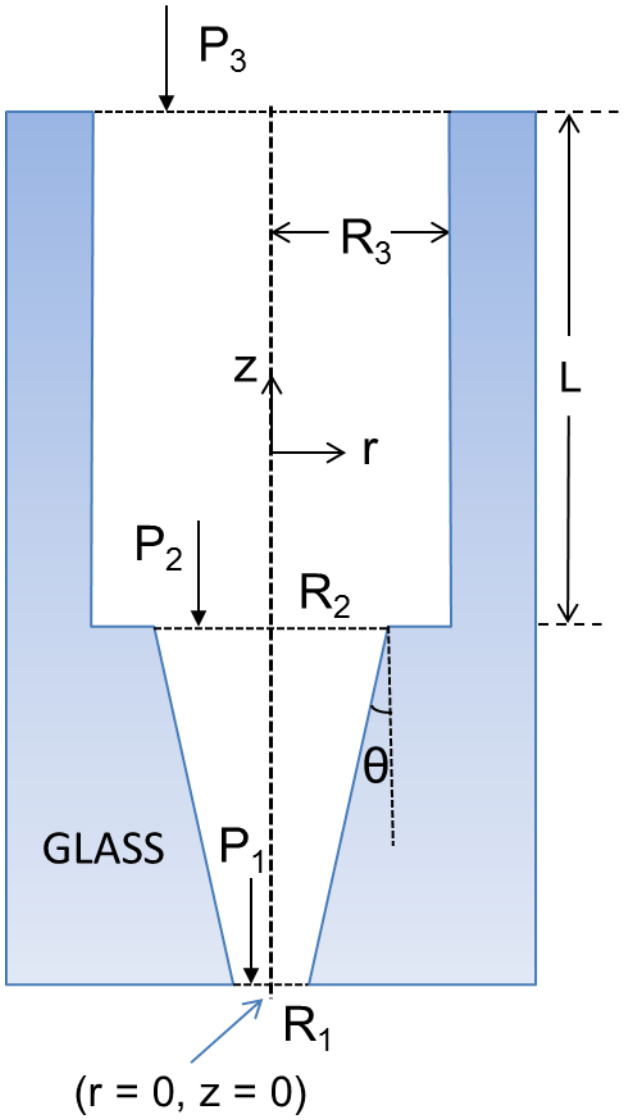

Figure 3.5. GNM geometry used to derive eq 3.1 in the text (not drawn to scale).

where $\Delta P = P_3 - P_1$, L is the height of the solution in the cylindrical capillary, R_1 and R_2 are the small and large orifice radii of the nanopore, θ is the half-cone angle of the nanopore, and R_3 is the capillary radius.

Eq 3.1 is simplified by noting that R_3 (0.375 mm) and R_2 (3.7 μm, assuming θ = 10° and the thickness of the conical pore is 20 μm) are at least 10 times larger than R_1 (210 nm) for the GNM used in these experiments. Thus, R_2^{-3} is three orders of magnitude smaller than R_1^{-3} and $3LR_3^{-4}$ (assuming L = 2 cm) is eight orders of magnitude smaller than $R_1^{-3}\cot\theta$, and eq 3.1 simplifies to eq 3.2 with negligible loss of accuracy.

$$Q = \frac{3\pi R_1^{\,3}(P_3 - P_1)}{8\eta \cot\theta} \tag{3.2}$$

Eq 3.2 indicates that the volumetric rate increases proportionally to the third power of the pore orifice radius for a conical-shaped pore, in contrast to the fourth power of the radius of a cylindrical-shaped pore (Hagen-Poiseuille eq). Thus, for the same applied pressure, the conical-shaped pore yields a larger volumetric rate than a cylindrical pore of radius R_1 and with the same length.

The average solution velocity ($u_{avg} = Q/\pi R_1^2$) at the orifice of the GNM, eq 3.3, is proportional to the applied pressure and orifice radius.

$$u_{avg} = \frac{3R_1(P_3 - P_1)}{8\eta \cot\theta} \tag{3.3}$$

As shown from computer simulations below, the solution velocity, $u(r, z)$, reaches a

maximum near the center of the pore orifice (r = 0, z = 0), falling quickly to near-zero values inside and outside of the nanopore, and along the walls of the pore.

The nanopore orifice radius R_1, the applied pressure P_3, and half-cone angle θ in eq 3.3 can be measured experimentally. However, the pressure at the pore orifice, P_1, is unknown because a fraction of the total pressure drop occurs in the bulk solution outside of the GNM. Thus, a numerical procedure was used to fully solve for the pressure and velocity distributions in order to determine the particle translocation frequency.

3.3.3 Finite-element simulations of pressure-driven particle transport

A physical description of the pressure-driven mass flow in the conical-shaped capillary starts from the Navier-Stokes equation.

$$\mathbf{u}\nabla\mathbf{u} = \frac{1}{\rho}(-\nabla P + \eta\nabla^2\mathbf{u}) \tag{3.4}$$

In eq 3.4, **u** is the r, z position-dependent fluid velocity, ρ is the density of fluid, and P is the local pressure. The simulation was simplified by three assumptions: steady-state condition, incompressible fluid flow, and no electroosmotic flow. The GNM was modeled using a 2D axial symmetric system and the model parameters were set to reflect the geometry of a conical-shaped GNM used in the experiments earlier (see Appendix for details of the model geometry, boundary conditions, and simulation meshing). The simulation contains no adjustable unknown parameters.

Figures 3.6a and 3.6c show the pressure distribution across a 210 nm radius GNM for an applied pressure of -10 mmHg (internal vs. external). All pressures are plotted

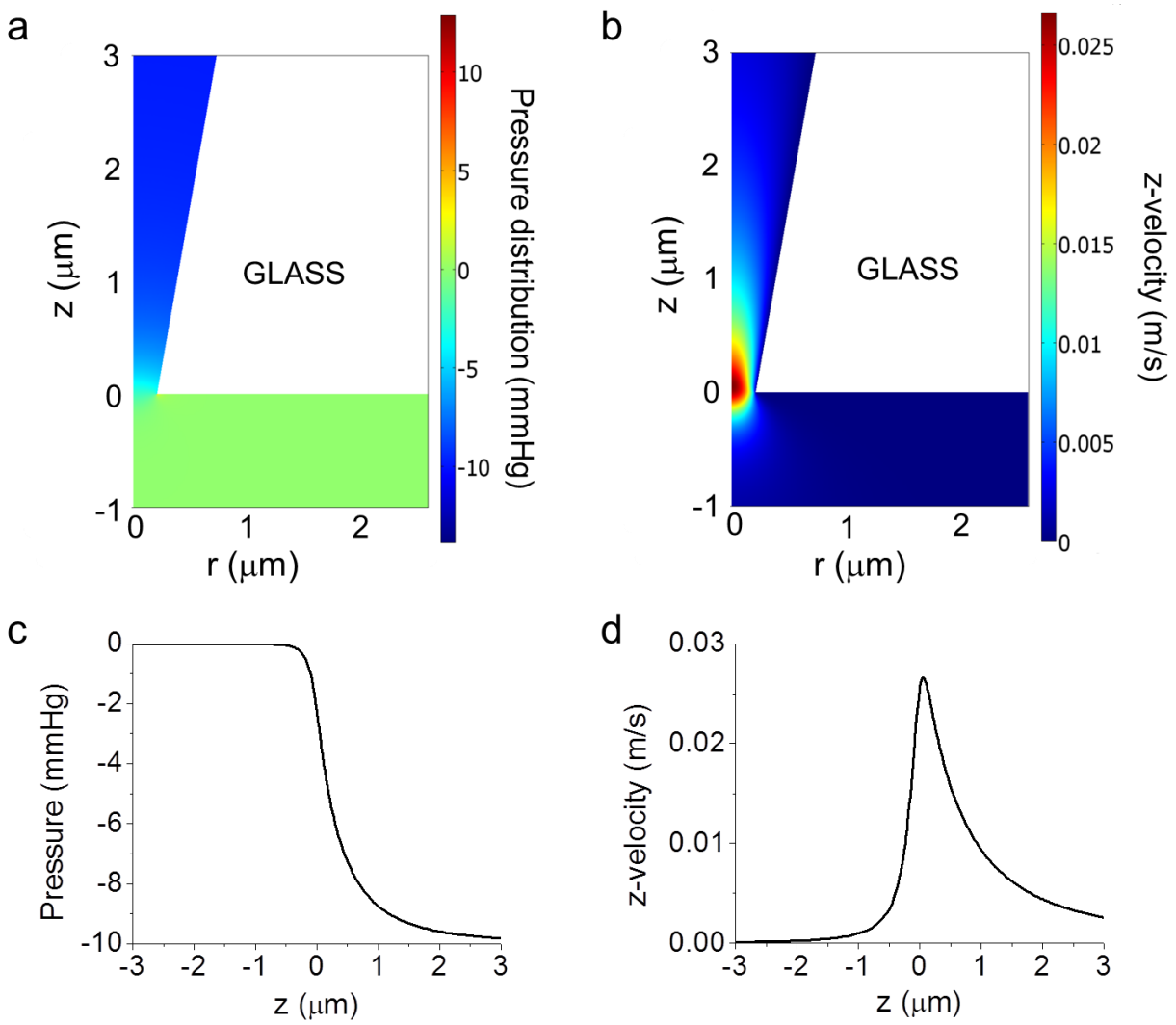

Figure 3.6. (a) Simulated pressure and (b) *z*-velocity distribution in the solution near the GNM orifice at -10 mmHg pressure. (c) Simulated pressure and (d) *z*-velocity along the central axis of the GNM opening at -10 mmHg pressure. The opening of the pore is located at $z = 0$ μm in each figure. Values of $z < 0$ μm correspond to the external solution, while values of $z > 0$ μm correspond to the nanopore interior.

relative to the bulk external solution value which is arbitrarily assigned a value of 0 mmHg. Starting from the bulk external solution, the pressure along the center axis of the nanopore begins to decrease significantly at a distance of ~0.5 μm from the orifice, decreasing to almost 23% at the orifice. The remaining 77% of the pressure drop occurs more slowly within the nanopore over a distance of ~3 μm.

Figures 3.6b and 3.6d show the fluid velocity distribution resulting from the pressure drop across the pore orifice. Again, starting in the bulk external solution, the velocity increases steeply from zero to a maximum value of ~0.027 m/s near the nanopore orifice, and then drops back slowly in the pore interior to a near-zero value. The simulation indicates the velocity of a nanoparticle will increase rapidly as it approaches the nanopore from the exterior solution, and then decreases more slowly as it enters the nanopore. A consequence of this position-dependent flow velocity is the asymmetry in the resistive pulse. Results from additional pressure-dependent simulations show that the flow rate and fluid velocity are proportional to the applied pressure (Appendix), in good agreement with the analytical expressions presented above.

The volumetric rate Q (m^3/s) was computed by integration of the simulated z-velocity distribution over the GNM orifice, allowing the nanoparticle translocation frequency to be computed (particles/s = flow rate × particle concentration in the bulk solution). In addition, the pressure P_1 at the nanopore orifice (23% of the applied pressure) is obtained from the simulation and can be employed in the analytical theory (eq 3.1, 3.2, and 3.3) to compute the translocation frequency. The values obtained are summarized in Figure 3.4 and show that the analytical theory and finite-element simulation match the experimental data quite well.

The simulated and calculated particle translocation frequencies are sensitive to the nanopore geometrical parameters R_1 and θ (eq 3.2). For instance, Figure 3.4 shows simulation values of the translocation frequency for θ = 9, 10, 11° with different pore orifice radii. Clearly, a quantitative prediction of translocation frequencies requires precise determination of the nanopore geometry. The excellent agreement between the experimental and simulated values is somewhat fortuitous because the estimated error in θ is of the order of ± 1°.

The Navier-Stokes model was also combined with the Nernst-Planck model in the simulations to quantitatively predict the nanoparticle translocation pulse height and duration.[8] The ion fluxes, potential distribution, and current are modeled by the Nernst-Planck equation, assuming electroneutrality.

$$\mathbf{J}_i = -D_i \nabla c_i - \frac{z_i F}{RT} D_i c_i \nabla \Phi \tag{3.5}$$

In eq 3.5, $\mathbf{J}_i$, D_i, c_i, and z_i are, respectively, the ion flux vector, diffusion coefficient, concentration, and charge of species i in solution. Φ is the local electric potential and F, R, and T are Faraday's constant, the gas constant, and the temperature, respectively. The geometry of the model used to compute the ion current is the same as that used in the Navier-Stokes model (Appendix). The glass surface of the nanopore was defined as an uncharged and insulating boundary. The parameters for the ionic species were chosen to reflect the 0.1 M KCl solution (D_{K+} = 1.957 × 10^{-9} m^2/s,[26] c_{K+} = 0.1 M, z_{K+} = +1, D_{Cl-} = 2.032 × 10^{-9} m^2/s,[26] c_{Cl-} = 0.1 M, z_{Cl-} = -1, T = 298 K). Note that the ion diffusion coefficients used correspond to infinite dilution conditions; actual diffusion coefficients

in 0.1 M KCl solution may be smaller.

In employing the Nernst-Planck equation to compute the current while ignoring convective transport of ions, we implicitly assume that the electrolyte ions are uniformly distributed throughout the solution at the bulk concentration (0.1 M), including within the nanopore. Thus, solution flow does not result in a flux of charge. This assumption is equivalent to assuming an ohmic *i*-*V* response and the absence of permselectivity, as ion current rectification in glass nanopores results from a non-uniform distribution of ions within the nanopore.[27] The *i*-*V* response of the silanized 210 nm radius nanopore shows a nearly ohmic response in the 0.1 M KCl solution, justifying the assumption of a uniform ion distribution.

A 120 nm radius nanoparticle was introduced into the simulation as a nonconducting sphere. The nanoparticle was moved incrementally in Δz steps (of width between 25 and 1000 nm) along the centerline axis of the pore, and the ion fluxes in the presence of the nanoparticle were computed. This manual stepping of the particle through the nanopore generates a current-position (*i*-*z*) pulse, as shown in Figure 3.7a. With the solution velocity ($u(z)$) at each position along the centerline ($r = 0$) provided by the simulations of the fluid flow, the *i*-*z* pulse was converted into a dynamic *i*-*t* pulse, as shown in Figure 3.7b, using the expression $\Delta t = \Delta z/u$. Here we assume that the particle moves at the same velocity as the solution. However, because the particle is accelerated during its entire motion through a conical nanopore, drag forces acting on it may reduce and increase its velocity relative to the solution as it enters and exits the pore, respectively. The complexity of this fluid dynamics problem is beyond the scope of this work.

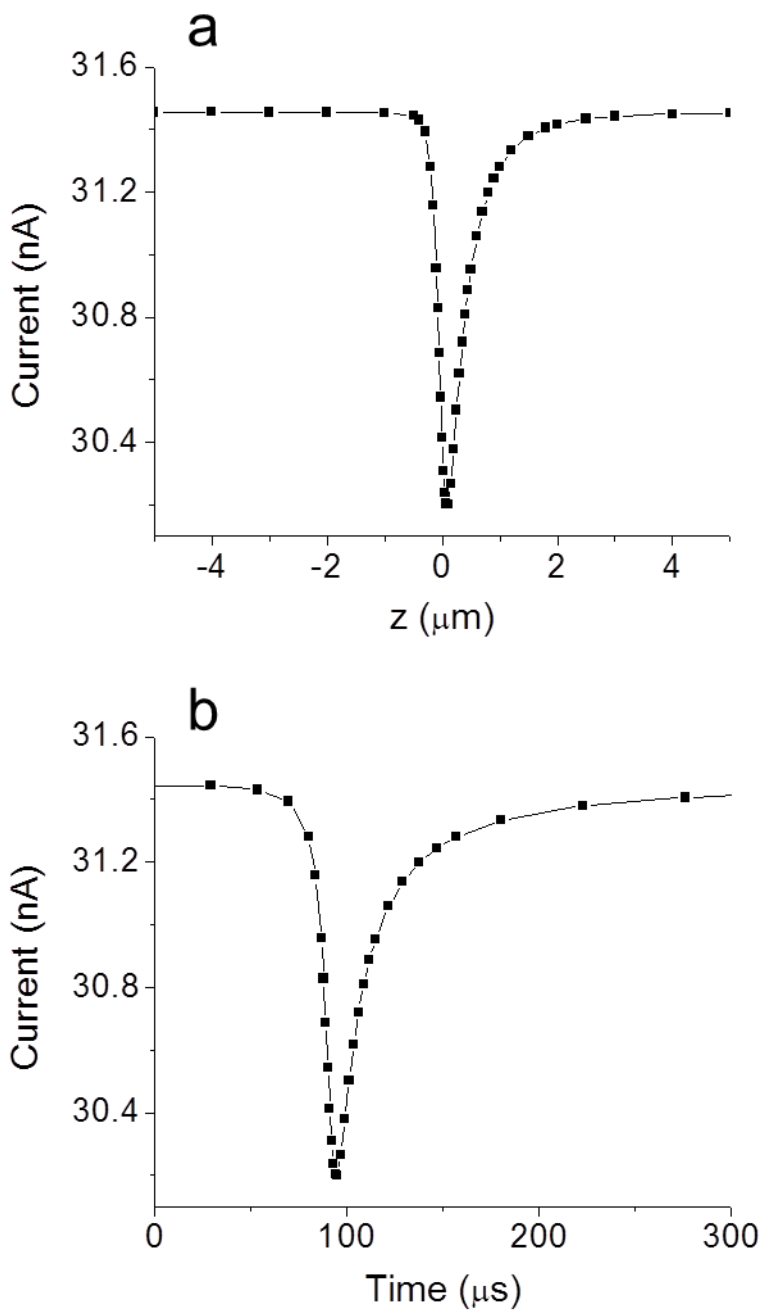

Figure 3.7. (a) Simulated *i-z* and (b) *i-t* pulses corresponding to translocation of a 120 nm radius PS nanoparticle through a 210 nm radius nanopore in a 0.1 M KCl solution at -10 mmHg pressure. The opening of the pore is located at $z = 0$ μm. Values of $z < 0$ μm correspond to the external solution, while values of $z > 0$ μm correspond to the nanopore interior. Applied voltage: 200 mV internal vs. external solution.

The full-width at half-maximum (FWHM) of the simulated translocation pulse in Figure 3.7b, obtained at a pressure of -10 mmHg, ~22 μs, is significantly shorter than the experimentally measured value, ~90 μs (average FWHM of 1292 pulses recorded at -10 mmHg). While much of this difference is due to the use of a 10 kHz low-pass filter, the simulation of the translocation pulse is also complicated by the highly confined geometry of the nanopore and the drag on the particle. Figure 3.8 schematically shows an overlay of the fluid velocity profile at -10 mmHg, *computed in the absence of a particle*, and the relative dimensions of the 210 nm radius nanopore and 120 nm radius nanoparticle. Our simulations of the translocation pulse shape, Figure 3.7, assume that the particle does not influence the velocity profile; i.e., the solution moves at the same velocity of the solution in the absence of nanoparticles. While this approximation appears reasonable for a dilute solution of nanoparticles moving through a bulk solution, it may be less appropriate when the particle and nanopore are of comparable dimensions, such as in our experiments. For instance, as shown in Figure 3.8, for a particle moving along the centerline axis of the nanopore, the solution velocity decreases from 0.025 m/s to 0.020 m/s over a distance comparable to the particle radius. Thus, using the centerline velocity from the simulations presumably overestimates the velocity of the nanoparticle by ~25%. A more complete and accurate simulation of this problem would involve a simultaneous solution of both the nanoparticle's motion and fluid flow through the nanopore. These calculations are currently under investigation in our laboratory.

Figures 3.9a and 3.9b show the dependence of the pulse duration time (τ, equivalent to FWHM) determined from the finite-element simulations on the applied pressure and the relative sizes of the nanopore (R_1) and nanoparticle (R_p). Since the fluid

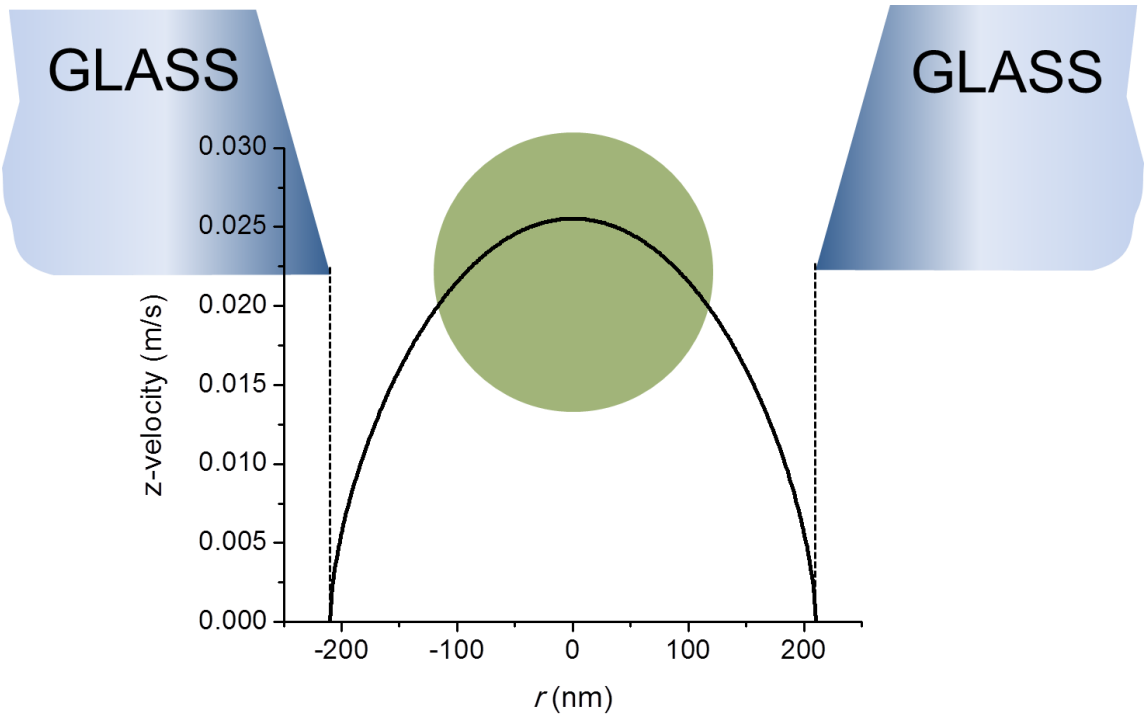

Figure 3.8. Simulated *z*-velocity along the *r* direction at the 210 nm radius GNM opening (z = 0) at -10 mmHg pressure, computed in the absence of a particle. A 120 nm radius particle is drawn (centered at the nanopore orifice, r = 0, z = 0) to qualitatively depict the relative sizes of the velocity gradient, particle and nanopore.

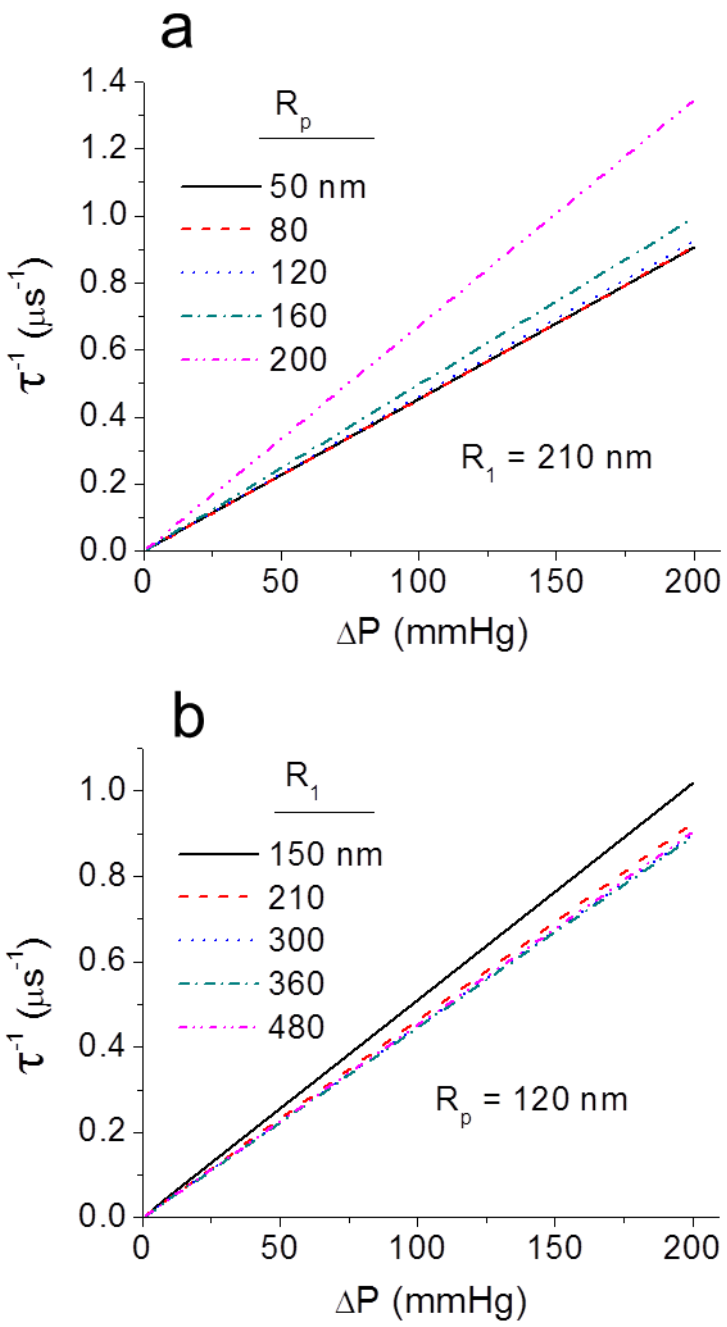

Figure 3.9. (a) The reciprocal of the simulated duration time, τ^{-1}, as a function of ΔP and R_p for R_1 = 210 nm. (b) Values of τ^{-1} as a function of ΔP and R_1 for R_p = 120 nm.

velocity is proportional to the applied pressure, eq 3.3, τ is inversely proportional to the pressure, and thus, all plots of τ^{-1} vs. ΔP in Figure 3.9 are linear. As discussed above, the values of τ are based on the assumption that the nanoparticles move at the same velocity of the solution along the centerline of the nanopore. Figures 3.9a and 3.9b show that values of τ are independent of relative values of R_p and R_1 for $R_p/R_1 < 0.5$, but decrease significantly as the nanoparticle radius becomes comparable to the pore radius ($R_p/R_1 > 0.5$). This dependence reflects the convolution of the width and magnitude of the pressure gradient across the nanopore orifice (which determines the driving force on the particle and its velocity) and the volume of electrolyte solution excluded by the particle as it passes across the pressure gradient (which determines the change in electrical current). Larger particles passing through a pore of constant size, Figure 3.9a, exclude a larger volume of solution, generating a sharper resistive pulse, and smaller τ values. Figure 3.9b shows that for a fixed particle size, values of τ are nearly independent of the nanopore radius. This is counter-intuitive, since the solution velocity through the nanopore increases in proportion to R_1, eq 3.3. However, the increase in velocity is countered by the fact that the width of the sensing zone of a conical nanopore is also proportional to R_1. Thus, these two offsetting factors result in pulse widths that are nearly independent of the nanopore radius.

3.4 Conclusions

Experiments, theory, and finite-element simulations of pressure-driven translocation of nanoparticles across a conical-shaped nanopore demonstrate a linear dependence of translocation frequency that can be readily computed, *a priori*, from the applied transmembrane pressure, radius of the small opening of the nanopore, and solution viscosity. Although not detailed in this chapter, the translocation frequency is also proportional to the nanoparticle concentration. These findings, coupled with the ease of preparing conical pores in glass with readily measured orifice radii, suggest that GNMs are suitable for quantitative analytical measurements of particle concentrations. The agreement between observed and predicted translocation event frequencies suggests that the rate of entry of 120 nm radius nanoparticles into a 210 nm radius orifice is not strongly influenced by any finite-size kinetic limitations; i.e., the rate of translocation is controlled largely by volumetric flow and effects associated with the entry of particles into the nanopore, of comparable dimensions, do not greatly impede translocation rates. Small uncertainties in pore geometry, however, may conceal entry kinetic effects. The findings and conclusions reported in this chapter are based on experiments using nanopores in glass of radius greater than 100 nm. More complex flow behaviors in much smaller pores (< 5 nm) and in pores fabricated in other materials, may arise from chemical interactions between the solution and the pore surface.

Our studies reveal that there are several significant challenges in applying GNMs (and conical-shaped pores, in general) to the determination of particle shape and size via pressure-driven transport. Foremost, the velocity of solution flow through a conical-shaped nanopore, even at modest pressure, is very large, and is coupled to the narrow

sensing zone of a conical pore. This results in very short pulse widths that are obscured by low-pass filtering from both the electronic instrumentation and capacitances associated with the electrolyte cell components. For instance, at -200 mmHg, the pulse width is predicted to be on the order of ~1 μs, which will require MHz bandwidths to accurately measure the pulse magnitude, when measurement of the particle size is the experimental objective. This limitation can be potentially overcome by using faster electronics and by improvements in the cell design and selection of materials used to construct the nanopores. Second, unlike flow in a cylindrical nanopore where the flow velocity increases with the square of the pore radius (r^2), the flow velocity across a conical nanopore is proportional to the pore radius (r). This finding, coupled with the same dependence of the sensing zone width on the orifice radius, results in pulse widths that are nearly independent of the radius of the nanopore. In contrast, the translocation pulse width in a cylindrical pore or channel can be tuned by varying the length of the pore or channel.

3.5 Appendix

3.5.1 Derivation of Eq 3.1

The derivation of flow through a GNM is summarized as follows. The volumetric flow rate (Q) due to a pressure difference (ΔP) applied across a cylindrical capillary of length, L, and radius, r_c, is given by the Hagen-Poiseuille equation,

$$Q = \frac{\pi r_c^{\,4} \Delta P}{8 L \eta}$$

where η is the solution viscosity. Rearranging, and using the definitions of the geometric parameters defined in Figure 3.5 of the main text,

$$P_3 - P_2 = \frac{8L\eta Q}{\pi R_3^{\,4}} . \tag{3.6}$$

For flow in a conical-shaped pore, the relationship between the differential pressure and the length of pore is given by

$$dp = \frac{8\eta Q}{\pi r^4} dl \tag{3.7}$$

where

$$dl = dr \cot\theta . \tag{3.8}$$

Substituting Eq 3.8 into 3.7 yields

$$dp = \frac{8\eta Q \cot\theta}{\pi r^4} dr . \tag{3.9}$$

The pressure drop (from P_2 to P_1) over the conical pore (between R_2 and R_1, see Figure 3.5 of main text) is given by

$$P_2 - P_1 = \frac{8\eta Q \cot\theta}{\pi}\int_{R_1}^{R_2} r^{-4} dr \quad . \tag{3.10}$$

Integration yields

$$P_2 - P_1 = -\frac{8\eta Q \cot\theta}{3\pi}(R_2^{-3} - R_1^{-3}) \quad . \tag{3.11}$$

An equivalent form of eq 3.11 was reported by Nguyen et al. in their studies of vascular flow. (Nguyen, B. P.; Chui, C. K.; Ong, S. H.; Chang, S., "Vascular Flow Rendering for Interactive Simulation of Contrast and Drugs Injection", *IEEE Region 10 Annual International Conference, Proceedings/TENCON*, 2009, art. no. 5395825.)

Combining 3.6 + 3.11 to eliminate the pressure P_2 at the large opening at the base of the conical pore yields eq 3.1 in the main text.

$$P_3 - P_1 = \frac{8\eta Q}{3\pi}[3LR_3^{-4} + \cot\theta(R_1^{-3} - R_2^{-3})] \tag{3.12}$$

where

$$P_3 = P_0 + P_a \quad . \tag{3.13}$$

P_0 is atmospheric pressure and P_a is the applied pressure, respectively, and the geometrical parameters θ, L, R_1, R_2, and R_3 are defined in Figure 3.5 of the main text.

3.5.2 Geometry, mesh, and boundary conditions used in simulations

COMSOL Multiphysics software (version 3.5a) was used with the stationary incompressible Navier Stokes module to compute the pressure and the velocity profile across the GNM. The geometry of the model, a typical mesh used in the simulation, and the boundary conditions are shown in Figure 3.10. The orifice radius and length of the conical pore were set equal to 210 nm and 20 μm, respectively. The GNM has a typical length between 20 and 100 μm; however, because of the conical pore geometry, the majority of the pressure drops occurs near the small orifice opening (see Figure 3.6c of the main text). Thus, in the limit that the pore length is greater than ~20 times the pore orifice radius, the precise length of the GNM used in the simulation does not significantly influence the calculated volumetric rate (consistent with eq 3.2 in the main text). For a 210 nm radius (R_1) orifice, the nanopore is required to be only ~4 μm to meet this condition. To approximate the semi-infinite boundary of the experimental cell, the exterior boundary of the bulk solution in the simulation model was extended to a radial distance of 100 μm and a vertical distance of 60 μm from the GNM orifice, Figure 3.10. The fluid density (ρ = 10^3 kg·m^{-3}) and viscosity (η = 8.9 × 10^{-4} Pa·s) corresponding to aqueous solutions were used in the subdomain settings. The mesh size at the conical orifice was refined to obtain a more accurate volumetric flow rate. An adaptive mesh refinement was used to optimize the mesh size geometry.

3.5.3 Simulated solution velocity profiles across the nanopore membrane

Figure 3.11 shows simulated solution velocities along the central axis of the 210 nm radius GNM opening at different applied pressures. The results indicate that the flow rate and fluid velocity are proportional to the applied pressure across the nanopore.

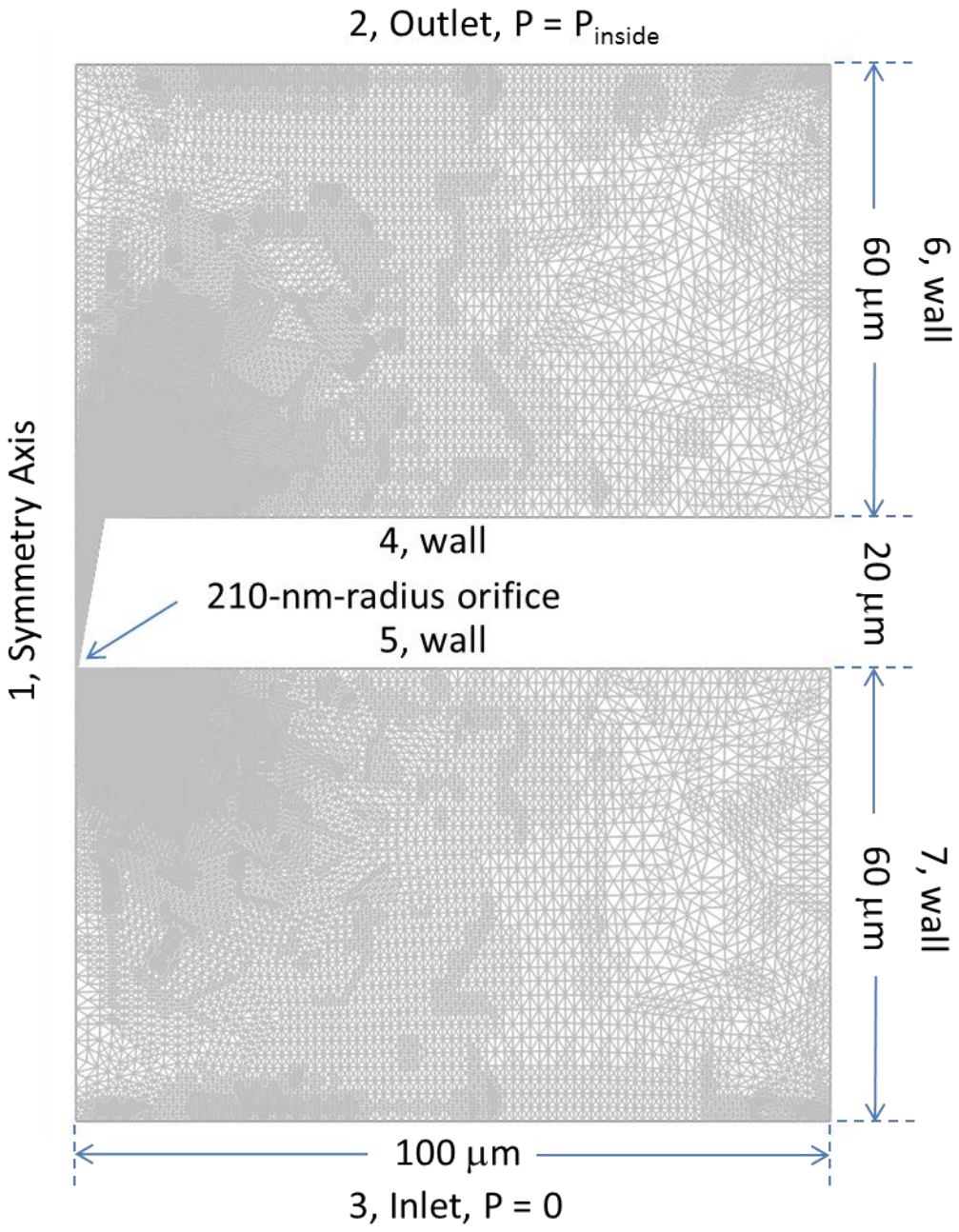

Figure 3.10. The 2D axial symmetric geometry of the GNM, the boundary settings, and a typical mesh for the finite-element simulation.

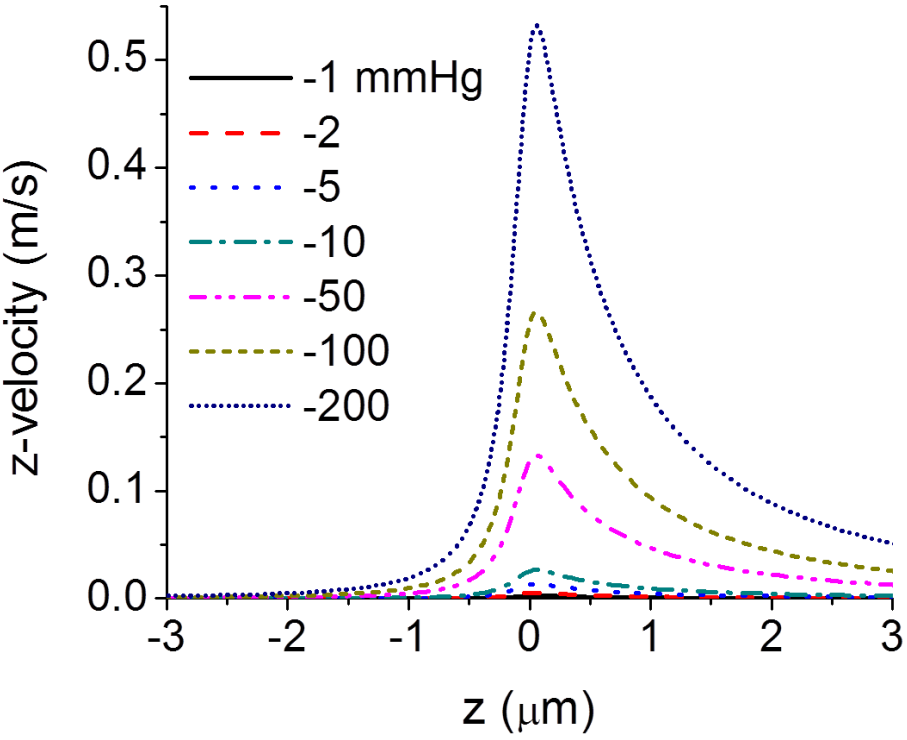

Figure 3.11. Simulated solution velocities along the central axis of the 210 nm radius GNM opening at different applied pressures. The opening of the pore is located at $z = 0$ μm. Values of $z < 0$ μm correspond to the external solution, while values of $z > 0$ μm correspond to the nanopore interior.

3.5.4 Dependence of nanoparticle translocation time and resistive pulse height on the applied pressure

The average time of translocation of a 120 nm radius particle through a 210 nm radius GNM as a function of pressure (Figure 3.12) was determined by fitting a Gaussian curve to histograms of individual translocation times (τ, half-height pulse width, Figure 3.13). The error bar represents one sigma (σ) in the Gaussian fit. The average percentage decrease in current ($\%\Delta i$) was calculated by averaging individual pulse heights and the error bar represents the standard deviation. The average duration time in the conical shaped pore was ~550 μs when no pressure was applied across the GNM, corresponding to residual particle translocation due to diffusion and electrophoresis. As the pressure is increased from 0 to -160 mmHg, the duration time decreased sharply, approaching an asymptotic value of ~50 μs. A similar dependence of $\%\Delta i$ on pressure is also observed, Figure 3.12. The finite-element simulations predict that τ is inversely proportional to the applied pressure and that $\%\Delta i$ should be independent of pressure. The discrepancies between the experiment and the simulated data are partly due to instrumental electrical filtering; data were obtained at a bandwidth of 10 kHz, limiting useful quantitative comparisons of experimental and simulated data to pulse widths greater than ~100 μs (see below).

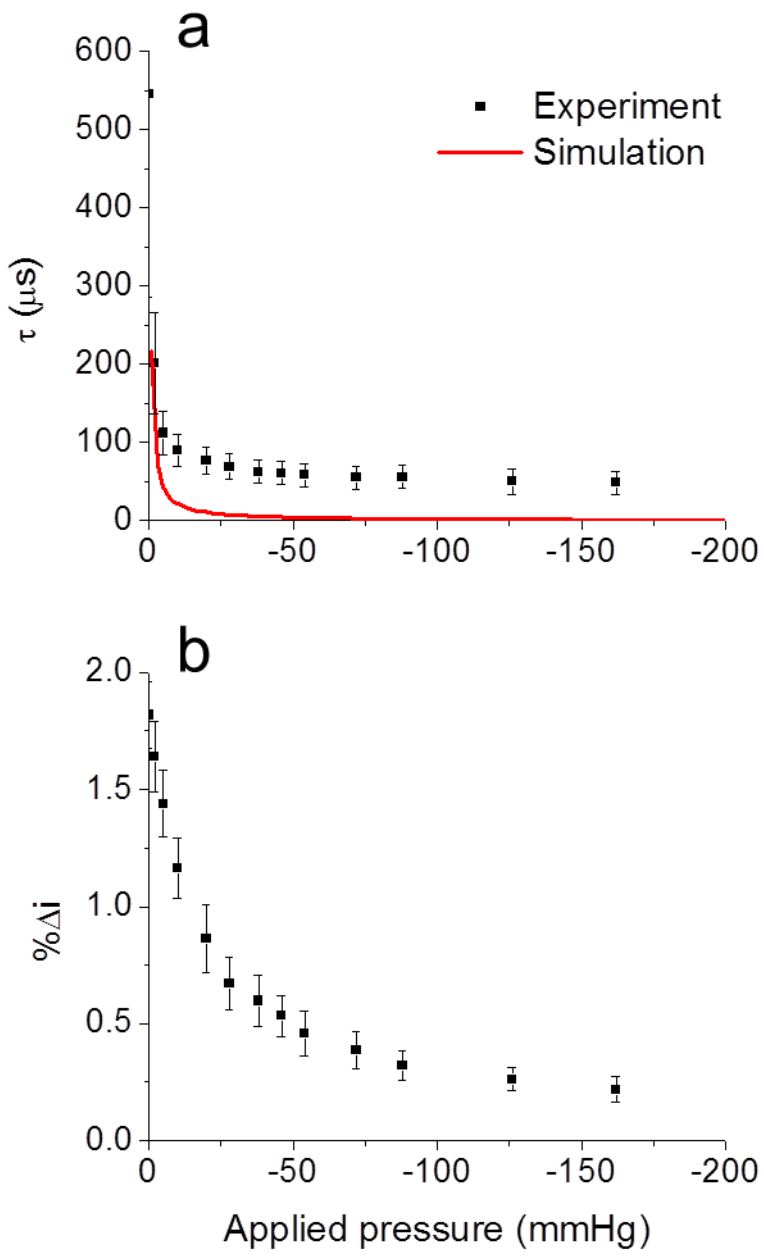

Figure 3.12. (a) Experimental and simulated duration time (τ) and (b) percentage current decrease (%Δi) as a function of applied pressure for a 210 nm radius GNM in a 0.1 M KCl buffered solution containing 0.1% Triton X-100 in the presence of 120 nm radius PS particles (1.3×10^9 particles/mL). Applied voltage: 200 mV internal vs. external.

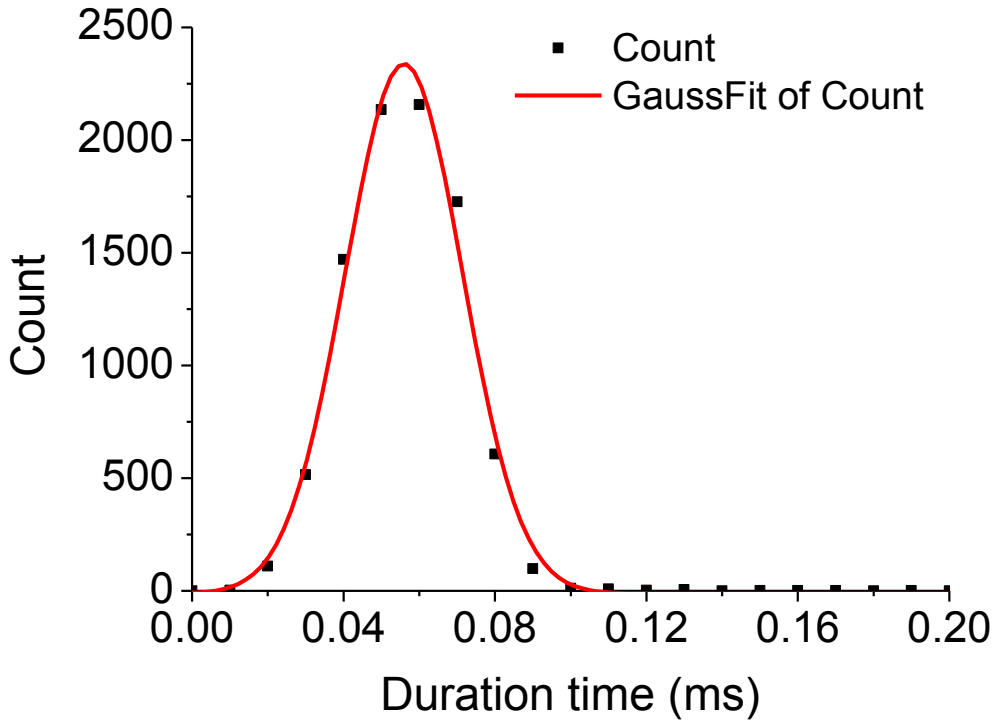

Figure 3.13. Distribution of duration times for a 120 nm radius particle translocation in a 210 nm radius GNM at an applied pressure of -90 mmHg. The red line is drawn to fit the data assuming a Gaussian distribution. Applied voltage: 200 mV internal vs. external.

3.5.5 Filtering effect in pressure-driven nanoparticle analysis

In the experiments described in the main text, a 3-pole Bessel low-pass filter was applied with a cut-off frequency of 10 kHz. The low-pass filter significantly distorted translocation pulses with duration times shorter than 100 μs. However, despite this limitation in analyzing pulse shapes, it was still possible to observe and accurately count individual pulses as short as 10 μs. For example, Figure 3.14 shows the response function of the Dagan potentiostat to square-wave pulses of width ranging from 10 to 300 μs (from a waveform generator) at a sample frequency of 75 kHz using 20 kHz low-pass filter. The data in Figure 3.14 were obtained by applying voltage pulses into the Dagan potentiostat and recording the current measured across a 100 MΩ resistor. The resulting current pulses are ~1 nA, corresponding closely to the experimental pulse heights recorded during the translocation of particles (see, for example, Figures 3.2 and 3.3 of the main text). While the response functions were greatly distorted for pulse widths less than 50 μs, it is still possible to detect individual events as low as 10 μs.

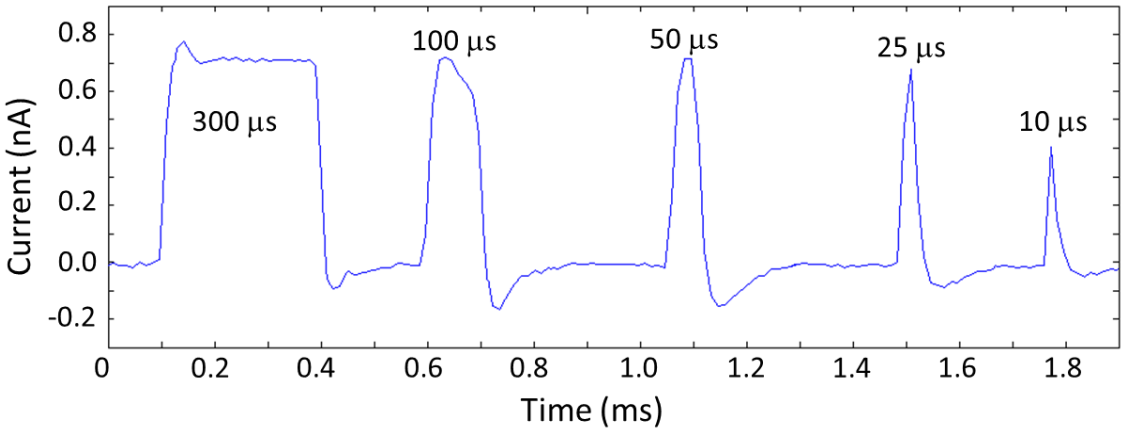

Figure 3.14. Response functions to square-wave voltage pulses, input from a waveform generator, of different widths (shown on the figure) using a ~20 kHz filter. The data acquisition rate was 75 kHz.

3.6 References

(1) Lan, W. J.; Holden, D. A.; Liu, J.; White, H. S. *J. Phys. Chem. C* **2011**, *115*, 18445-18452.

(2) Coulter, W. H. Means for Counting Particles Suspended in a Fluid. U.S. Patent 2,656,508, 1953.

(3) (a) DeBlois, R. W.; Bean, C. P. *Rev. Sci. Instrum.* **1970**, *41*, 909-916. (b) DeBlois, R. W.; Wesley, R. K. A. *J. Virol.* **1977**, *23*, 227-233.

(4) (a) Sun, L.; Crooks, R. M. *J. Am. Chem. Soc.* **2000**, *122*, 12340-12345. (b) Ito, T.; Sun, L.; Crooks, R. M. *Anal. Chem.* **2003**, *75*, 2399-2406. (c) Ito, T.; Sun, L.; Bevan, M. A.; Crooks, R. M. *Langmuir* **2004**, *20*, 6940-6945. (d) Ito, T.; Sun, L.; Crooks, R. M. *Chem. Comm.* **2003**, 1482-1483. (e) Henriquez, R. R.; Ito, T.; Sun, L.; Crooks, R. M. *Analyst* **2004**, *129*, 478-482. (f) Ito, T.; Sun, L.; Henriquez, R. R.; Crooks, R. M. *Acc. Chem. Res.* **2004**, *37*, 937-945. (g) *International Standard*, ISO 13319:2007(E), ISO, Geneva, 2007.

(5) Gu, L. Q.; Cheley, S.; Bayley, H. *Proc. Natl. Acad. Sci. U.S.A.* **2003**, *100*, 15498-15503.

(6) Wanunu, M.; Morrison, W.; Rabin, Y.; Grosberg, A. Y.; Meller, A. *Nature Nanotech.* **2010**, *5*, 160-165.

(7) (a) Bayley, H.; Martin, C. R. *Chem. Rev.* **2000**, *100*, 2575-2594. (b) Kasianowicz, J. J.; Brandin, E.; Branton, D.; Deamer, D. W. *Proc. Natl. Acad. Sci. U.S.A.* **1996**, *93*, 13770-13773. (c) Gu, L. Q.; Braha, O.; Conlan, S.; Cheley, S.; Bayley, H. *Nature* **1999**, *398*, 686-690.

(8) Lan, W. J.; Holden, D. A.; Zhang, B.; White, H. S. *Anal. Chem.* **2011**, *83*, 3840-3847.

(9) Lee, S.; Zhang, Y.; Harrell, C. C.; Martin, C. R.; White, H. S. *Anal. Chem.* **2004**, *76*, 6108-6115.

(10) Zhang, B.; Galusha, J.; Shiozama, P. G.; Wang, G.; Bergren, A. J.; Jones, R. M.; White, R. J.; Ervin, E. N.; Cauley, C. C.; White, H. S. *Anal. Chem.* **2007**, *79*, 4778-4787.

(11) White, R. J.; Zhang, B.; Daniel, S.; Tang, J. M.; Ervin, E. N.; Cremer, P. S.; White, H. S. *Langmuir* **2006**, *22*, 10777-10783.

(12) (a) Zhang, B.; Zhang, Y.; White, H. S. *Anal. Chem.* **2006**, *78*, 477-483. (b) Zhang, Y.; Zhang, B.; White, H. S. *J. Phys. Chem. B* **2006**, *110*, 1768-1774.

(13) (a) Siwy, Z.; Fulinski, A. *Phys. Rev. Lett.* **2002**, *89*, 198103. (b) Siwy, Z., Gu, Y.; Spohr, H. A.; Baur, D.; Wolf-Reber, A.; Spohr, R.; Apel, P.; Korchev, Y. E. *Europhys*. *Lett.* **2002**, *60*, 349-355. (c) Siwy, Z.; Heins, E.; Harrell, C. C.; Kohli, P.; Martin, C. R. *J. Am. Chem. Soc.* **2004**, *126*, 10850-10851. (d) Siwy, Z.; Kosinska, I. D.; Fulinski, A.; Martin, C. R. *Phys. Rev. Lett.* **2005**, *94*, 048102. (e) Siwy, Z. S.; Powell, M. R.; Kalman, E.; Astumian, R. D.; Eisenberg, R. S. *Nano Lett.* **2006**, *6*, 473-477.

(14) (a) Choi, Y.; Baker, L. A.; Hillebrenner, H.; Martin, C. R. *Phys. Chem. Chem. Phys.* **2006**, *8*, 4976-4988. (b) Siwy, Z. S.; Trofin, L.; Kohli, P.; Baker, L. A.; Trautmann, C.; Martin, C. R. *J. Am. Chem. Soc.* **2005**, *127*, 5000-5001. (c) Harrell, C. C.; Choi, Y.; Horne, L. P.; Baker, L. A.; Siwy, Z. S.; Martin, C. R. *Langmuir* **2006**, *22*, 10837-10843. (d) Heins, E. A.; Siwy, Z. S.; Baker, L. A.; Martin, C. R. *Nano Lett.* **2005**, *5*, 1824-1829. (e) Sexton, L. T.; Horne, L. P.; Sherrill, S. A.; Bishop, G. W.; Baker, L. A.; Martin, C. R. *J. Am. Chem. Soc.* **2007**, *129*, 13144-13152. (f) Sexton, L. T.; Mukaibo, H.; Katira, P.; Hess, H.; Sherrill, S. A. Horne, L. P.; Martin, C. R. *J. Am. Chem. Soc.* **2010**, *132*, 6755-6763.

(15) Zhou, K.; Li, L.; Tan, Z.; Zlotnick, A.; Jacobson, S. C. *J. Am. Chem. Soc.* **2011**, *133*, 1618-1621.

(16) (a) Saleh, O. A.; Sohn, L. L. *Rev. Sci. Instrum.* **2001**, *72*, 4449-4451. (b) Saleh, O. A.; Sohn, L. L. *Proc. Natl. Acad. Sci. U.S.A.* **2003**, *100*, 820-824.

(17) Petrossian, L; Wilk, S. J.; Joshi, P.; Goodnick, S. M.; Thornton, T. J. *J. Phys.: Conf. Ser.* **2008**, *109*, 012028.

(18) (a) Zhang, B.; Wood, M.; Lee, H. *Anal. Chem.* **2009**, *81*, 5541-5548. (b) Bacri, L.; Oukhaled, A. G.; Schiedt, B.; Patriarche, G.; Bourhis, E.; Gierak, J.; Pelta, J.; Auvray, L. *J. Phys. Chem. B* **2011**, *115*, 2890-2898.

(19) White, R. J.; White, H. S. *Anal. Chem.* **2007**, *79*, 6334-6340.

(20) (a) Steinbock, L. J.; Stober, G.; Keyser, U. F. *Biosens. Bioelectron.* **2009**, *24*, 2423-2427. (b) Zhe, J.; Jagtiani, A.; Dutta, P.; Hu, J.; Carletta, J. *J. Micromech. Microeng.* **2007**, *17*, 304-313. (c) Jagtiani, A. V.; Zhe, J.; Hu, J.; Carletta, J. *Meas. Sci. Technol.* **2006**, *17*, 1706-1714. (d) Scott, R.; Sethu, P.; Harnett, C. K. *Rev. Sci. Instrum.* **2008**, *79*, 046104.

(21) (a) Willmott, G. R.; Vogel, R.; Yu, S. S. C.; Groenewegen, L. G.; Roberts, G. S.; Kozak, D.; Anderson, W.; Trau, M. *J. Phys.: Condens. Matter* **2010**, *22*, 454116. (b) Roberts, G. S.; Kozak, D.; Anderson, W.; Broom, M. F.; Vogel, R.; Trau, M. *Small* **2010**, *6*, 2653-2658. (c) Vogel, R.; Willmott, G.; Kozak, D.; Roberts, G. S.; Anderson, W.; Groenewegen, L.; Glossop, B.; Barnett, A.; Turner, A.; Trau, M.

Anal. Chem. **2011**, *83*, 3499-3506. (d) Willmott, G. R.; Parry, B. E. T. *J. Appl. Phys.* **2011**, *109*, 094307.

(22) Technotes 100 and 201, Bangs Laboratories Inc., Fishers, IN (www.bangslabs.com).

(23) Higgins, A. Z.; Karlsson, J. O. M. *CryoLetters* **2008**, *29*, 447-461.

(24) Figueiredo, M. M. In *Encyclopedia of Analytical Chemistry*; Meyers, R. A., Ed.; John Wiley & Sons: New York, 2000; pp 5358-5371.

(25) (a) Nguyen, B. P.; Chui, C. K.; Ong, S. H.; Chang, S. *IEEE Region 10 Annual International Conference, Proceedings/TENCON*, Singapore, 2009; art. no. 5395825. (b) Kemblowski, Z.; Kiljanski, T. *Chem. Eng. J.* **1975**, *9*, 141-151.

(26) *CRC Handbook of Chemistry and Physics*, 90th ed.; Lide, D. R., Ed.; CRC Press/Taylor and Francis: Boca Raton, FL, 2010.

(27) (a) Wei, C.; Bard, A. J.; Feldberg, S. W. *Anal. Chem.* **1997**, *69*, 4627-4633. (b) White, H. S.; Bund, A. *Langmuir* **2008**, *24*, 2212-2218. (c) Siwy, Z. S. *Adv. Funct. Mater.* **2006**, *16*, 735-746. (d) Guerrette, J. P.; Zhang, B. *J. Am. Chem. Soc.* **2010**, *132*, 17088-17091. (e) Cervera J.; Schiedt, B.; Neumann, R.; Mafe, S.; Ramirez, P. *J. Chem. Phys.* **2006**, *124*, 104706. (f) Cervera, J.; Schiedt, B.; Ramirez, P. *Europhys. Lett*. **2005**, *71*, 35-41.

CHAPTER 4

PRESSURE-DEPENDENT ION CURRENT RECTIFICATION IN CONICAL-SHAPED GLASS NANOPORES

4.1 Introduction

In this chapter, ion current rectification that occurs in conical-shaped glass nanopores in low ionic strength solutions is shown to be dependent on the rate of pressure-driven electrolyte flow through the nanopore, decreasing with increasing flow rate.[1] The dependence of the *i*-*V* response on pressure is due to the disruption of cation and anion distributions at equilibrium within the nanopore. Because the flow rate is proportional to the third power of the nanopore orifice radius, the pressure-driven flow can eliminate rectification in nanopores with radii of ~200 nm but has a negligible influence on rectification in a smaller nanopore with a radius of ~30 nm. The experimental results are in qualitative agreement with predictions based on finite-element simulations used to simultaneously solve the Nernst-Planck, Poisson, and Navier-Stokes equations for ion fluxes in a moving electrolyte within a conical nanopore.

Mass transfer through charged nanopores and nanochannels with asymmetric geometries has attracted significant attention during the past decade.[2-4] An interesting characteristic associated with charged conical-shaped nanopores is ion current rectification (ICR). ICR is defined as the asymmetric *i*-*V* response of the nanopores, i.e., the experimental departure from ohmic behavior.[5, 6] For negatively charged glass

nanopores, the magnitude of the current through the nanopore at a negative potential (pore interior vs external solution) is larger than the current at a positive potential with the same magnitude. ICR was first reported by Wei, Bard, and Feldberg in 1997 based on *i-V* experiments using quartz nanopipets.[2] It was discovered that the ICR behavior in the conical-shaped nanopipets was strongly related to the ionic strength in the cell and the nanopipet orifice size. Since then, ICR has been attracting great attention. Scientists have investigated the control of the ICR with different types of ions or surface modifications, as well as the sensing applications of the ICR phenomena.[7-9] ICR in a conical-shaped charged nanopore may arise from surface charges on the pore wall and the voltage-dependent depletion and accumulation of electrolyte ions near the nanopore orifice.[10]

We have been interested in the fabrication and analytical applications of glass and fused quartz nanopore membranes[11] (GNMs and QNMs, respectively) as nano-Coulter counters of particles and as lipid bilayer supports for ion channel recordings.[12] These conical-shaped nanopores can be prepared with orifice radii as small as a few nanometers, and they exhibit ICR behavior that is dependent on the ion concentration and nanopore radius.[13] Here we describe the dependence of the ICR behavior of conical-shaped GNMs on the pressure applied across the nanopore, as depicted in Scheme 4.1. We demonstrate that pressure-driven flow through the nanopore results in a decrease in ICR due to disruption of the equilibrium cation and anion distributions. The pressure-dependent ICR response is shown to be strongly dependent on the pore orifice size, in agreement with finite-element simulations presented below.

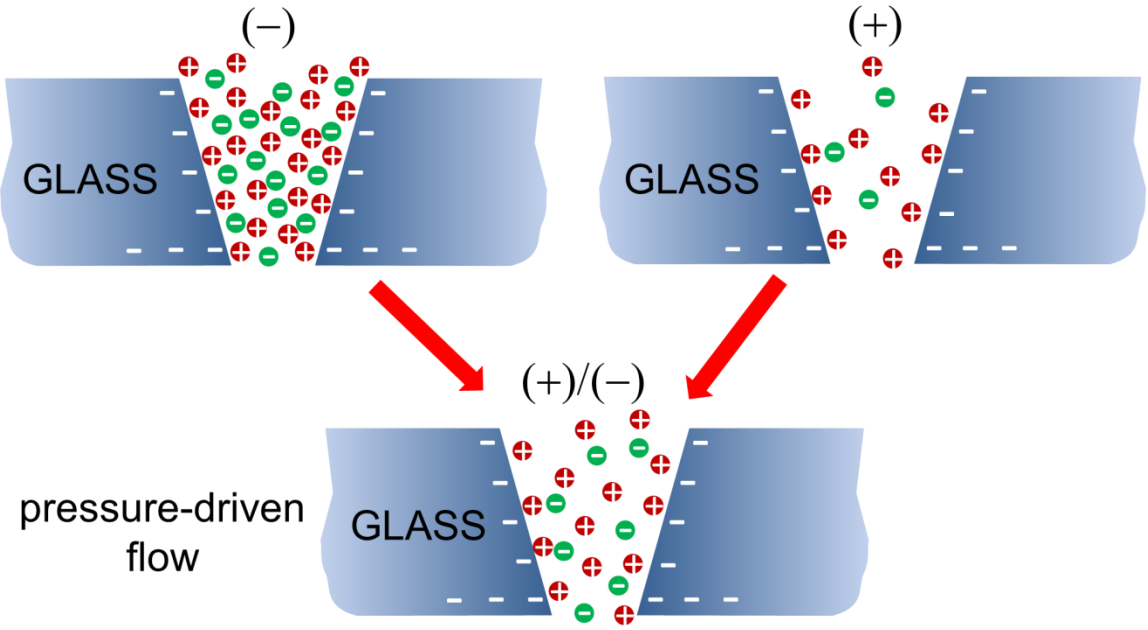

Scheme 4.1. Ion distributions around the orifice of the negatively charged GNM at positive/negative potentials in the absence and presence of pressure-driven flow. If the flow is sufficiently large, the concentrations of both cations and anions in the nanopore are equal to the values in the bulk solution in contact with the nanopore. The + and - signs refer to the polarity of the voltage applied across the membrane.

4.2 Experimental section

4.2.1 Chemicals

KCl, K_2HPO_4, and KH_2PO_4 (Mallinckrodt) were used as received. All aqueous solutions were prepared using water (18 MΩ·cm) from a Barnstead E-pure water purification system.

4.2.2 GNMs fabrication

GNMs were fabricated according to a previous report.[11] Very briefly, the preparation involves the following four steps: (1) a 2 cm length piece of 25 μm diameter Pt wire (Alfa Aesar, 99.95%) is attached to a W rod (0.254 mm diameter, FHC, Inc.) using Ag conductive adhesive paste (Alfa Aesar). The Pt wire is electrochemically etched to produce a sharp tip; (2) the sharpened Pt tip is sealed in a glass capillary (Dagan Corp., Prism glass capillaries, SB16, 1.65 mm outer diameter, 0.75 mm inner diameter, softening point 700 °C) using a H_2/air flame; (3) the capillary is polished until a Pt nanodisk is exposed. This process is monitored by an electrical continuity circuit; (4) the exposed Pt disk is then etched in a 20% $CaCl_2$ solution by applying a 5.9 V ac voltage between the Pt nanoelectrode and a large-area Pt wire electrode, after which the entire Pt wire is gently pulled from the glass to yield a conical-shaped nanopore. The radii of small orifices of the GNMs are determined from the ionic resistance of the nanopore (R) in a 1.0 M KCl solution. The ionic current is measured as a function of the voltage between internal and external Ag/AgCl electrodes. From the slope of i-V curve, the radius (r_i) is calculated using a simplified expression $r_i = 19/R$.[13] The radii of the nanopores used in the studies were 185, 30, and 207 nm, with a relative uncertainty of ~10%.

4.2.3 Cell configuration and data acquisition

A Pine RDE3 potentiostat/waveform generator (or a Princeton Applied Research model 175 Universal Programmer) and a Dagan Chem-Clamp potentiostat were interfaced to a computer through a PCI 6251 data acquisition card (National Instruments). Voltammetric data (*i*-*V* curves) were recorded by in-house virtual instrumentation written in LabVIEW (National Instruments). The GNM was filled and immersed in a 0.01 M KCl and 0.1 mM K_2HPO_4 / KH_2PO_4 buffer solution (pH 7.3). A potential difference was applied across the GNM using Ag/AgCl electrodes. Pressure was applied using a 10 mL gastight syringe and monitored with a Traceable Pressure Meter (Fisher Scientific, model 06-662-69). The sign of pressure is defined as the pressure inside the GNM capillary versus the external solution. A schematic drawing of the experimental setup is presented in Figure 4.1.

i-*V* curves were recorded by scanning the potential between the two Ag/AgCl electrodes from -0.4 to +0.4 V. The small offset currents were adjusted at 0 mmHg applied pressures. The offsets were less than 0.1 nA and variable in sign. The pressure-driven flows generally result in streaming currents less than 0.1 nA in our experiments (typically, negative streaming currents for negative pressures and positive currents for positive pressures). The *i*-*V* curves and the rectification factor were not corrected for the offsets caused by the streaming current.

4.2.4 Finite-element simulations

The finite-element simulations were performed using COMSOL Multiphysics 3.5a (Comsol, Inc.) on a high-performance desktop computer (16 GB RAM).

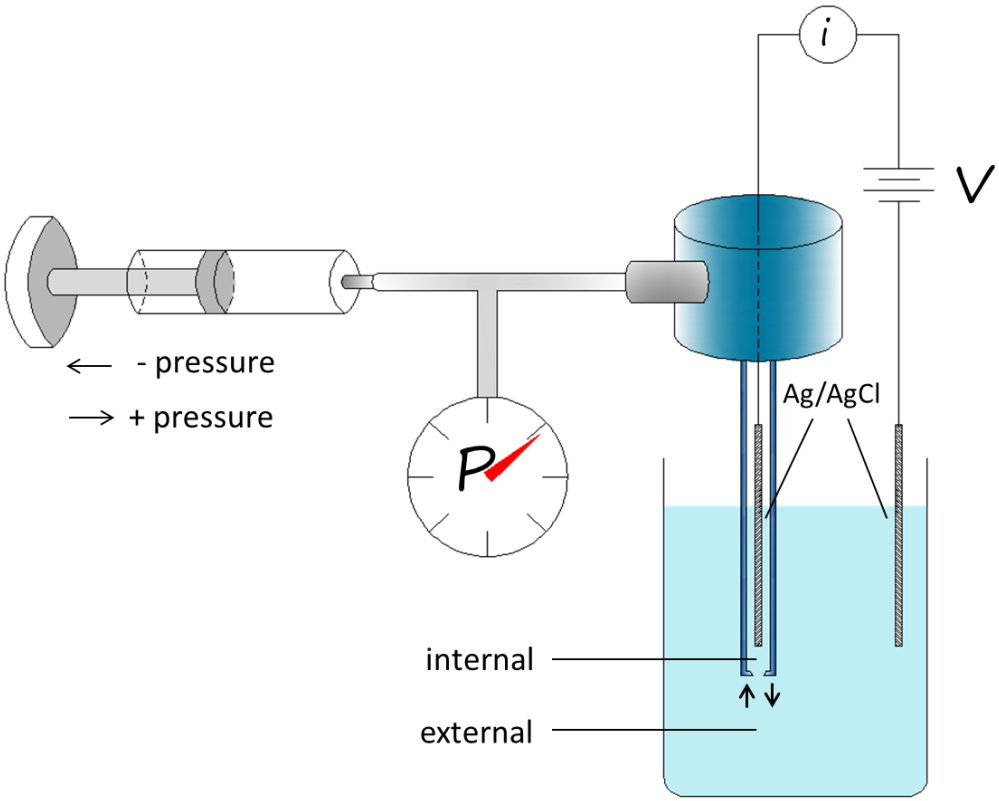

Figure 4.1. A schematic illustration of a GNM and the experimental setup used to control the pressure-driven flow through the nanopore while measuring the *i*-*V* responses.

4.3 Results and discussion

4.3.1 Ion current rectification in conical-shaped glass nanopores

GNMs containing a single conical-shaped nanopore in a glass membrane at the end of a glass capillary were prepared as previously described. The radii of the small orifices were determined by measuring the nanopore resistance in a 1 M KCl solution. The GNMs were rinsed with water and then filled with and immersed in a 0.01 M KCl solution (pH 7.3). Pressure was applied across the membrane using a syringe connected to the glass capillary containing the GNM (Figure 4.1). The signs of both pressure and potential are defined as the value inside the nanopore relative to the value in the external solution.

Figure 4.2 shows the *i*-*V* responses for nanopores with radii of 185 and 30 nm at pressures ranging from -160 to 160 mmHg (all radii herein refer to the dimension of the small orifice of the nanopore). In the absence of pressure, both nanopores displayed a significant nonlinear *i*-*V* response, similar to previous reports.[10] Several models have been proposed to account for the phenomena of ICR. Here, we use the ion depletion and accumulation model to qualitatively explain the ICR. Since the nanopore surface is negatively charged at neutral pH and the radius of the pore orifice is small, the region at the pore opening is cation-selective. At negative potentials, the K^+ flux is directed from the external bulk solution to the pore interior while Cl^- moves in the opposite direction. As the pore is cation-selective, Cl^- ions are rejected by the glass surface because of electrostatic repulsion. A consequence of anion rejection is an increase in the K^+ and Cl^- concentrations within the pore interior, resulting in nanopore conductivity greater than that based on the KCl concentration in the bulk solution. Conversely, when a positive

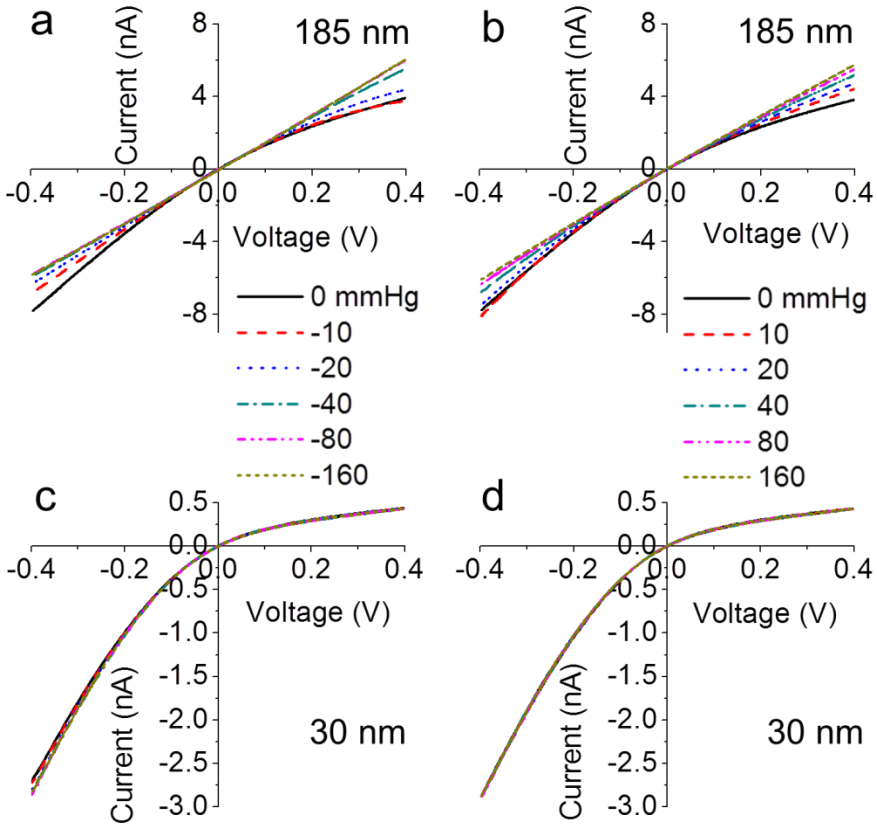

Figure 4.2. Pressure-dependent *i-V* responses of conical-shaped GNMs with radii of (a, b) 185 and (c, d) 30 nm in a 0.01 M KCl solution containing 0.1 mM phosphate buffer (pH 7.3). The scan rates were 30 and 50 mV/s for the 185 and 30 nm radius nanopores, respectively. The *i-V* curves in the left column correspond to negative applied pressures, and those in the right column to positive pressures (pore interior vs external solution).

potential relative to the external solution is applied inside the pore, the transport of Cl^- from the external solution to the internal solution is rejected by the surface charges, depleting Cl^- within the pore interior and thus decreasing the nanopore conductivity and the observed ionic current.[14,15] A larger conical-shaped nanopore displays a weaker rectification than a smaller pore because of the smaller extent of the ion electrical double layer into the pore. The above explanation is quantitatively supported by previous finite-element simulations in which the ion depletion and accumulation were observed by solving the Nernst-Planck and Poisson equations simultaneously.[16]

4.3.2 Pressure-dependent ion current rectification in glass nanopores

The 185 and 30 nm radius nanopores displayed qualitatively different ICR behaviors when negative or positive pressure was applied across the GNM. As shown in Figure 4.2a and b, an applied pressure across the larger pore (185 nm) resulted in a more ohmic *i*-*V* response. The rectification factor, defined as the ratio of the ion current magnitude at -0.4 V to that at +0.4 V, decreased from ~2 to ~1 as the pressure increased from 0 to ±160 mmHg. Application of negative pressures reduced the ICR slightly more effectively than positive pressures, as shown in Figure 4.3a for positive and negative pressures between 0 and 160 mmHg. The dependence of the rectification factor on pressure was reversible, as shown in Figure 4.3b for pressure cycling between 0 and ±80 mmHg. In contrast, applied pressure had negligible effect on the more highly rectified *i*-*V* response of the smaller pore (30 nm, Figure 4.2c, d). The rectification ratio was ~6.6 at all pressures. In general, we observed a significant pressure dependence of the ICR for nanopores with radii of ~180 nm or larger.

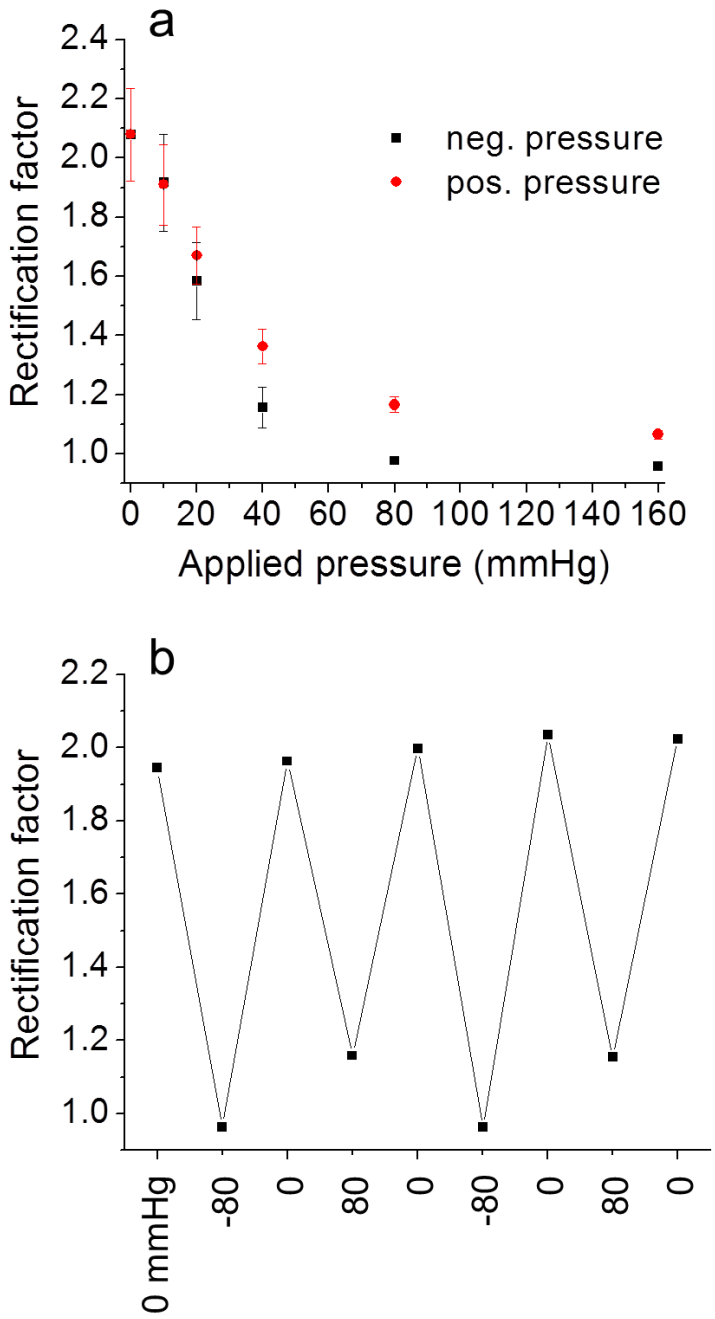

Figure 4.3. (a) Rectification factor as a function of applied pressure for a conical-shaped nanopore with a radius of 185 nm in a 0.01 M KCl solution (pH 7.3). (b) Rectification factor during pressure cycling between 0 and ±80 mmHg.

The pressure-dependent ICR behavior can be readily understood in terms of the effect of flow on the ion distributions near the nanopore orifice. The applied pressure across the GNM engenders a volumetric flow Q through the conical-shaped nanopore, estimated by $Q = 3\pi r^3 \Delta P/(8\eta \cot\theta)$, where r is the radius of the pore orifice, ΔP is the pressure difference across the nanopore, η is the solution viscosity, and θ is the half-cone angle of the nanopore.[17] Q is proportional to r^3 at constant ΔP. Thus, the volumetric rate is greater by a factor of ~235 for the 185 nm radius GNM than for the 30 nm radius GNM. The flow brings solution containing bulk concentrations of K^+ and Cl^- ions (0.01 M) into the nanopore, disrupting the equilibrium ion concentrations induced by the charged glass surface. Finite-element simulations employing the Navier-Stokes equation to compute the fluid velocity distributions near the pore orifice (Figure 4.4) demonstrated that an applied pressure of 80 mmHg creates a large velocity gradient near the orifice of a 185 nm radius pore but has a relatively negligible effect on the flow through a 30 nm radius pore. These results indicate that an applied pressure should result in qualitatively different ICR dependences for large and small nanopores, in agreement with the data shown in Figure 4.2. Qualitatively, the different dependences of Q and the ion distributions on the pore size result in different pressure-dependent ICR behaviors as a function of nanopore size.

In order to better understand the pressure- and size-dependent i-V behaviors, finite-element computations were performed to simultaneously solve the Nernst-Planck equation for the ion fluxes, the Poisson equation relating the ion concentrations to the local electric field, and the Navier-Stokes equation for solution flow. The simulations were similar to the ICR simulations published previously,[16] and details of the simulation

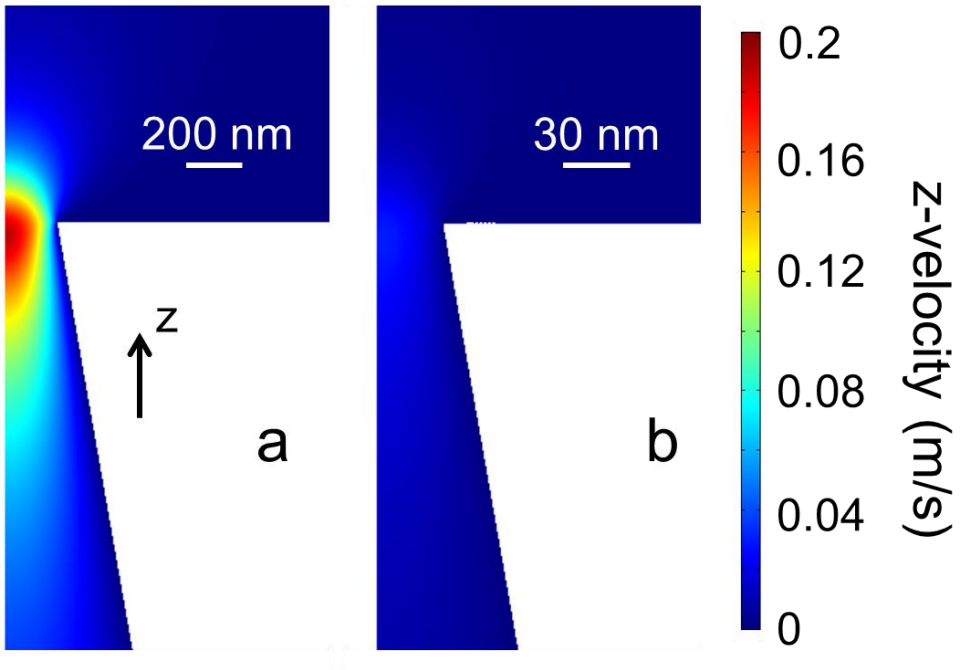

Figure 4.4. Simulated *z* velocity distributions (two-dimensional axial) for nanopores with radii of (a) 185 and (b) 30 nm at an applied pressure of 80 mmHg.

boundary conditions and so on are presented in the Appendix.

Figure 4.5a shows distributions of the total ion concentration (K^+ and Cl^-) near the pore orifice at different potentials and pressures for a 185 nm radius GNM. In the absence of an applied pressure (0 mmHg, middle column), the depletion of ions in the pore interior at positive potential and the accumulation of the ions at negative potential are apparent, and they result in significant ICR as previously described. Upon application of a pressure, the induced flow brings in solution containing K^+ and Cl^- ions at their bulk concentrations (0.01 M), removing the depletion or excess of ions responsible for ICR. Thus, the total concentration at the orifice is closer to that of the bulk solution, resulting in a more ohmic behavior in agreement with the experimental observations. The simulations also indicated that for the 185 nm radius pore, negative pressures are slightly more effective in producing a uniform concentration distribution within the pore. A consequence of the asymmetry in the pressure dependence is that negative pressures are more effective than positive pressures in producing an ohmic *i*-*V* response, as shown in Figure 4.3.

The finite-element simulations of the total ion concentration for the 30 nm radius pore (Figure 4.5b) also demonstrated that an applied pressure has negligible effect on ICR for this pore. Although larger ion depletion/accumulation effects and thus a more pronounced rectified *i*-*V* response are associated with the smaller nanopore, the greatly reduced rate of flow through the smaller nanopore results in an insignificant pressure dependence of the ICR.

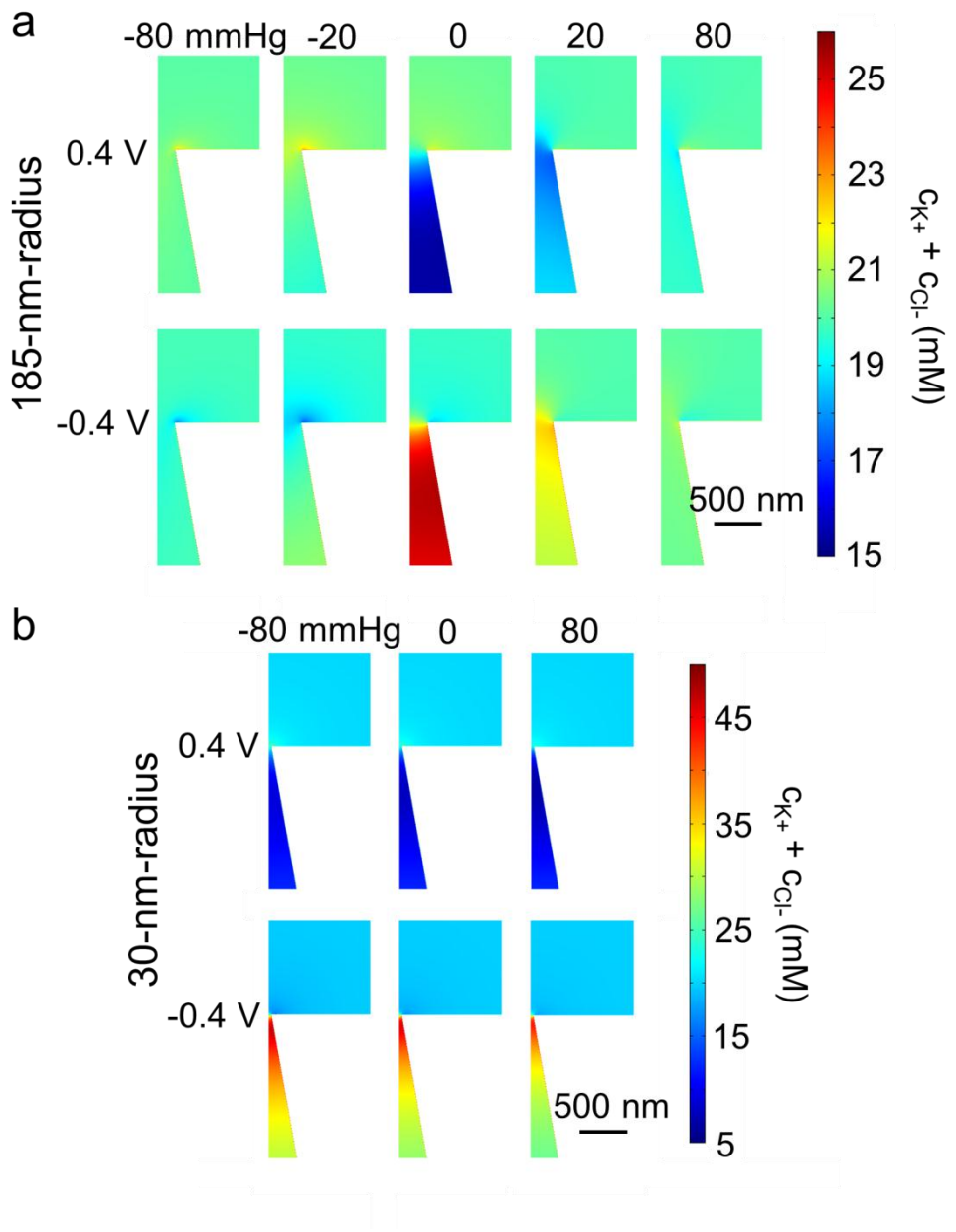

Figure 4.5. Simulated distributions of the total ion concentration (K^+ and Cl^-) near the orifice for GNMs with radii of (a) 185 and (b) 30 nm as functions of applied potential and pressure (both pore interior vs external solution) in 0.01 M KCl solution.

Figure 4.6a and b show solution conductivity profiles along the central nanopore axis (r = 0) at different pressures and potentials for a 185 nm radius pore. The conductivity in the pore decreases at the positive potential and increases at the negative potential relative to the value of the bulk 0.01 M KCl solution (0.15 S/m) in contact with the nanopore on both sides, consistent with the qualitative explanation of ICR presented above and reported previously.[16] When a negative or positive pressure (80 mmHg in magnitude) is applied across the pore, the gradient in the electric conductivity nearly vanishes. The flat conductivity profiles at 80 and -80 mmHg correspond more closely to that for an uncharged nanopore, in which no ion depletion or accumulation is expected (or observed in finite-element simulations). The simulations in Figure 4.6 also demonstrate that the direction of the applied pressure across the GNM (+80 vs -80 mmHg) results in a small but significant difference in the nanopore conductivity at both positive and negative voltages. At the positive voltage, application of 80 mmHg nearly restores the nanopore conductivity to the bulk-solution value (Figure 4.6a), but a small residual decrease in conductivity is observed around the pore orifice (z = 0). Conversely, at -80 mmHg, a small residual increase in conductivity is observed. The difference between the residuals at negative and positive pressures may be responsible for the small difference in the experimental i-V curves at ±80 mmHg. In contrast, the conductivity profiles for a 30 nm radius pore (Figure 4.6c, d) are nearly independent of the applied pressure, consistent with the applied pressure having a negligible effect on the i-V response (Figure 4.2).

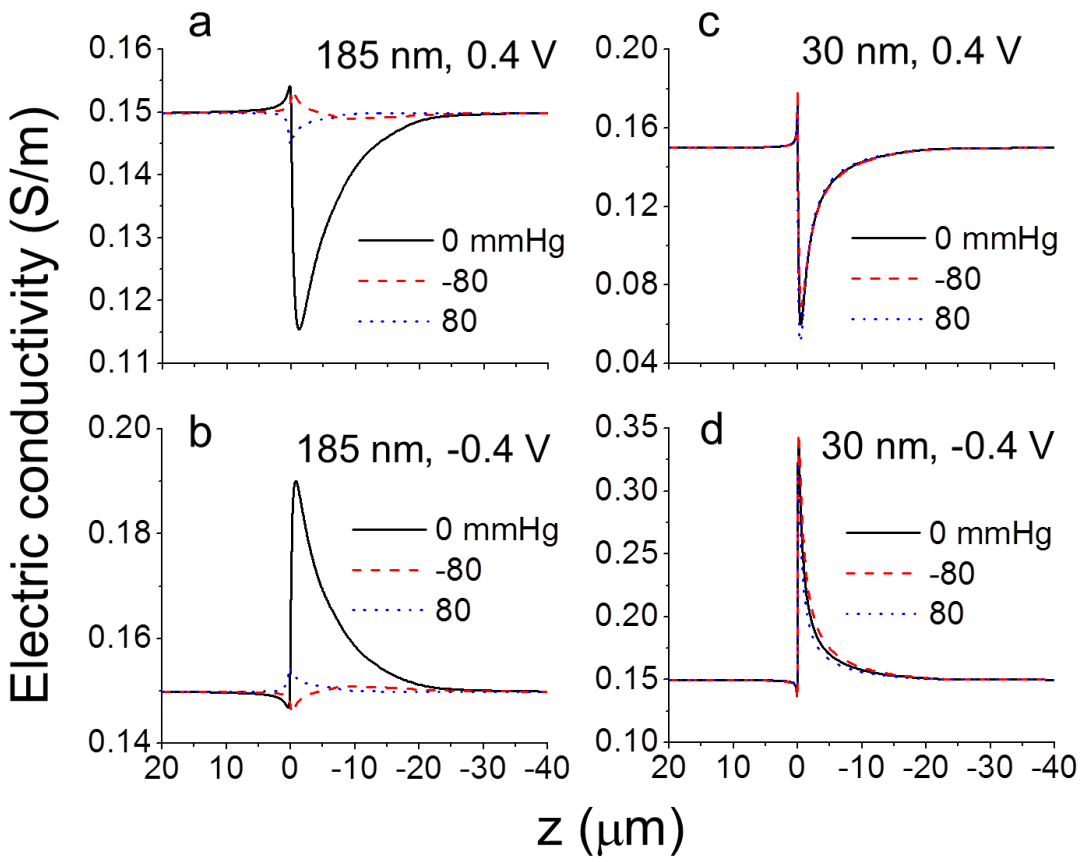

Figure 4.6. Simulated electric conductivity distributions for pores with radii of (a, b) 185 and (c, d) 30 nm as functions of distance along the central pore axis under different pressures at (a, c) 0.4 and (b, d) -0.4 V (pore interior vs external solution). The opening of the pore is located at $z = 0$ μm in each figure; $z < 0$ μm corresponds to the nanopore interior and $z > 0$ μm to the external solution.

Simulations of the full pressure-dependent *i*-*V* curves for nanopores with radii of 185 and 30 nm are presented in the Appendix. While the finite-element simulations successfully predict all of the qualitative trends of the pressure-dependent rectification, they fail to predict rectification factors that quantitatively match the experimental observations at different applied pressures. Both our experiments and simulations suggest that overlap of the electrical double layer is apparently not required to achieve significant ICR, in agreement with phenomena reported previously by Jacobson,[18] Wang,[19] and our group.[13] For a 0.01 M KCl solution as employed here, the electrical double layer associated with the glass surface charge is ~15 nm (5 times the Debye length) and thus extends only a fraction of the distance into the interior of the 185 nm radius nanopore. It is also worthwhile to mention that the currents at negative potentials under small positive pressures were sometimes slightly larger than the currents in the absence of pressure (e.g., compare the red dashed line for 10 mmHg and the black solid line at 0 mmHg in Figure 4.2b). However, this phenomenon was not reproducibly observed for all GNMs of similar size (Appendix). The origin of this second-order effect is not understood; we speculate that flow at low pressure results in a small compression of the ion concentration gradients at the pore orifice, producing a slightly higher conductivity at negative potentials.

4.4 Conclusions

In summary, we have reported a previously unobserved but fundamental aspect of the relationship between fluid flow and ion fluxes in an electrically charged nanopore. The ion redistributions around the nanopore orifice are determined by a combination of the electrostatic forces associated with the surface charge and finite solution conductivity and by the volumetric flow induced by the pressure. Finite-element simulations of the

electric field, ion concentration, and flow rate have provided insight into the origin of the pressure-dependent ICR and are in semiquantitative agreement with the experimental observations.

4.5 Appendix

4.5.1 Estimation of the GNM surface charge

The surface charge density on the glass nanopore membrane, σ (C/m^2), is estimated using the method described by Behrens and Grier.[20] The surface charge arises from the dissociation of the surface bound silanol groups and depends on the number of active surface sites and the *pK* of the dissociation reaction. The surface charge increases with increasing ionic strength and increasing *pH* value and can be estimated from the following equations that are based on the Stern layer's phenomenological capacity and the Poisson-Boltzmann equation,

$$\varphi_d(\sigma) = \frac{RT}{F} In \frac{-\sigma}{e\Gamma + \sigma} - (pH - pK)\frac{RT}{F} In10 - \frac{\sigma}{C} \tag{4.1}$$

$$\sigma(\varphi_d) = \frac{2\varepsilon\varepsilon_0 \kappa RT}{F} \sinh(\frac{F\varphi_d}{2RT}) . \tag{4.2}$$

In eqs 4.1 and 4.2, φ_d is the diffuse layer potential, *e* is the absolute value of elementary charge, Γ is the concentration of head groups, *pK* is the logarithmic dissociation constant, *C* is the Stern layer's phenomenological capacity, *F* is the Faraday's constant, *R* is the gas constant, $\varepsilon\varepsilon_0$ is the solution permittivity, *T* is the absolute

temperature, and κ^{-1} is the Debye screening length.

Eqs 4.1 and 4.2 were solved numerically using the Table and FindRoot functions in Mathematica 6.0. For an electrolyte concentration of 0.01 M, κ^{-1} is ~3 nm and the surface charge is calculated to be ~ -0.026 C/m^2. Other parameters used in the calculation are C = 2.9 F/m^2, pK = 7.5, pH = 7.3, Γ = 8 nm^{-2}, ε = 78, as described by Behrens and Grier.[20]

4.5.2 Finite-element simulations

The pressure-dependent voltammetric response of a conical-shaped nanopore was computed by finite-element simulations. The model is similar to a previously published simulation of ion current rectification in a quiet solution.[16] The calculation procedure is outlined as follows. The ion fluxes are modeled by the Nernst-Planck equation:

$$\mathbf{J}_i = -D_i \nabla c_i - \frac{z_i F}{RT} D_i c_i \nabla \Phi + c_i \mathbf{u} \quad . \tag{4.3}$$

In eq 4.3, $\mathbf{J}_i$, D_i, c_i, and z_i are, respectively, the ion flux vector, diffusion coefficient, concentration, and charge of species i in solution. Φ and $\mathbf{u}$ are the local electric potential and fluid velocity, and F, R, and T are the Faraday's constant, the gas constant, and the temperature, respectively.

The GNM surface is negatively charged, creating an electrical double layer within the nanopore. The relationship between the local electric potential Φ and ion concentrations c_i is given by the Poisson equation, eq 4.4,

$$\nabla^2\Phi = -\frac{F}{\varepsilon}\sum_i z_i c_i \tag{4.4}$$

where ε is the dielectric constant of the solution.

The pressure-driven flow through the nanopore is described by the Navier-Stokes equation, eq 4.5, relating pressure and fluid velocity.

$$\mathbf{u}\nabla\mathbf{u} = \frac{1}{\rho}(-\nabla P + \eta\nabla^2\mathbf{u}) \tag{4.5}$$

In eq 4.5, ρ and η are the density and the viscosity of the fluid, and P is the pressure. Due to the truncated conical geometry of the GNM, analytical solutions to the above three equations are almost impossible. Electroosmotic flow in the nanopore was ignored in the simulation.

Finite-element simulations were performed to obtain solutions for the ion concentration distributions, ionic currents, and flow distributions at different potentials and pressures. The geometry of the model is shown in Figure 4.7, employing a 2D axial symmetric system (cylindrical coordinate). The orifice radius of the GNM was set to be 185 or 30 nm, corresponding to the geometry of the GNMs used in this study. The length of the GNM was set to be 20 μm. To approximate the semiinfinite solution of the experiment, the exterior boundary of bulk solution in the model was extended to a distance r = 20 μm and z = 20 μm away from the pore. The glass surface of the nanopore was defined as a charged insulating boundary. The surface charge was only applied to the orange lines shown in Figure 4.7 due to computational limitations. As previously reported

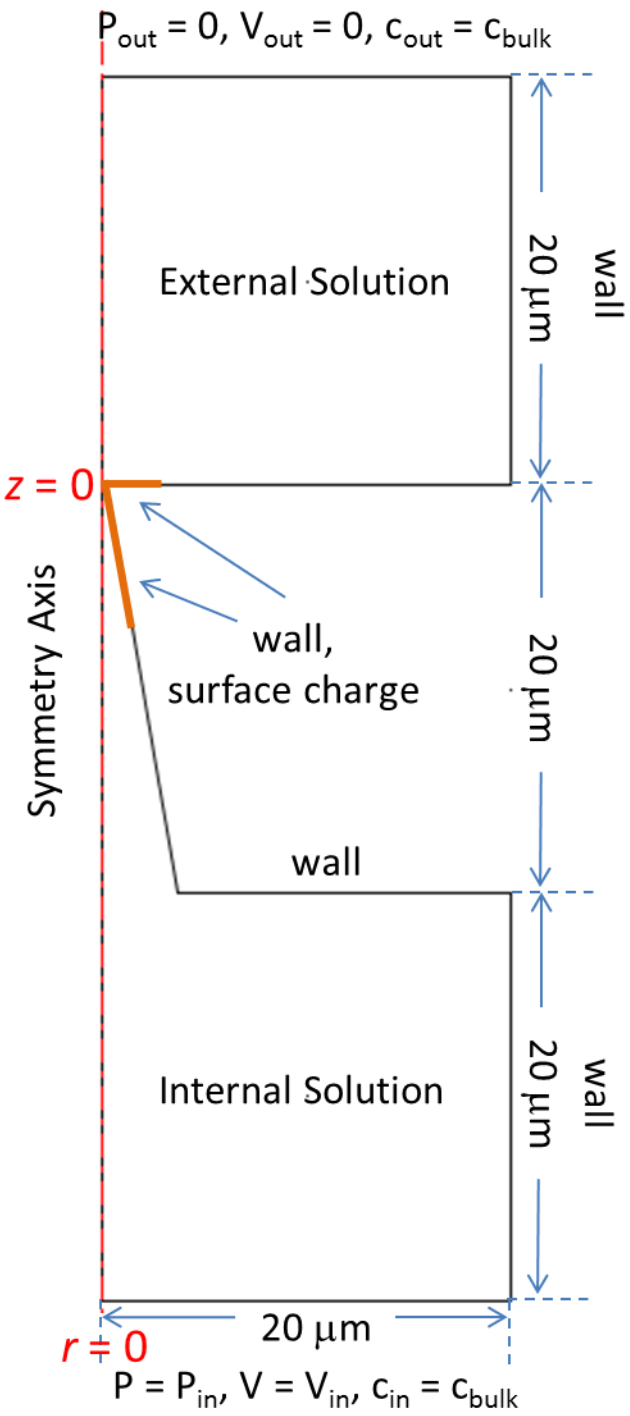

Figure 4.7. The 2D axial symmetric geometry of the GNM and boundary settings for the finite-element simulation.

by Kubeil and Bund, a charged surface of 3 μm length is sufficient to accurately describe the ICR effects.[16] An adaptive mesh refinement was used to optimize the mesh, and the mesh size at the conical orifice is refined down to less than 1 nm to obtain a more accurate ionic current value. The electrolyte solution parameters for the ionic species were chosen to reflect a 0.01 M KCl solution (D_{K+} = 1.957 × 10^{-9} m^2/s, c_{K+} = 0.01 M, z_{K+} = +1, D_{Cl-} = 2.032 × 10^{-9} m^2/s, c_{Cl-} = 0.01 M, z_{Cl-} = -1, T = 298 K, η = 8.9 × 10^{-4} Pa s).

Figure 4.8 and 4.9 show the simulated electric conductivity distributions and *i-V* curves for nanopores with radii of 185 and 30 nm in the absence and presence of applied pressures.

4.5.3 Pressure-dependent *i-V* curves for a 207 nm radius nanopore

Figure 4.10 shows the experimental pressure-dependent *i-V* curves for a 207 nm radius conical-shaped glass nanopore.

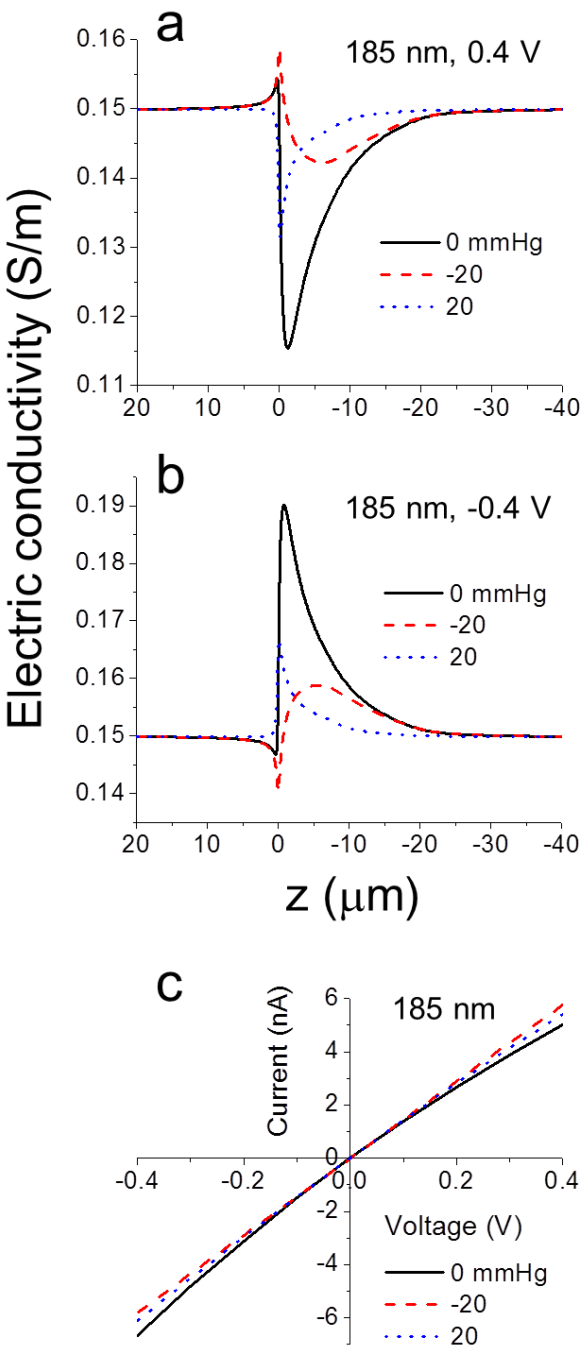

Figure 4.8. (a), (b) Simulated electric conductivity distributions for a 185 nm radius pore as a function of distance along the central pore axis under pressures at 0.4 V and -0.4 V internal vs. external. The opening of the pore is located at z = 0 μm in each figure. Values of z < 0 μm correspond to the nanopore interior, while values of z > 0 μm correspond to the external solution. (c) Simulated *i-V* curves for a 185 nm radius pore with and without applied pressures.

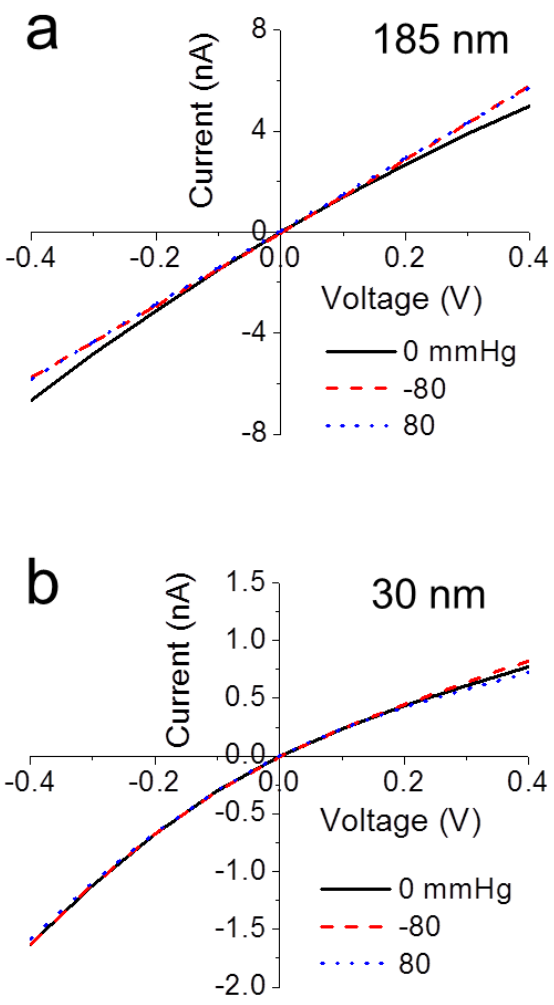

Figure 4.9. Simulated *i*-*V* curves for nanopores with radii of (a) 185 and (b) 30 nm in the absence and presence of applied pressures.

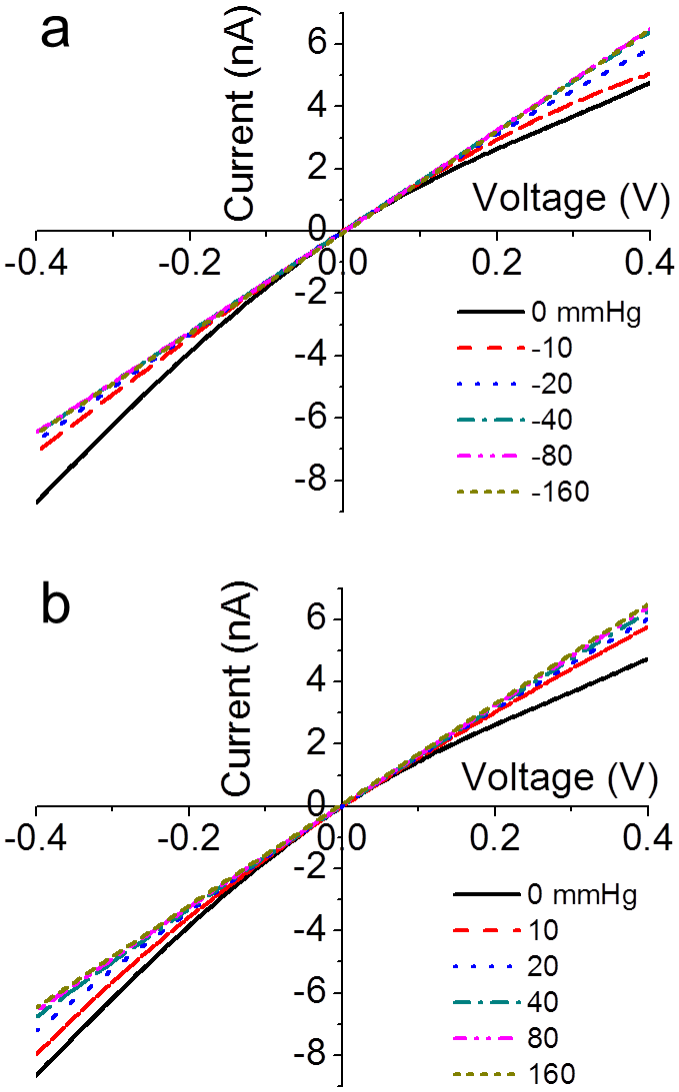

Figure 4.10. Experimental *i-V* responses of a 207 nm radius conical-shaped GNM in a 0.01 M KCl solution at pH 7.3 containing 0.1 mM phosphate buffer under (a) negative and (b) positive pressures. The scan rate was 50 mV/s.

4.6 References

(1) Lan, W. J.; Holden, D. A.; White, H. S. *J. Am. Chem. Soc.* **2011**, *133*, 13300-13303.

(2) Wei, C.; Bard, A. J.; Feldberg, S. W. *Anal. Chem.* **1997**, *69*, 4627-4633.

(3) (a) Jin, P.; Mukaibo, H.; Horne, L. P.; Bishop, G. W.; Martin, C. R. *J. Am. Chem. Soc.* **2010**, *132*, 2118-2119. (b) Sexton, L. T.; Mukaibo, H.; Katira, P.; Hess, H.; Sherrill, S. A. Horne, L. P.; Martin, C. R. *J. Am. Chem. Soc.* **2010**, *132*, 6755-6763. (c) Sexton, L. T.; Horne, L. P.; Sherrill, S. A.; Bishop, G. W.; Baker, L. A.; Martin, C. R. *J. Am. Chem. Soc.* **2007**, *129*, 13144-13152. (d) Siwy, Z. S.; Trofin, L.; Kohli, P.; Baker, L. A.; Trautmann, C.; Martin, C. R. *J. Am. Chem. Soc.* **2005**, *127*, 5000-5001.

(4) (a) Yusko, E. C.; An, R.; Mayer, M. *ACS Nano* **2010**, *4*, 477-487. (b) Han, J. H.; Kim, K. B.; Kim, H. C.; Chung, T. D. *Angew. Chem. Int. Ed.* **2009**, *48*, 3830-3833. (c) Umehara, S.; Pourmand, N.; Webb, C. D.; Davis, R. W.; Yasuda, K.; Karhanek, M. *Nano Lett.* **2006**, *6*, 2486-2492.

(5) Guerrette, J. P.; Zhang, B. *J. Am. Chem. Soc.* **2010**, *132*, 17088-17091.

(6) (a) Sa, N. Y.; Baker, L. A. *J. Am. Chem. Soc.* **2011**, *133*, 10398-10401. (b) Sa, N. Y.; Fu, Y. Q.; Baker, L. A. *Anal. Chem.* **2010**, *82*, 9963-9966.

(7) (a) Vlassiouk, I.; Kozel, T. R.; Siwy, Z. S. *J. Am. Chem. Soc.* **2009**, *131*, 8211-8220. (b) He, Y.; Gillespie, D.; Boda, D.; Vlassiouk, I.; Eisenberg, R. S.; Siwy, Z. S. *J. Am. Chem. Soc.* **2009**, *131*, 5194-5202. (c) Siwy, Z.; Heins, E.; Harrell, C. C.; Kohli, P.; Martin, C. R. *J. Am. Chem. Soc.* **2004**, *126*, 10850-10851. (d) Vlassiouk, I.; Siwy, Z. S. *Nano Lett.* **2007**, *7*, 552-556.

(8) (a) Yameen, B.; Ali, M.; Neumann, R.; Ensinger, W.; Knoll, W.; Azzaroni, O. *J. Am. Chem. Soc.* **2009**, *131*, 2070-2071. (b) Ali, M.; Yameen, B.; Cervera, J.; Ramirez, P.; Neumann, R.; Ensinger, W.; Knoll, W.; Azzaroni, O. *J. Am. Chem. Soc.* **2010**, *132*, 8338-8348. (c) Ali, M.; Nguyen, Q. H.; Neumann, R.; Ensinger, W. *Chem. Commun.* **2010**, *46*, 6690-6692.

(9) (a) Hou, X.; Yang, F.; Li, L.; Song, Y.; Jiang, L.; Zhu, D. *J. Am. Chem. Soc.* **2010**, *132*, 11736-11742. (b) Xia, F.; Guo, W.; Mao, Y.; Hou, X.; Xue, J.; Xia, H.; Wang, L.; Song, Y.; Ji, H.; Ouyang, Q.; Wang, Y.; Jiang, L. *J. Am. Chem. Soc.* **2008**, *130*, 8345-8350. (c) Hou, X.; Dong, H.; Zhu, D.; Jiang, L. *Small* **2010**, *6*, 361-365.

(10) Siwy, Z. S. *Adv. Funct. Mater.* **2006**, *16*, 735-746.

(11) (a) Zhang, B.; Galusha, J.; Shiozawa, P. G.; Wang, G.; Bergren, A. J.; Jones, R. M.; White, R. J.; Ervin, E. N.; Cauley, C. C.; White, H. S. *Anal. Chem.* **2007**, *79*,

4778-4787. (b) Schibel, A. E. P.; Edwards, T.; Kawano, R.; Lan, W. J.; White, H. S. *Anal. Chem.* **2010**, *82*, 7259-7266.

(12) (a) Lan, W. J.; Holden, D. A.; Zhang, B.; White, H. S. *Anal. Chem.* **2011**, *83*, 3840-3847. (b) White, R. J.; Ervin, E. N.; Yang, T.; Chen, X.; Daniel, S.; Cremer, P. S.; White, H. S. *J. Am. Chem. Soc.* **2007**, *129*, 11766-11775. (c) Holden, D. A.; Hendrickson, G.; Lyon, L. A.; White, H. S. *J. Phys. Chem. C* **2011**, *115*, 2999-3004.

(13) White, R. J.; Zhang, B.; Daniel, S.; Tang, J. M.; Ervin, E. N.; Cremer, P. S.; White, H. S. *Langmuir* **2006**, *22*, 10777-10783.

(14) Woermann, D. *Phys. Chem. Chem. Phys.* **2003**, *5*, 1853-1858.

(15) Cervera, J.; Schiedt, B.; Ramirez, P. *Europhys. Lett.* **2005**, *71*, 35-41.

(16) (a) White, H. S.; Bund, A. *Langmuir* **2008**, *24*, 2212-2218. (b) Kubeil, C.; Bund, A. *J. Phys. Chem. C* **2011**, *115*, 7866-7873. (c) Ai, Y.; Zhang, M.; Joo, S. W.; Cheney, M. A.; Qian, S. *J. Phys. Chem. C* **2010**, *114*, 3883-3890.

(17) Lan, W. J.; Holden, D. A.; Liu, J.; White, H. S. *J. Phys. Chem. C* **2011**, *115*, 18445-18452.

(18) (a) Kovarik, M. L.; Zhou, K. M.; Jacobson, S. C. *J. Phys. Chem. B* **2009**, *113*, 15960-15966. (b) Perry, J. M.; Zhou, K.; Harms, Z. D.; Jacobson, S. C. *ACS Nano* **2010**, *4*, 3897-3902.

(19) Feng, J.; Liu, J.; Wu, B.; Wang, G. *Anal. Chem.* **2010**, *82*, 4520-4528.

(20) Behrens, S. H.; Grier, D. G. *J. Chem. Phys.* **2001**, *115*, 6716-6721.

CHAPTER 5

CAPTURING AND RELEASING INDIVIDUAL PARTICLES IN A NANOPORE

5.1 Introduction

Capture and release of individual nanoparticles as they are driven through a conical-shaped glass nanopore membrane (GNM) by pressure-induced flow is reported. In these experiments, one to several hundred particles are driven through the orifice of the nanopore. Following the initial translocation, the pressure is reversed and the particles are driven through the GNM orifice in the reverse direction. The resistive pulse technique is used to monitor the particle capture and release translocations. The size of the particles (120 to 160 nm) and the direction of translocation can be determined from the pulse amplitude and shape. The stochastic nature of particle trajectories has been investigated, including instantaneous transfer rate, return probability, and cumulative release success rate. We demonstrate that the sequence of particle translocations in the capture step (*a*, *b*, *c*… where the letters represent different particles) is largely preserved and can be read out by resistive pulse signature during the release translocations (…*c*, *b*, *a*). The observed stochastic events are in good agreement with finite-element simulations of particle trajectory within the confined geometry of the nanopore. The pressure reversal technique opens new avenues for chemical analysis of particles using resistive pulse methods.[1]

We report a pressure-reversal, resistive-pulse method to capture and release nanoparticles using a conical-shaped nanopore. The objective of this study is to probe the behavior of particle trajectories during translocation through a nanopore. The resistive-pulse technique was invented by W. H. Coulter in 1953 as a means of counting and sizing particles in a conducting fluid.[2] Particles in a weak electrolyte solution are driven through an orifice separating two Ag/AgCl electrodes and the current between the electrodes is momentarily interrupted when a particle passes through the orifice.[3] Typically, the rate of particle translocation is used to determine the solution particle concentration, while the duration time and the peak height are analyzed to determine the particle size and shape. During the past decade, the development of both synthetic[4-8] and biological nanopores[9-14] has attracted significant attention due to the application of the resistive-pulse method in analyses of nanoparticles[15-19] and molecules[20-22].

A pressure-reversal technique using cylindrical micropores (3-30 μm in diameter) was first reported by Berge and Jossang in 1989.[23,24] A trigger signal from the particle translocation event was used to activate two miniature solenoid valves to control the direction of pressure-driven flow. Capture and release translocations were demonstrated for particles, bacteria, and dissolving air bubbles. More recently, Gershow and Golovchenko studied the forward and reverse translocation of a single DNA molecule through a solid-state nanopore by reversing the transmembrane potential direction after the initial translocation, and they used numerical solutions of a drift-diffusion physical model to analyze the probability of observing the release translocation.[25,26] Meller[27], Hibbs[28] and coworkers also applied similar voltage switching methods to investigate diffusional motion of single-stranded DNA in a protein channel.

The experiment reported herein is depicted in Figure 5.1. Pressure applied across a glass nanopore membrane (GNM) is controlled using a gastight syringe. The GNM, schematically shown in Figure 5.2, is a single conical nanopore embedded in a thin glass membrane (50 to 100 μm), with the smaller-radius orifice facing the external solution. The GNM is fabricated using simple bench-top methods previously described by this laboratory.[29] A three-part pressure waveform, Figure 5.1a, is used to drive an individual particle or a large group of particles back and forth through the GNM orifice. Upon application of a negative pressure inside the GNM (*-P*), Figure 5.1b, the particle is initially driven from the external solution through the pore orifice, generating a pulse in the *i-t* recording. After a pre-set period of time, τ, following the initial translocation, the pressure is switched to a positive pressure (*+P*) and the same particle translocates through the pore orifice in the opposite direction, generating a current pulse at release time τ_r. In the absence of any stochastic influences, τ_r should equal τ if the initial (*-P*) and reversal (*+P)* pressure are identical. This assumes that the nanoparticle's motion is determined by the velocity of the solution through the nanopore, which is proportional to the applied pressure. A consequence of this equivalence of τ_r and τ is that when multiple particles are driven through the orifice, the order in which they re-translocate, upon the pressure reversal, is reversed to the order of the initial translocation. That is, the time sequence of particle translocations in the capture step (τ_a, τ_b, τ_c … where the letters represent different particles) is preserved and can be read out by resistive pulses during the release translocations (…τ_{rc}, τ_{rb}, τ_{ra}). In this chapter, we show that this sequence information is largely preserved, but that diffusional motion of the particle introduces a stochastic broadening of the particle location and, thus, τ_r.

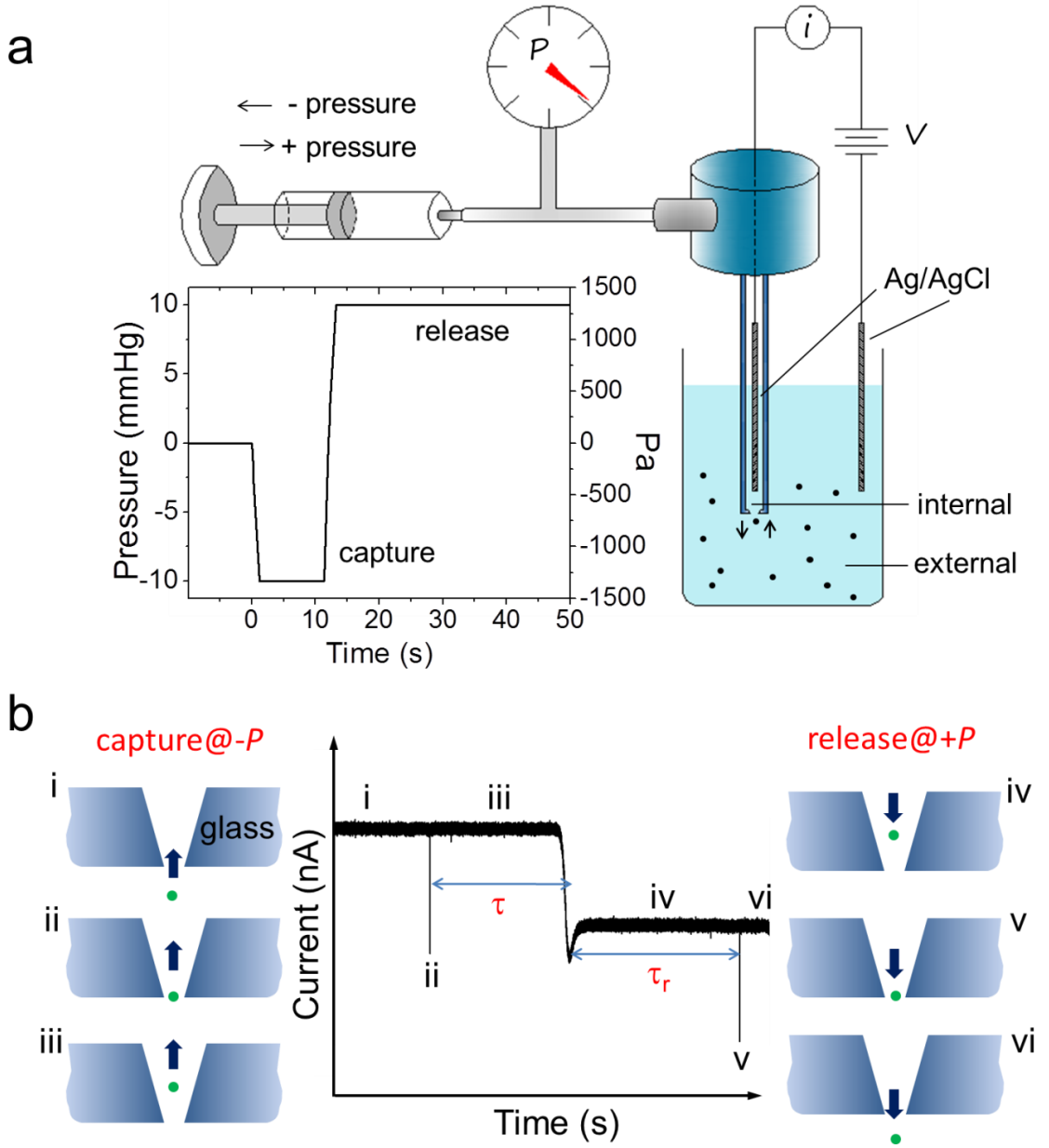

Figure 5.1. (a) Schematic illustration of glass nanopore membrane (GNM), and particle capture and release method using a three-part pressure waveform. (b) Schematic of the particle translocation and resulting *i-t* recording. The arrows represent the direction of particle movement. (i) The particle moves towards the pore orifice from the external solution after the initial application of -*P*. (ii) The particle translocates through the pore, generating a pulse in the *i-t* recording. (iii) The particle continues travelling into the pore interior under pressure-driven flow. (iv) The pressure is reversed (+*P*) at τ, and the particle moves towards the pore. (v) The particle translocates through the pore at τ_r generating a second resistive pulse and (vi) returns to the external solution.

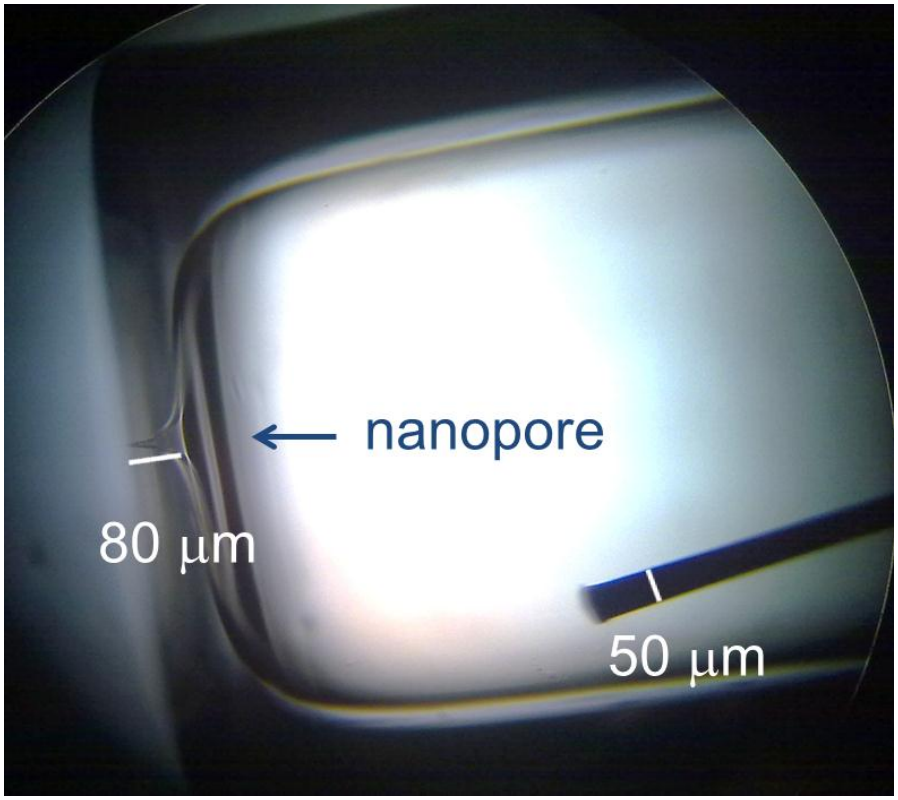

Figure 5.2. Optical-microscopy image of the GNM (side view) used in recording the translocation data presented in the main text. A 50 μm diameter W rod was inserted into the capillary for length calibration (bottom right). The GNM thickness was measured to be ~80 μm.

5.2 Experimental section

5.2.1 Chemicals

KCl, K_2HPO_4, KH_2PO_4 (Mallinckrodt), Triton X-100 (Sigma-Aldrich), 3-cyanopropyldimethylchlorosilane ($Cl(Me)_2Si(CH_2)_3CN$), and *n*-butyldimethylchloro-silane ($Cl(Me)_2Si(CH_2)_3CH_3$) (Gelest Inc.) were used as received. All aqueous solutions were prepared using water (18 MΩ cm) from a Barnstead E-pure water purification system. The KCl solutions and phosphate buffered KCl solutions at a pH of 7.4 were made by dissolving appropriate amounts of each salt in ultrapure water. Acetonitrile (HPLC grade, J. T. Baker) was stored over 3-Å molecular sieves. Non-functionalized (120 nm radius, PS02N Lot 5708, Bangs Laboratories, Fishers, IN) and -COOH modified (160 nm radius, PC02N Lot 9172) polystyrene (PS) nanoparticles were dispersed in buffered KCl solutions as received.

5.2.2 GNMs fabrication and surface modification

GNMs were fabricated according to previous reports from our laboratory.[29] Briefly, an electrochemically sharpened Pt tip was sealed in a glass capillary (Dagan Corp., Prism glass capillaries, SB16, 1.65 mm outer diameter, 0.75 mm inner diameter, softening point 700 ℃) using a H_2/air flame. The capillary was polished until a Pt nanodisk was exposed, using a sensitive electrical continuity tester. The Pt nanodisk was then partially removed by electrochemical etching in a 20% $CaCl_2$ solution with 5.9 V ac voltage applied between the Pt nanodisk and a large Pt wire counterelectrode, after which the remaining Pt wire was gently pulled from the glass to yield a conical-shaped nanopore. The interior and exterior glass surfaces of the GNMs were silanized with $Cl(Me)_2Si(CH_2)_3CN$ or $Cl(Me)_2Si(CH_2)_3CH_3$ by immersing the GNM for 20 hours in an

acetonitrile solution containing the silane. The radius of the small orifice of the GNM, *a*, was determined from the ionic resistance of the pore in 1.0 M KCl solution as previously described.[30] The relative uncertainty in *a* is estimated to be ~10%. Optical microscopy was used to measure the thickness of the glass membrane (~80 μm) containing the nanopore, Figure 5.2. All data reported herein were obtained with the single nanopore shown in Figure 5.2, which has an orifice radius of 210 nm. However, the capture and release data presented have been reproduced using numerous GNMs with orifice radii ranging from approximately 200 to 500 nm.

5.2.3 Cell configuration and data acquisition

A Pine RDE 3 potentiostat and a Dagan Cornerstone Chem-Clamp potentiostat was interfaced to a computer through a PCI 6251 data acquisition board (National Instruments). Current-time (*i*-*t*) curves were recorded by in-house virtual instrumentation written in LabVIEW (National Instruments) at a sampling frequency of 100 kHz. A 3-pole Bessel low-pass filter was applied at a cut-off frequency of 10 kHz. The GNM was filled and immersed in a 0.1 M KCl solution (pH 7.4, 0.1% Triton X-100) and polystyrene nanoparticles were homogeneously dispersed throughout the solution. Electrical contact with the reservoirs was made using the Ag/AgCl electrodes and a voltage, V_{app}, applied between these electrodes to record *i*-*t* curves. The pressure across the GNM was applied using a 10 mL gastight syringe (Hamilton Co., Reno, Nevada) and was measured by a sphygmomanometer (pressure sensing range ~ -80 to 200 mmHg). The sign of the pressure is defined as the pressure inside the capillary versus the external solution (which is at atmospheric pressure). Particles placed in the external solution are driven towards and through the pore at -*P*.

5.2.4 Computational analysis and finite-element simulations

The *i-t* recordings were plotted with Igor Pro software 6.0.2.4 (WaveMetrics, Lake Oswego, U.S.A.). The current pulses were detected and analyzed by QuB software package 1.5.0.20 (State University of New York at Buffalo, available at www.qub.buffalo.edu/). Statistical analyses of *i-t* recordings were accomplished by analyzing three or more segments of the data at each experimental condition. The finite-element simulations were performed with COMSOL Multiphysics 4.1 (Comsol, Inc.) on a high performance desktop computer (16 GB RAM).

5.3 Results and discussion

5.3.1 Capture and release of 120 and 160 nm radius particles in a mixed particle solution

We first investigated particle translocation using a 210 nm radius GNM that joined two reservoirs of aqueous 0.1 M KCl maintained at pH 7.4 by a 10 mM K_2HPO_4 / KH_2PO_4 buffer. A mixture of non-functionalized 120 nm and -COOH modified 160 nm radius particles were added to the external solution and a 200 mV potential applied across the GNM (internal vs. external solution). The top panel in Figure 5.3 shows a typical *i-t* recording for the capture and release of 3 particles recorded over an 8 s interval. The particles were first driven through the pore from external solution, and detected by a momentary blockage of the ionic current. Three resistive pulses are observed, denoted as *a*, *b*, and *c*. The size of the particles can be unequivocally assigned by the pulse heights, as determined in experiments using only 120 nm radius particles, or only 160 nm radius particles. Thus, the smaller pulse *a* corresponds to the 120 nm radius particle, while the larger pulses *b* and *c* correspond to two 160 nm radius particles.

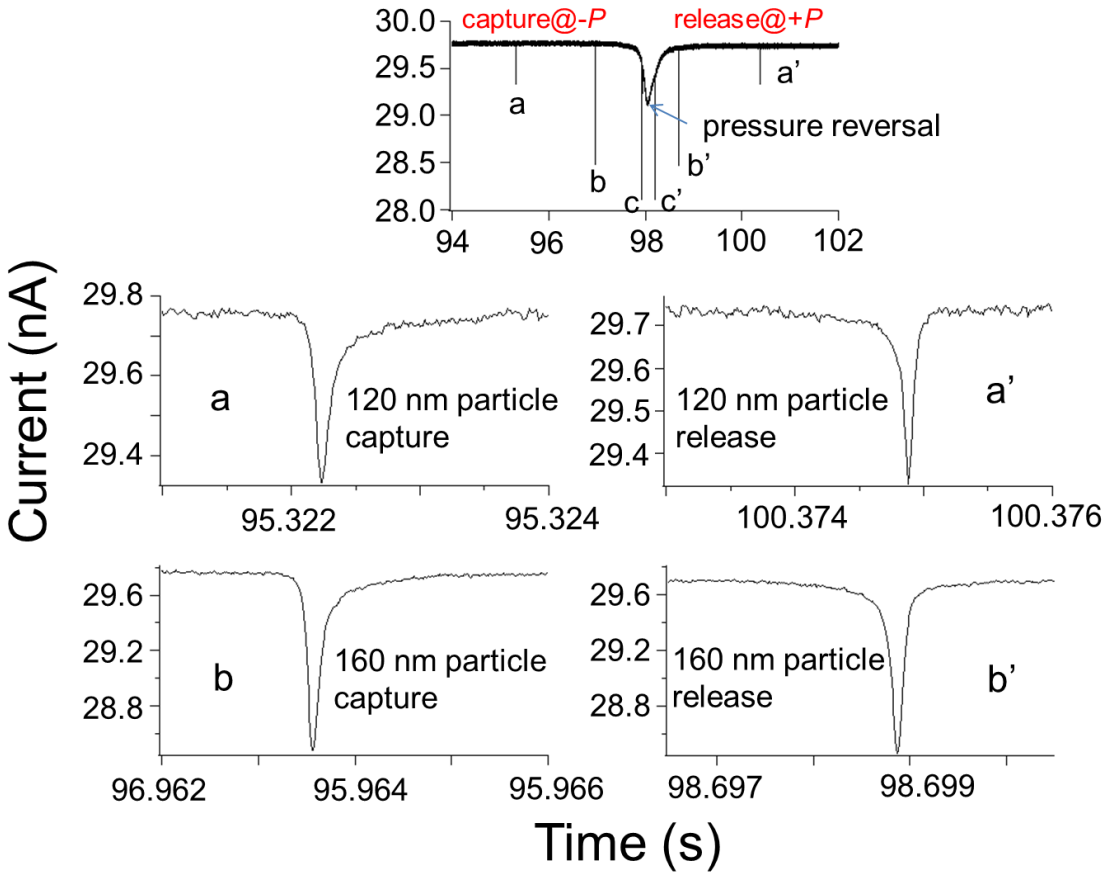

Figure 5.3. *i-t* recordings corresponding to the capture and release of 120 and 160 nm radius nanoparticles using a 210 nm radius GNM in a 0.1 M KCl solution (pH 7.4) at P = -5 mmHg (capture) and P = +5 mmHg (release). Pulses denoted by (a), (b), and (c) correspond to translocation of a 120 nm radius and two 160 nm radius particles, respectively, from the bulk solution into the GNM ("capture"). Pulses denoted by (a'), (b'), and (c') correspond to translocation of the same 120 and 160 nm radius particles from the GNM back into the bulk solution ("release"). V_{app}: 200 mV internal vs. external solution. Expanded *i-t* traces are shown for pulses (a), (a'), (b), and (b').

Upon translocation, the three particles were driven into the nanopore by pressure-driven flow for a pre-set time period. The pressure was then reversed to bring the same particles back through the GNM orifice, yielding pulses *c'*, *b'*, and *a'*, where *c'* and *b'* correspond to the two 160 nm radius particles and pulse *a'* corresponds to the smaller 120 nm radius particle. This reverse order of particle translocation is typical of the capture and release experiment; the first particle to be captured is typically the last particle to be released. However, as shown below, diffusional broadening of the particle location after it is captured results in stochastic release times, which can scramble the sequence information.

Spherical particle translocation through a conical pore results in an asymmetric triangular pulse in the *i-t* recording as previously detailed,[31] and demonstrated in the enlarged *i-t* curves in Figure 5.3 for capture/release pulse pairs *a*/*a'* and *b*/*b'*. For capture translocation, the current initially decreases steeply to a minimum value, and then slowly increases back to the baseline (pulses *a* and *b*). In contrast, the release pulse shape is the mirror image of the capture pulse shape; a sharp current increase followed by a slow decrease, as shown for pulses *a'* and *b'*. Thus, the particle translocation direction can be readily distinguished from *i-t* recordings based on the peak shape.

In addition to pressure-driven solution flow, particle motion in these experiments may be potentially influenced by diffusion, migration, electrostatic interaction with the nanopore surface charge, and electroosmotic flow (EOF). Since the nanopore has been silanized to reduce the GNM surface charge, and the experiments were performed in a relatively high electrolyte concentration (0.1 M), we assume that the electrostatic repulsion and EOF have a negligible influence on the particle's motion. The ζ-potential

of the non-functionalized 120 nm radius particles dispersed in a 0.1 M KCl solution (pH 7.4) was measured to be less than -2 mV, which we assume is sufficiently small that electrophoretic transport can be ignored.

In the absence of particle diffusion, the capture time, τ, and release time, τ_r, for pressure-driven flow should be identical. Due to diffusion, τ and τ_r are not equal and the sequence of particle release is not necessarily the reverse of the order of particle capture.

A measure of the distance that a particle diffuses, δ, along the direction of the nanopore's central axis, during the time period, t, following the initial capture, can be estimated using the Einstein relationship[32-34],

$$\delta^2 = 2Dt. \tag{5.1}$$

The particle diffusivity, D, is estimated by the Stokes-Einstein equation,

$$D = \frac{k_B T}{6\pi\eta r}, \tag{5.2}$$

where k_B is the Boltzmann constant, T is the absolute temperature, η is the viscosity of the solution, and r is the particle radius. For a 120 nm radius particle, D is 2.0×10^{-12} m^2/s and δ was computed to be 3.5 μm in a 3 s duration. The 120 nm radius particle is estimated to travel, by pressure-driven flow, a distance of ~50 μm from the pore orifice through the nanopore in this 3 s duration, assuming that the particle travels uniformly with the fluid along the pore axis. Thus, diffusion is expected to lead to a ~10% variation

in τ_r following the pressure reversal. A detailed simulation of the particle trajectory is described in the following sections.

5.3.2 Capture and release of multiple 120 nm radius particles

Experiments were carried out in a concentrated PS particle solution (~10^{10} particles/mL) in order to capture and release large numbers of nanoparticles over a short period of time. Negative pressure was first applied for a predetermined time period (~10 s, see Figure 5.4a), resulting in translocation of an average of ~370 particles through the GNM. The pressure was then reversed and maintained. The particles, having just passed through the GNM, now travel in the opposite direction through the GNM. Following pressure reversal at ~12 s, nearly the same amount of particles translocated back through nanopore over a ~40 s period.

Figure 5.4b shows the rate of particle translocation for the data presented in Figure 5.4a at different times during capture and release. Each data point represents the translocation rate in a 1 s interval centered about the corresponding time. The bold black lines represent the predictions of the finite-element simulation, which will be discussed below. For capture translocations, the rate increased during the first 1 s following the pressure application and then remained constant at ~33 events s^{-1} (the slow increase results from manual application of the pressure, which requires ~1s). The relatively large error bars for the experimental translocation rates are due to the small bin size (1 s). After the pressure is reversed, the particle release transfer rate is constant and equal to the capture rate (~33 events s^{-1}), and then slowly decreases over time as all of the particles are released.

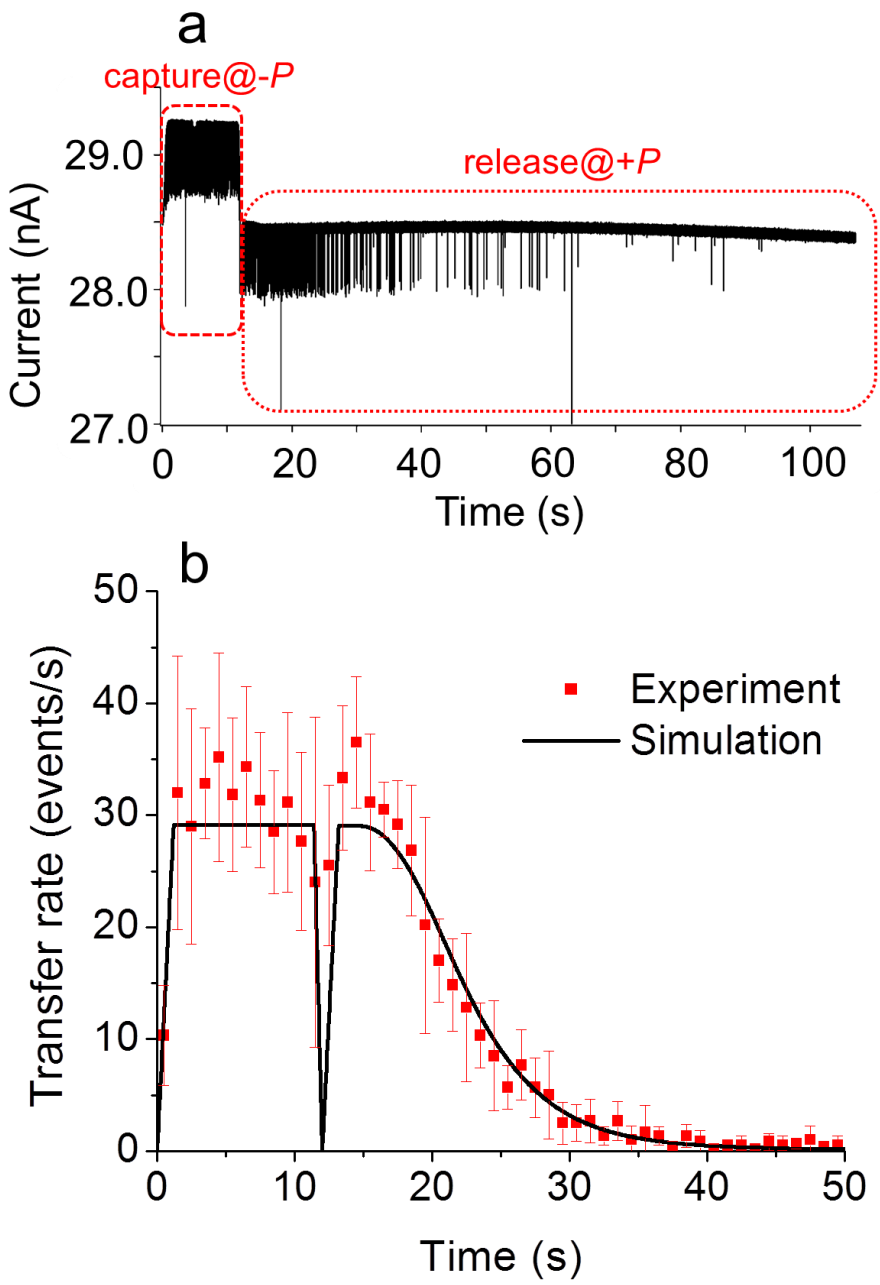

Figure 5.4. (a) *i-t* recording for the capture and release of 120 nm radius particles (GNM size: 210 nm radius, 1.3×10^{10} particles/mL, V_{app}: 200 mV internal vs. external). A -10 mmHg pressure was applied to drive the particles through the pore (0 to ~12 s). The pressure was reversed to 10 mmHg at ~12 s and maintained until 110 s to drive the particles inside the pore back to the external solution. (b) Instantaneous translocation rates for the particle capture and release experiments (±10 mmHg pressures for the data in part a). Each red point represents the rate at which particles enter the pore within a 1 s time interval (for example, the point at 0.5 s represents the rate within the interval 0 and 1 s). The bold black line represents the transfer rate predicted by finite-element simulations.

5.3.3 Finite-element simulations

A diffusion-convection model was used to quantitatively predict the stochastic instantaneous particle translocation event rate, using the Ergodic principle to relate observations of discrete particle translocation events to calculations based on continuum analytical expressions. In our continuum based simulations, the finite size of the particle is not considered. To simplify the model, the 0.1 M KCl solution was considered as incompressible, and migration and electroosmosis were ignored. A physical description of the pressure-driven flow in a pore begins with the Navier-Stokes equation.

$$\mathbf{u}\nabla\mathbf{u} = \frac{1}{\rho}(-\nabla P + \eta\nabla^2\mathbf{u}) \tag{5.3}$$

In eq 5.3, **u** is the local position-dependent fluid velocity, ρ and η are the density and viscosity of the fluid, respectively, and P is the pressure.

The particle distribution and flux inside the pore were modeled by the Nernst-Planck equation, assuming electroneutrality and ignoring particle migration.

$$\mathbf{J} = -D\nabla c + c\mathbf{u} \tag{5.4}$$

In eq 5.4, **J** and c are, respectively, the flux and concentration of the particles. The two terms on the right-hand side represent diffusion and the pressure-driven convection. The finite-element method was utilized to solve the coupled equations, details of which are presented in the Appendix. The glass surface of the nanopore was defined as an

uncharged and insulating boundary. Input parameters were chosen to reflect a 0.1 M KCl solution (T = 298 K, $\rho = 10^3$ kg m^{-3}, and $\eta = 8.9 \times 10^{-4}$ Pa s).

The orifice radius and length of the GNM were set to 210 nm and 80 μm, respectively (corresponding to actual size of the GNM, Figure 5.2). To approximate the semi-infinite volume of the solution far away from the nanopore, the exterior boundary of the bulk solution in the model was extended to a distance ~100 μm from the opening of the GNM. The inflow particle concentration was set to equal the concentration used in the experiment (2.2×10^{-8} mol m^{-3}). A built-in function of the COMSOL software (Piecewise) was input to control the pressure applied at the pore orifice. We have previously demonstrated that 77% of the overall applied pressure drop occurs within the interior of a conical shaped nanopore, the remaining pressure drop occurring in the external solution near the pore orifice.[31] Thus, in the simulation, the applied pressure was adjusted correspondingly to the 77% value of the experimental pressure. However, this adjustment does not significantly affect the probability curves presented below, since the effect is cancelled out with the application of both positive and negative pressures during the simulation. The boundary conditions and the mesh used in the study are summarized in the Appendix. Strict time stepping (0.02 s) was employed in the COMSOL solver in order to fully resolve the multiple particle capture and release process.

Figure 5.5 shows the simulated particle concentration distribution inside the GNM at different times when the pressure waveform was applied. Initially (t = 0 s), no particles are present inside the GNM. At t > 0 s, a negative pressure was applied and the particles began to translocate through the opening of the GNM and continued to disperse into the pore with increasing time (t = 5 and 10 s). After the pressure was reversed at t = 12 s

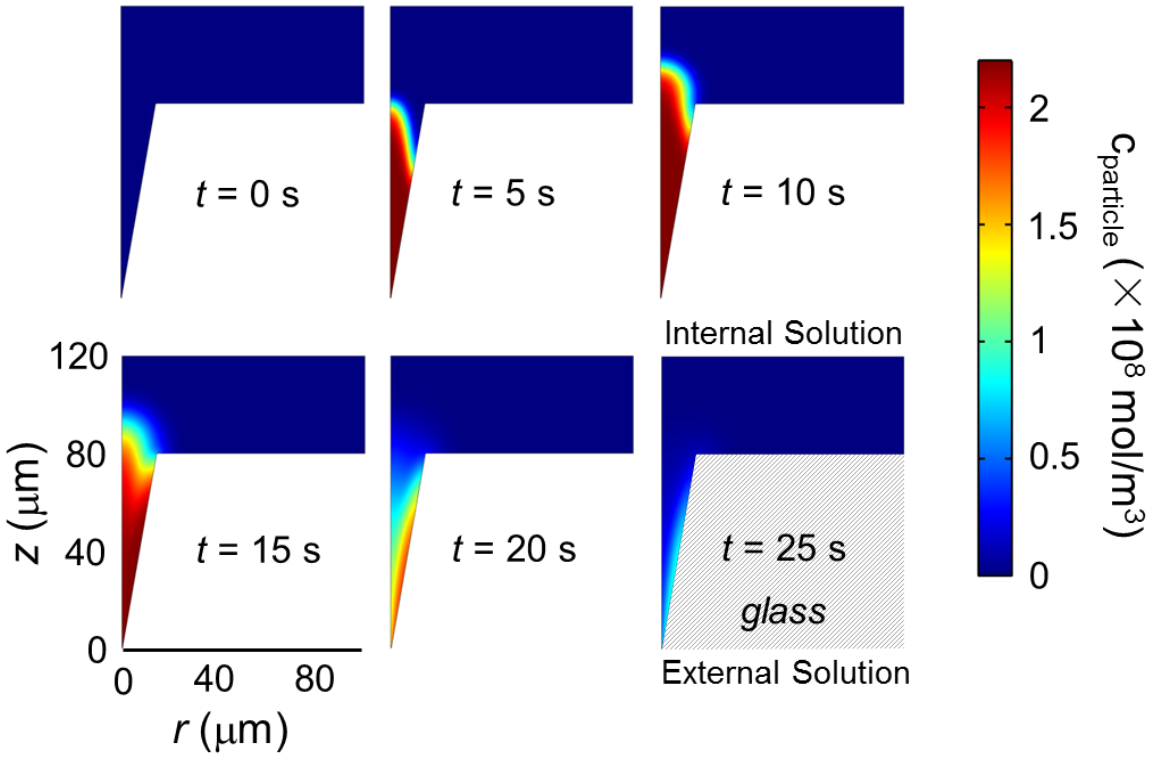

Figure 5.5. Simulated time-dependent average particle concentration distribution within a 210 nm radius pore during a capture and release experiment. The particle concentration at the pore orifice was set as constant (2.2×10^{-8} mol/m^3). The particles were treated as points in this continuum simulation, i.e., the finite size of the particle was not taken into account in the simulation. The -10 mmHg pressure was applied for the first ~10 s to drive particles from external solution to the pore interior (geometry shown in each figure), and then the pressure was reversed to 10 mmHg to drive particles back to the external solution. The simulation corresponds to the capture and release of 323 particles.

(corresponding to the experimental pressure waveform used in collecting the data in Figure 5.4), the particle concentration within the nanopore decreased due to the change of flow direction (t = 15, 20, and 25 s). With the continuing application of positive pressure (t = 50 s, simulation not shown), all of the particles that initially entered the pore have returned to the external solution.

The particle transfer rate (particle s^{-1}) through the GNM was then computed by the integration of simulated particle flux (mol m^{-2} s^{-1}) across the GNM orifice (m^2) as a function of time, and the results are shown as the solid curve in Figure 5.4b. Integration across the cross sectional area at a distance z = 50 nm inside the nanopore was used to calculate the particle flux through the GNM.

Dividing the instantaneous release transfer rate (Figure 5.4b) by the total number of capture translocations yields the particle return probability. Figure 5.6 shows the return probability histograms for different release pressures. Each bar represents the translocation probability in a 1-s interval centered about the corresponding time. The simulation based histograms are in good agreement with the experimental histograms. As shown in Figure 5.6, the histograms of release times depend strongly on the release pressure, with shorter release times at higher pressures.

The cumulative count percentages of particle release as a function of release time are plotted in the Appendix. The release pressure has a strong effect on the overall release success rate at different times. Approximately 95% of the particles were released in 10 s after the pressure reversal at a release pressure of 20 mmHg. At 15 and 5 mmHg, that value decreased to 90% and 50%, respectively.

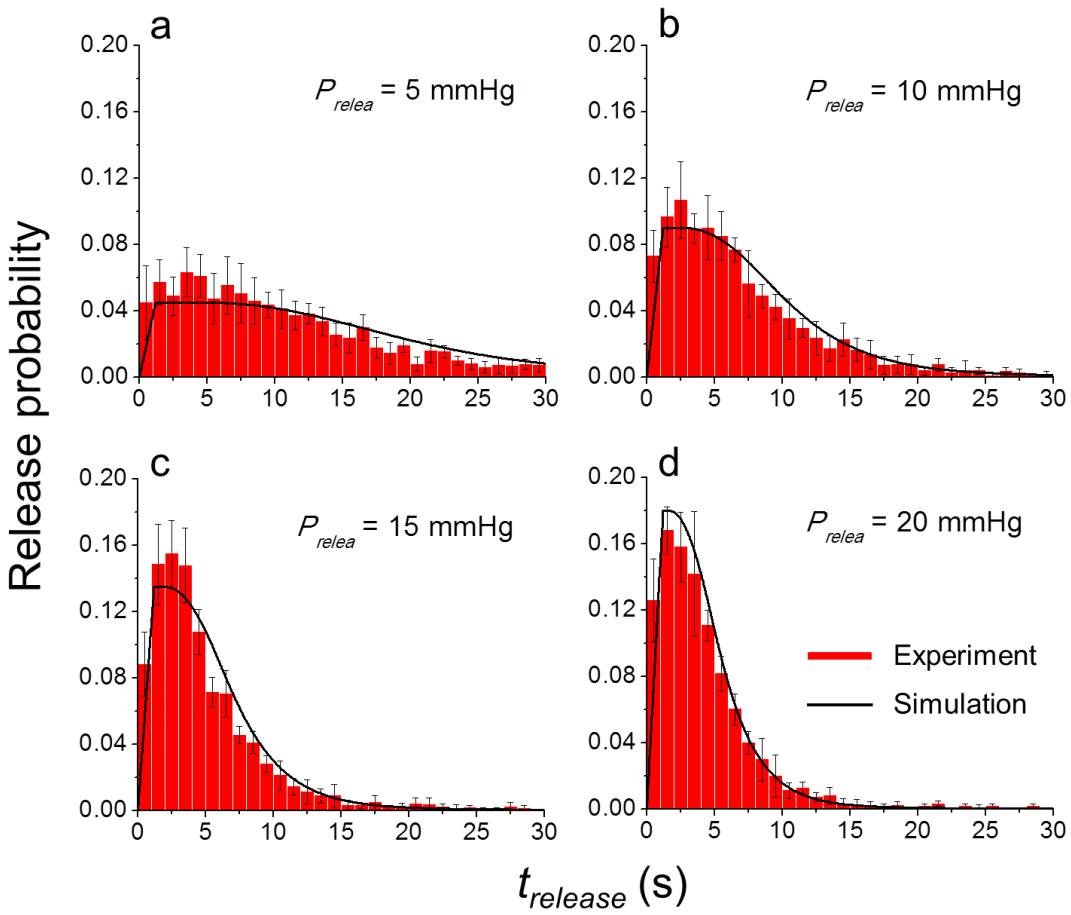

Figure 5.6. Release probabilities as a function of time for 120 nm radius particles from a 210 nm radius nanopore at release pressures of (a) 5, (b) 10, (c) 15, and (d) 20 mmHg. The capture pressure was -10 mmHg for all experiments. The particles were driven from the external solution into the GNM for ~12 s. $t_{release}$ = 0 s in the figures corresponds to the instant at which pressure was reversed. The data correspond to the capture and release of ~370 particles in each experiment.

5.3.4 Capturing and releasing single nanoparticles

The above experiments demonstrate that hundreds of particles may be captured and released in a single experiment, and that this process is well described by a convective diffusion model. Conversely, a single nanoparticle may be captured and released multiple times in an individual experiment.

Figure 5.7 shows an example of this experiment, in which a 120 nm radius particle was driven through a 210 nm radius nanopore at a pressure of -5 mmHg. The experiments were conducted in 0.1 M KCl solutions with low particle concentration (~10^7 particles/mL) and low pressure (5 mmHg) in order to capture only one particle in the programmed time. After a particle passed through the pore, the pressure was maintained at -5 mmHg for a time, τ, between 3 and 10 s, and then reversed to 5 mmHg to drive the particle back through the nanopore orifice. As shown in Figure 5.7a, for example, a particle translocating the pore in the capture direction was detected by an ionic current blockage. A time of ~6.5 s was allowed to elapse, and then the pressure was reversed, and the particle translocated the pore in the reverse direction, as evidenced by a second current blockage, indicating that the nanoparticle had entered the bulk solution. The pressure was then returned to -5 mmHg, driving the same particle back or another particle through the pore. We found that probability of releasing the particle was nearly 100%, as long as the time interval between the particle capture and the pressure reversal was less than 10 seconds.

We varied the time between the capture translocation and the pressure reversal, τ, and measured τ_r, the time until the particle re-enters the external solution after pressure reversal, in order to probe the behavior of the particles that traveled different distances

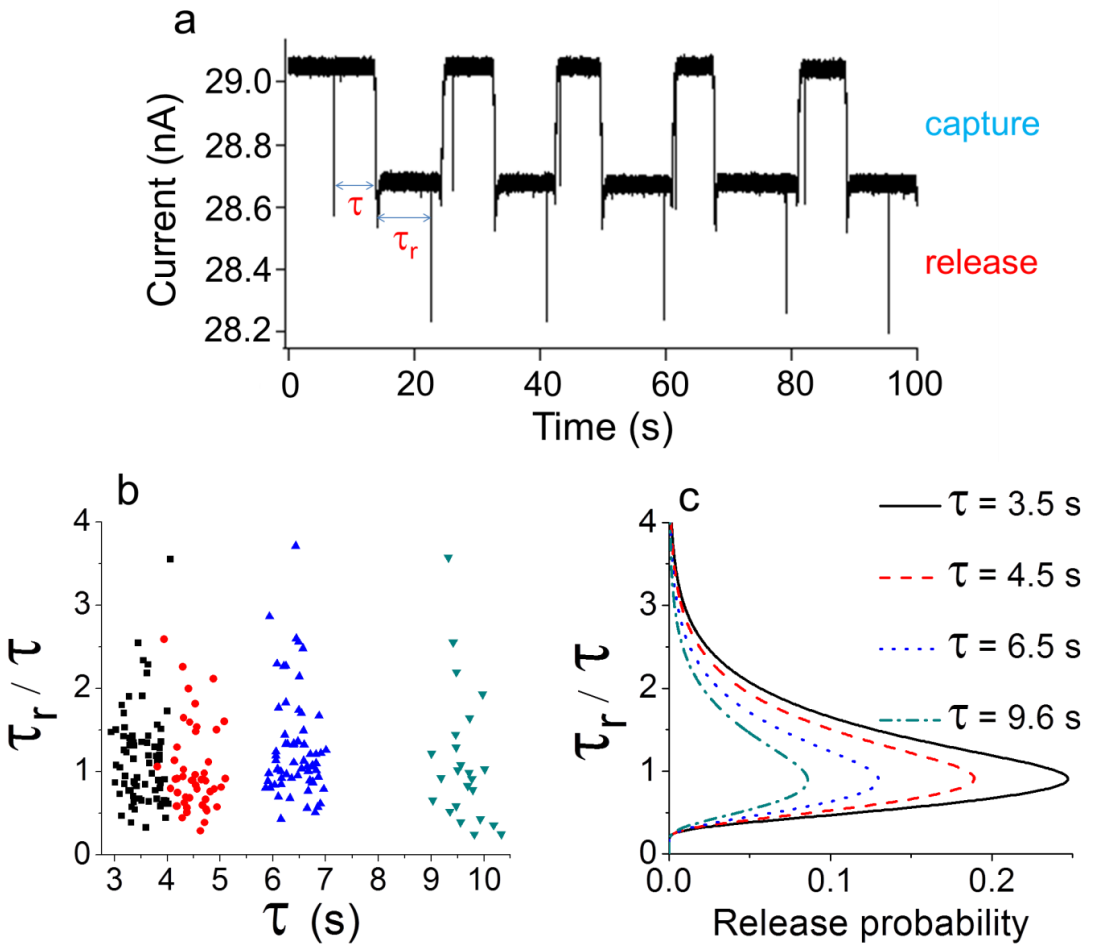

Figure 5.7. (a) *i-t* recordings for capturing and releasing *single* 120 nm radius particle multiple times using a 210 nm radius GNM in a 0.1 M KCl solution containing 1.3 × 10^7 PS particles/mL. In this particular *i-t* trace, the particle was captured for τ = 6.5 ± 0.3 s at -5 mmHg and then released at +5 mmHg. V_{app}: 200 mV internal vs. external. (b) Experimental τ_r/τ ratio distributions for different capture times, τ. τ_r refers to the time needed to release a single 120 nm radius particle. In each capture/release event, the particle was captured for τ = 3.5 ± 0.3 s (black squares, 74 events), τ = 4.5 ± 0.3 s (red circles, 49 events), τ = 6.5 ± 0.3 s (blue upward triangles, 65 events), and τ = 9.6 ± 0.3 s (green downward triangles, 24 events). (c) Simulated return probability curves as a function of τ_r/τ for different τ.

within the nanopore. Figure 5.7b shows the experimental distribution of the ratio τ_r/τ as a function of τ. These data were collected by capturing and releasing the nanoparticle for τ between 3.5 and 9.6 s. The spread in the experimental values of τ is due to the manual control of the pressure; however, precise values of both τ and τ_r are readily obtained from electrical signatures in the *i-t* curves. Figure 5.7b shows that the τ_r is strongly dependent on the elapsed time after the capture translocation, but the distribution of ratios between the release time (τ_r) and capture time (τ) remains relatively constant.

In order to simulate the single-nanoparticle release probability, Figure 5.8, a particle flux pulse was generated manually in the simulations by setting the particle concentration at the orifice to 1.3×10^{-4} mol·m^{-3} and applying a low pressure (3.75×10^{-2} mmHg, 5 Pa) for a short time period (0.001 s). Since the time duration of the low-pressure pulse is very short, the particles move a very short distance into the pore (~200 nm). The number of particles driven into the pore during this pulse is of the order of unity (~1), as computed from the simulated particle concentration distribution. The resulting particle concentration distribution at t = 0.001 s was then used to simulate experiments where a single particle enters the pore (the capture event), transported deep into the pore (tens of micrometers), and then, following pressure reversal, is transported in the reverse direction until it passes again through the pore orifice. Following the introduction of the particle, the inflow concentration and outlet pressure were set to 0 mol·m^{-3} and -5 mmHg, respectively. The probability distribution inside the GNM continues to vary due to pressure-driven flow and diffusion effects afterwards. The time step was adjusted to 2×10^{-5} s during the initial 0.004 s of "particle injection" and then increased to 0.001 and 0.02 s afterwards. After a predetermined time, the pressure was reversed. The moment at

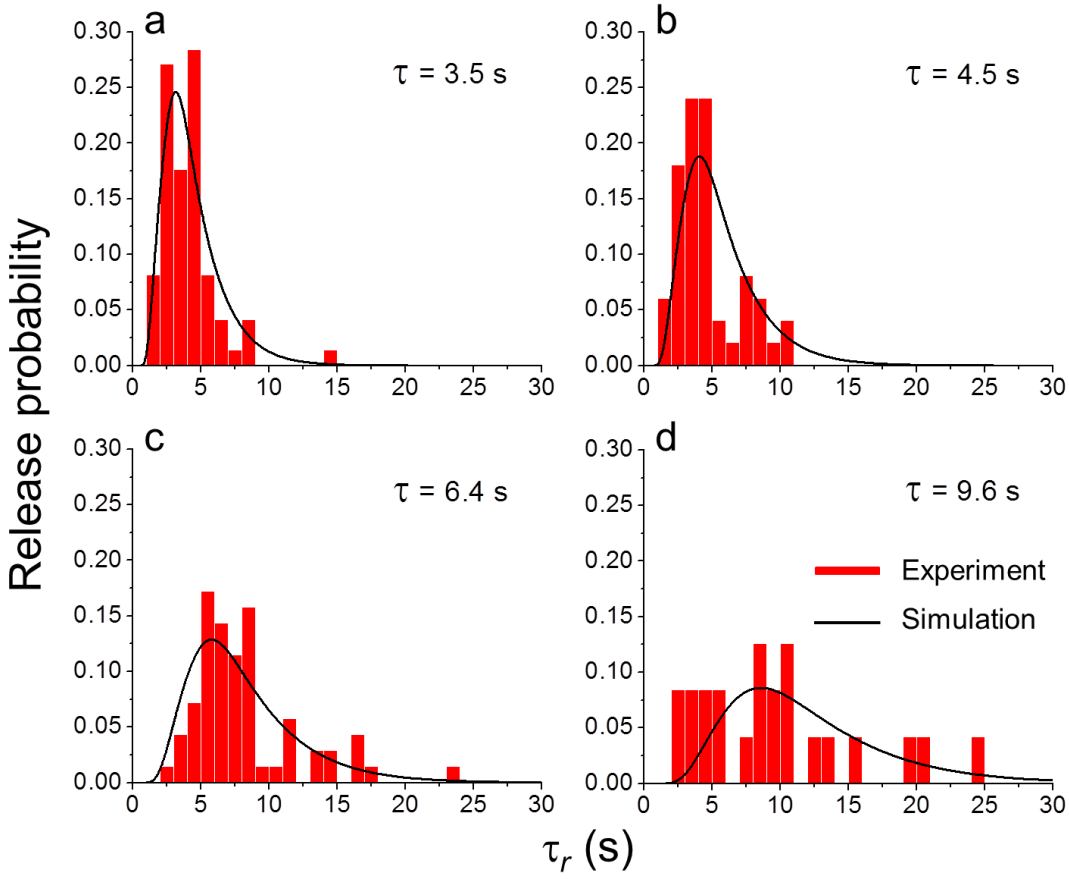

Figure 5.8. Experimental histograms of the probability of particle release as a function of release time (τ_r) at different capture times (τ), for the same data and experimental conditions described in Figure 5.7: (a) 3.5 s (74 events), (b) 4.5 s (49 events), (c) 6.5 s (65 events), and (d) 9.6 s (24 events). Simulated release probability curves are shown for comparison with the experimental data.

which the pressure was reversed corresponds to $\tau_r = 0$ s (the origin of Figure 5.8). As τ increases, the maximum in the release probability distributions decreases, a consequence of diffusional broadening of the particle's position. The discrepancy between experiments and simulation originates primarily from the limited sample size, uncertainties in small pressures, as well as the assumptions and treatment in the simulation mentioned above. A discussion of the sources of error is presented in the Appendix.

The convection-diffusion model described above also successfully predicts the normalized distribution of τ_r/τ for single nanoparticle release, as shown in Figure 5.7c. Each return probability distribution curve has a maximum value at $\tau_r/\tau \sim 1$, in agreement with the experimental results.

Because the width of the τ_r/τ distribution curve, Figure 5.7c, is a function of the particle diffusion coefficient (*D*), eq 5.4, the method presented above can be used, in principle, to measure the size of a single particle (indeed, in the absence of knowing the radii of the PS particles, the above analyses could have been performed by adjusting *D* in the simulations to obtained a "best fit" to the experimental data, and then using eq 5.2 to compute the particle size). For very small particles (< 10 nm), manual control of the pressure reversal (1-2 s reversal time) may not be suitable since the particle may diffuse too quickly for accurate measurements. For instance, Gershow and Golovchenko employed a $\tau < 50$ ms to probe the diffusional property of DNA.[25] A systematic study is required to achieve a thorough understanding of this pressure capture and release method and future applications. However, this problem can be potentially overcome by improved engineering design, such as using an automatic translocation signal-activated pressure reversal trigger.

5.4 Conclusions

A pressure-reversal method to capture and release nanoparticles using conical-shaped nanopores has been presented. An individual nanoparticle may be driven multiples times through a nanoscale orifice in a membrane to study stochastic diffusional broadening, or multiple particles may be driven through the orifice, and their sequence read-out in the release translocations. Quantitative analysis of the capture and release events are in good agreement with predictions from finite-element simulations based on a convective-diffusion model.

The pressure-reversal resistive-pulse technique has several potential applications that expand analyses of nanoparticles. For instance, as noted above, it is possible to measure the size of a single particle by passing it repeatedly back and forth through the nanopore orifice, and measuring the diffusional broadening reflected in the distribution of τ_r. In addition, it should be possible to study time-dependent reactions that change the particle size as the particle passes repeatedly between the external and internal solutions. A prerequisite for the study of time-dependent reactions is that the reaction must take place in a relatively short period of time in order to be detected in the release stage. These potential applications of the pressure-reversal resistive-pulse method are currently under investigation.

5.5 Appendix

5.5.1 Finite-element simulations

COMSOL Multiphysics Software (Version 4.1) was used with the Laminar Flow and Transport of Diluted Species (i.e., convection and diffusion) models. Figure 5.9 and 5.10 show the geometry of the model and the cumulative probability for multiple-particle release at different pressures, respectively.

5.5.2 Discussion of sources of error

Agreement between experimental and simulated values in Figures 5.6 and 5.10 is remarkably good, in view of that fact that no adjustable parameters are used in the simulations. However, there are a number of sources of possible error that may contribute to the small discrepancies between experiment and simulation. First, the smallest increment of our pressure gauge is 2 mmHg, which introduces significant error when working with small pressures (e.g., 5 mmHg). Second, there is uncertainty in the pore geometry, especially in the orifice radius (~10%) and half-cone angle. Third, while the migration term is negligible compared to the convection term, it is likely significant relative to diffusion in close vicinity of the pore orifice where the electric field is large. However, since the particle spends most of the time inside the nanopore far removed from the high field at the orifice, migration should not have a large effect on values of τ or τ_r. Other minor sources of error may include the electroosmotic flow and electrostatic repulsion caused by the glass surface charge, which are not included in the computer simulations.

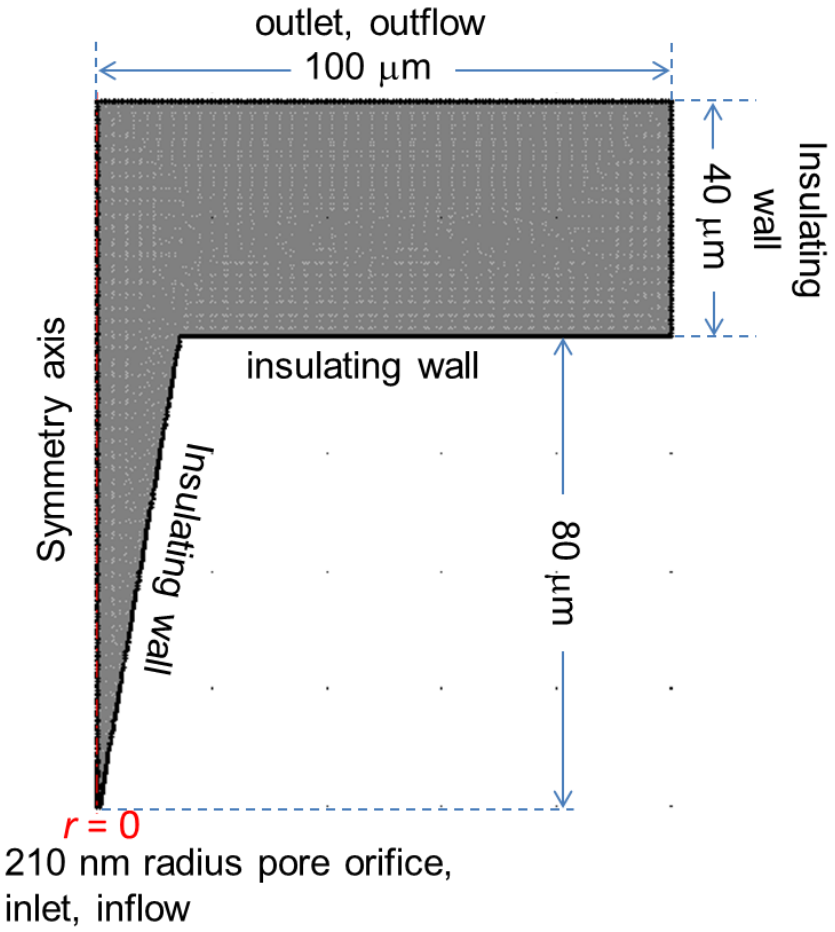

Figure 5.9. The 2D axial-symmetric geometry, mesh, and the boundary conditions used in the finite-element simulations. The symmetry axis is located at $r = 0$. The mesh size is refined to ~1 nm at the conical orifice to obtain a more accurate numerical prediction of the volumetric flow rate and particle flux.

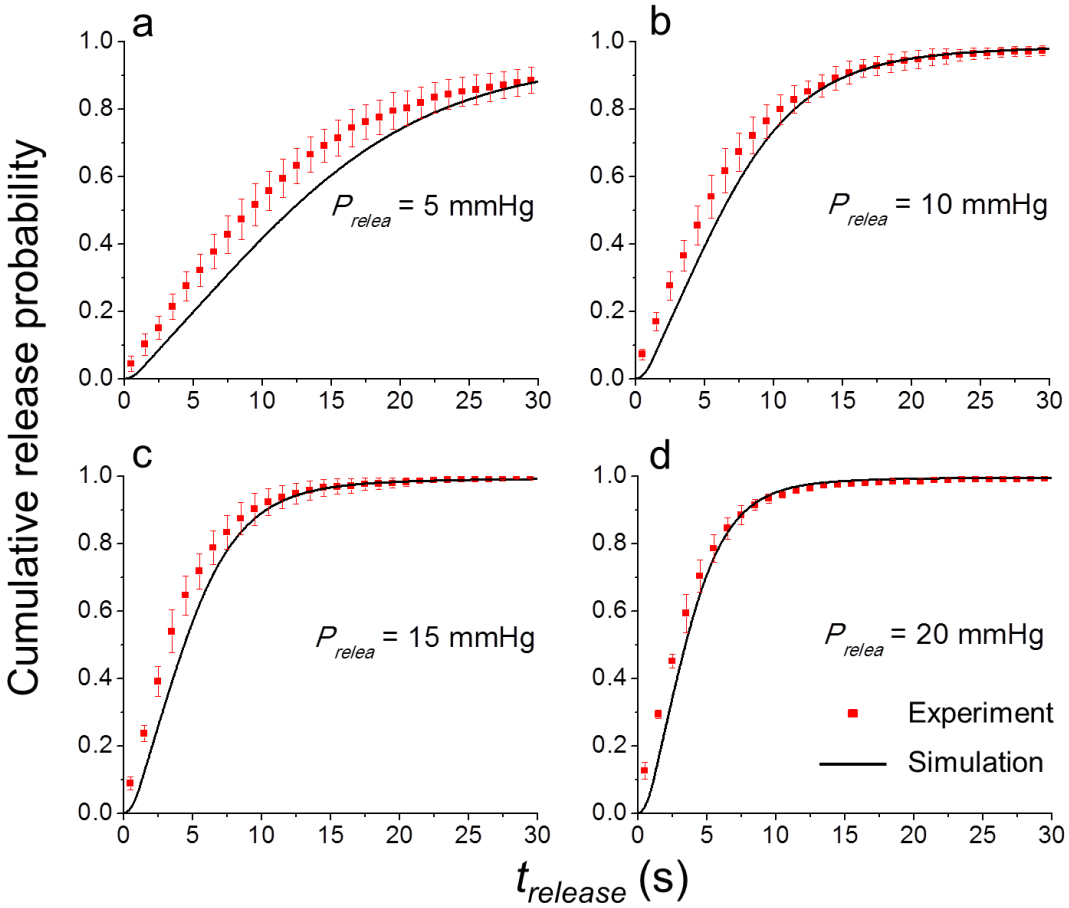

Figure 5.10. Cumulative probability as a function of time for the release of 120 nm radius particles in 0.1 M KCl solution following their initial capture through a 210 nm radius nanopore at -10 mmHg. The release pressures are: (a) 5, (b) 10, (c) 15, and (d) 20 mmHg. $t_{release}$ = 0 s corresponds to the moment that the pressure was reversed following the capture translocation event.

5.5.3 Particle capture at different capture pressures

After examining the release dynamics for multiple particles and single particles (main text), it is also interesting to explore the dependence of the time to capture the first particle on capture pressure. Particles were also placed in the external solution; however, instead of applying negative pressure, a positive pressure of 10 mmHg was first applied for ~10 s to drive particles away from the GNM opening. The initial application of positive pressure creates a depletion zone of particles around the pore orifice in the external solution. Afterwards the pressure was reversed to different negative pressures for particle capture and the time required to capture the first nanoparticle was noted (Figure 5.11 a-c). The experiments were repeated 10 times at capture pressures of -2, -5, and -10 mmHg, and the statistics are displayed in Figure 5.11d. It is clear that the average capture time decreased with the increased capture pressure, a consequence of the different volumetric rates through the nanopore generated by -2, -5, and -10 mmHg pressures.

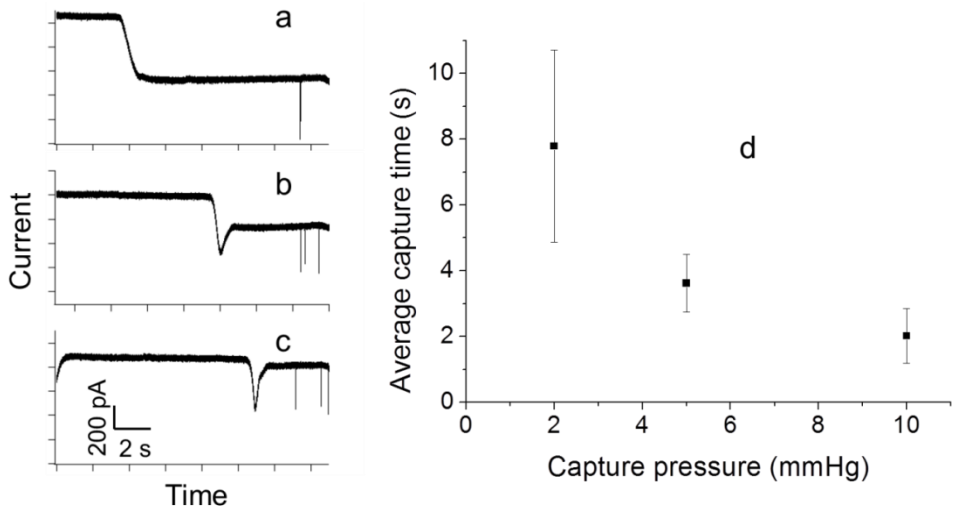

Figure 5.11. *i-t* recordings of 120 nm radius particle capture experiments with the capture pressure of (a) -2, (b) -5, and (c) -10 mmHg. The release pressure was held at 10 mmHg for ~10 s before being switched to a negative pressure. (d) Plot of the average time to capture the first particle as a function of capture pressure. GNM size: 210 nm radius. PS particle: 1.3×10^9 particles/mL. V_{app}: 200 mV internal vs. external.

5.6 References

(1) Lan, W. J.; White, H. S. *ACS Nano*, submitted.

(2) Coulter, W. H. Means for Counting Particles Suspended in a Fluid. U.S. Patent 2,656,508, 1953.

(3) Bayley, H.; Martin, C. R. *Chem. Rev.* **2000**, *100*, 2575-2594.

(4) Li, J.; Stein, D.; McMullan, C.; Branton, D.; Aziz, M. J.; Golovchenko, J. A. *Nature* **2001**, *412*, 166-169.

(5) Chen, P.; Mitsui, T.; Farmer, D. B.; Golovchenko, J.; Gordon, R. G.; Branton, D. *Nano Lett.* **2004**, *4*, 1333-1337.

(6) Dekker, C. *Nature Nanotech.* **2007**, *2*, 209-215.

(7) Martin, C. R.; Siwy, Z. S. *Science* **2007**, *317*, 331-332.

(8) Saleh, O. A.; Sohn, L. L. *Proc. Natl. Acad. Sci. U.S.A.* **2003**, *100*, 820-824.

(9) Bezrukov, S. M.; Vodyanoy, I.; Parsegian, V. A. *Nature* **1994**, *370*, 279-281.

(10) Kasianowicz, J. J.; Brandin, E.; Branton, D.; Deamer, D. W. *Proc. Natl. Acad. Sci. U.S.A.* **1996**, *93*, 13770-13773.

(11) Gu, L. Q.; Braha, O.; Conlan, S.; Cheley, S.; Bayley, H. *Nature* **1999**, *398*, 686-690.

(12) Bayley, H.; Cremer, P. S. *Nature* **2001**, *413*, 226-230.

(13) Meller, A.; Nivon, L.; Branton, D. *Phys. Rev. Lett.* **2001**, *86*, 3435-3438.

(14) Henrickson, S. E.; Misakian, M.; Robertson, B.; Kasianowicz, J. J. *Phys. Rev. Lett.* **2000**, *85*, 3057-3060.

(15) Zhou, K.; Li, L.; Tan, Z.; Zlotnick, A.; Jacobson, S. C. *J. Am. Chem. Soc.* **2011**, *133*, 1618-1621.

(16) Sun, L.; Crooks, R. M. *J. Am. Chem. Soc.* **2000**, *122*, 12340-12345.

(17) Ito, T.; Sun, L.; Crooks, R. M. *Anal. Chem.* **2003**, *75*, 2399-2406.

(18) Ito, T.; Sun, L. Bevan, M. A.; Crooks, R. M. *Langmuir* **2004**, *20*, 6940-6945.

(19) Fraikin, J.-L.; Teesalu, T.; McKenney, C. M.; Ruoslahti, E.; Cleland, A. N. *Nature Nanotech.* **2011**, *6*, 308-313.

(20) Li, J. L.; Gershow, M.; Stein, D.; Brandin, E.; Golovchenko, J. A. *Nature Mater.* **2003**, *2*, 611-615.

(21) Han, A.; Schürmann, G.; Mondin, G.; Bitterli, R. A.; Hegelbach, N. G.; De Rooij, N. F.; Staufer, U. *Appl. Phys. Lett.* **2006**, *88*, 093901.

(22) Storm, A. J.; Storm, C.; Chen, J.; Zandbergen, H.; Joanny, J.-F.; Dekker, C. *Nano Lett.* **2005**, *5*, 1193-1197.

(23) Berge, L. I.; Feder, J.; Jossang, T. *Rev. Sci. Instrum.* **1989**, *60*, 2756-2763.

(24) Berge, L. I.; Jossang, T.; Feder, J. *Meas. Sci. Technol.* **1990**, *1*, 471-474.

(25) Gershow, M.; Golovchenko, J. A. *Nature Nanotech.* **2007**, *2*, 775-779.

(26) Stein, D. *Nature Nanotech.* **2007**, *2*, 741-742.

(27) Bates, M.; Burns, M.; Meller, A. *Biophys. J.* **2003**, *84*, 2366-2372.

(28) Lathrop, D. K.; Ervin, E. N.; Barrall, G. A.; Keehan, M. G.; Kawano, R.; Krupka, M. A.; White, H. S.; Hibbs, A. H. *J. Am. Chem. Soc.* **2010**, *132*, 1878-1885.

(29) (a) Zhang, B.; Galusha, J.; Shiozama, P. G.; Wang, G.; Bergren, A. J.; Jones, R. M.; White, R. J.; Ervin, E. N.; Cauley, C. C.; White, H. S. *Anal. Chem.* **2007**, *79*, 4778-4787. (b) Schibel, A. E. P.; Edwards, T.; Kawano, R.; Lan, W. J.; White, H. S. *Anal. Chem.* **2010**, *82*, 7259-7266. (c) Lan, W. J.; Holden, D. A.; White, H. S. *J. Am. Chem. Soc.* **2011**, *133*, 13300-13303. (d) Holden, D. A.; Hendrickson, G. R.; Lan, W. J.; Lyon, L. A.; White, H. S. *Soft Matter* **2011**, *7*, 8035-8040.

(30) White, R. J.; Zhang, B.; Daniel, S.; Tang, J. M.; Ervin, E. N.; Cremer, P. S.; White, H. S. *Langmuir* **2006**, *22*, 10777-10783.

(31) (a) Lan, W. J.; Holden, D. A.; Zhang, B.; White, H. S. *Anal. Chem.* **2011**, *83*, 3840-3847. (b) Lan, W. J.; Holden, D. A.; Liu, J.; White, H. S. *J. Phys. Chem. C* **2011**, *115*, 18445-18452.

(32) Berg, H. C. *Random Walk in Biology*; Princeton University Press: Princeton, NJ, 1993.

(33) White, R. J.; White, H. S. *Anal. Chem.* **2005**, *77*, 214A-220A.

(34) Einstein, A. *Ann. d. Physik* **1905**, *17*, 549-560. (*Investigation on the Theory of Brownian Movement*; translated by Cowper, A. D. Methuen: London, 1926.)